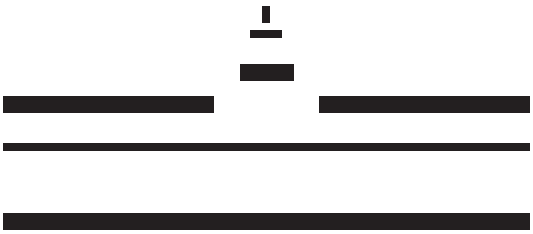

Westfälische
Wilhelms-Universität
Münster

Diplomarbeit in Mathematik

Comparison of Numerical Approaches to the EEG Forward Problem

eingereicht von

Johannes Vorwerk

Münster, 12. April 2011

Fachbereich 10
Mathematik und
Informatik

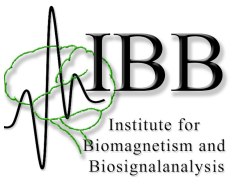

Gutachter:

Prof. Dr. Martin Burger

Institut für Numerische und Angewandte Mathematik

Priv.-Doz. Dr. Carsten Wolters

Institut für Biomagnetismus und Biosignalanalyse

Abstract

This thesis is devoted to the study and optimization of solution approaches to the forward problem of electroencephalography (EEG). We will investigate different numerical approaches regarding time consumption and particularly accuracy, two aspects that are crucial for solving the inverse problem of EEG, i.e., reconstructing source activity from measurement data. Several studies have shown that the accuracy of the solution highly depends on a realistic modeling of the human head. Besides others, two different numerical techniques are commonly used in combination with realistically shaped head models nowadays: Boundary element methods (BEM) and finite element methods (FEM). We will evaluate a recently proposed BE approach, the symmetric BEM, and will demonstrate that it leads to a considerably improved accuracy in multi-layer sphere models compared to former BE formulations. Furthermore, we will enhance accuracy and speed of different FE approaches by the application of leadfield interpolation, a technique originally proposed for the speed-up of BE calculations. Various investigations regarding the accuracy of the FE approaches in multi-layer sphere models are carried out before leadfield interpolation is applied to further optimize the results.

Acknowledgements

I want to thank everyone who made this thesis and my studies possible, especially

- Carsten Wolters for introducing me to this field of research and providing me with the right literature and tools,
- Martin Burger for being advisor of this thesis,
- Maureen Clerc and her group for introducing me to the OpenMEEG toolbox and the underlying theory,
- Behrend, Felix, Lars and Susanne for taking the time to read this thesis and to provide me with corrections and annotations,
- My parents for their mental and financial support at all times.

Contents

List of Figures

List of Tables

Introduction

The human brain is a highly complex organ, being topic of research since ages. Though brain research has already gained deep insight up to the brain's fundamental functions, there are still many open and only partially answered questions, like those for the emergence of emotions or the origin of mental diseases, e.g., depression. Therefore, technologies that allow for the investigation of the brain and its activity have been and still are developed. Besides cognitive science, many of these inventions have become an important tool in clinical routine, e.g., in pre-surgical epilepsy diagnosis.

The variety of different technologies allowing an investigation of the brain is large. Some of them are designated to create images of the head's anatomy, e.g., *X-ray computed tomography* (CT) or *magnetic resonance imaging* (MRI), others allow to observe the characteristics of metabolism, e.g., *positron emission tomography* (PET), *single photon emission computed tomography* (SPECT) or *functional magnetic resonance imaging* (fMRI); *electroencephalography* (EEG) and *magnetoencephalography* (MEG) again are able to measure the simultaneous activity of patches of neurons on a millisecond timescale.

The localization of *primary* or *impressed currents*, which cause the electromagnetic fields recorded by EEG or MEG, demands the solution of the *inverse problem of EEG/MEG*, which has to be carried out numerically. The *forward problem of MEG* is directly related to the *forward problem of EEG* via the *Biot-Savart law*. Therefore, the accurate simulation of the potential distribution induced by a certain source configuration, i.e., the forward problem of EEG, is crucial. The comparison and optimization of speed and accuracy of different approaches to its solution will be the main topic of this thesis.

Besides quasi-analytical solutions, requiring the assumption that the anatomy of a human head can be approximated by a multi-layer sphere model, methods being able to take the head geometry into account have been developed. *Boundary element methods* (BEM) can embed the realistic shape of the head but are based on the simplification of considering the head as an isotropic, homogeneous volume conductor having nested shell topography. *Finite element methods* (FEM) show more flexibility, supporting nearly arbitrary geometries and both isotropic and anisotropic conductivities. Furthermore, other solution approaches, e.g., *finite difference methods* or *finite volume methods*, are used, see, e.g., [72, 28, 29, 43] and [10], respectively. The BE as well as the FE methods can be implemented in different ways, which, again, have specific advantages and disadvantages. Therefore, we will run several numerical experiments in different artificial setups to demonstrate the strengths and weaknesses of the various approaches.

After shortly exposing the theoretical basics of the forward problem and sketching the derivation of a quasi-analytical solution in Chapter 1, we will present a recently proposed BE formulation, the *symmetric* BEM, promising a strong increase of accuracy, and examine its additional value in a three-layer sphere model in comparison to the well-known *double-layer* BE method in Chapter 2. We will give a short introduction to the different FE approaches, and run numerical experiments in different multi-layer sphere models where we compare both the FE methods among each other and to the symmetric BEM in Chapter 3, and aim to explicitly clarify the pros and cons of the different FE approaches. We close with an application of *leadfield inter-* and *extrapolation*, a technique originally designated to improve the accuracy and speed of BE methods. We will combine leadfield interpolation and FE methods in order to mitigate some of the specific drawbacks in Chapter 4.

1 The EEG Forward Problem

In this chapter we will derive the *partial differential equation* (PDE), which is known as the forward problem of EEG and depict solutions for few specific scenarios. We start with shortly considering physiological explanations for the creation of electrical fields in the human brain. Subsequently, we derive a simplification of the fundamental *Maxwell equations*, the so-called *quasi-static approximation*, and conclude a *Poisson equation* with *Neumann boundary conditions* for the electric potential. After presenting an adequate source model, we will shortly reflect an analytical solution approach and introduce the model assumption of approximating the head's anatomy by a *nested shell topography* with piecewise homogeneous conductivities.

1.1 Physiological Background

The electrical potential differences at the head surface measured by an EEG are an effect of electromagnetic fields induced by *ion currents* inside the brain. To understand the sources of this *bioelectromagnetism*, we will shortly consider the basic structures and elementary processes inside this highly complex organ. The human brain is composed out of 10^{11} up to 10^{12} elementary cells, the so-called *neurons* [69]. Neurons are electrically excitable cells that communicate amongst each other using electrochemical signaling. A typical neuron in the brain consists of three parts, the *soma*, which represents the cell body, the *dendrites*, and one *axon* arising at the *axon hillock* (see Figure 1.1). Each cell builds only one axon, which can reach a length between 1 μm (in the brain) up to 1 m (in the spinal chord) and branch several times, whereas several dendrites having a length of some hundred micrometers may develop. The neurons connect to each other cultivating (complex) networks, communicating via chemical transmitters at the *synapses*, where typically signals from the axon of one neuron are passed to a dendrite of another. Each neuron has about 7,000 synaptic connections to other neurons [16].
The process of signal transmission between neurons bases on the rise and fall of electric potentials at the cell membranes, established by the diffusion of ions through *ion-channels*. These potential differences cause intra- and extracellular ion currents, i.e., currents flowing inside and outside the neurons, respectively. According to the Maxwell equations of electrodynamic, the movement of electric charges gives rise to electromagnetic fields propagating through the human body. Two major patterns of membrane potentials appear in the signal transmission between neurons, *action potentials* and *post-synaptic potentials*.
When a certain threshold potential at the axon hillock of the *pre-synaptic* neuron is exceeded, the neuron "fires", i.e., a sudden change of the membrane potential consisting in an abrupt rise

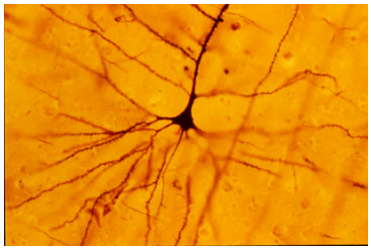

Figure 1.1: A human neocortical pyramidal neuron stained via Golgi technique. *Source: Bob Jacobs, Wikimedia Commons, CC-BY-SA-2.5; Released under the GNU Free Documentation License.*

followed by a fall of the same amplitude occurs. This action potential propagates along the axon inducing the dumping of neurotransmitters at the pre-synaptic membrane of the affiliated synapses. The diffusion of these transmitters through the neighboring *post-synaptic* membrane causes a potential change, the post-synaptic potential, in the post-synaptic neuron. This (or the sum of various) potential changes may, again, initiate an action potential in the post-synaptic neuron, i.e., the signal is passed on.
Since action potentials are too short (0.5-2 ms), insufficiently synchronized, and the far-field induced by the resulting ion currents is dominated by the quadrupole term they do not evoke an exploitable EEG signal [52, 35]. In contrast, the simultaneous generation of post-synaptic potentials with a duration of tens of milliseconds by some ten-thousand neighboring and similarly oriented neurons, corresponding to a patch of few square millimeters cortex surface, results in a measurable, dipolar electromagnetic field [46, 48]. The potential difference between the particular dendrite and the soma induces a balancing flow of ions in the liquid between the neurons. The highest concentration of similarly oriented neurons is given by the approximately 10^9 *pyramidal cells* that are mainly found in the cortex, but also in the hippocampus and the amygdala. Thus, the major contribution to the EEG signal originates from these areas.

1.2 Quasi-Static Approximation of the Maxwell Equations

We derive a quasi-static approximation of the Maxwell equations following the ideas of [30]. As a first step we note that the permeability of the head's tissue is that of free space, i.e., $\mu = \mu_0$. Then, the Maxwell equations take the form

$$\nabla \cdot E = \frac{\rho}{\epsilon_r \epsilon_0}, \tag{1.1}$$

$$\nabla \cdot B = 0, \tag{1.2}$$

$$\nabla \times E = -\frac{\partial B}{\partial t}, \tag{1.3}$$

$$\nabla \times B = \mu_0 J + \mu_0 \epsilon_r \epsilon_0 \frac{\partial E}{\partial t}, \tag{1.4}$$

where E denotes the electric field, B the magnetic field, ρ the charge density, J the current density, ϵ_0 and ϵ_r the permittivity of free space and the relative permittivity, respectively, and μ_0 the permeability of free space. In the following, we will show that the quasi-static approximation, i.e., neglecting the temporal derivatives in the Maxwell equations, is a reasonable model assumption. Using Ohm's law, $J = \sigma E$, in (1.4), we have

$$\nabla \times B = \mu_0(\sigma E + \epsilon_r \epsilon_0 \frac{\partial E}{\partial t}). \tag{1.5}$$

Since we can apply a Fourier decomposition to a general time dependent electric field, we have no loss of generality when assuming a harmonic time dependency with angular frequency ω, i.e. $E(t) = E_0 \cdot e^{-i\omega t}$, in (1.5):

$$\nabla \times B = \mu_0(\sigma E - i\epsilon_r \epsilon_0 \omega E). \tag{1.6}$$

Thus, for the quasi-static approximation to be valid, we need $|\epsilon_r \epsilon_0 \omega| \ll |\sigma|$, i.e., $|\epsilon_r \epsilon_0 \omega / \sigma| \ll 1$. With $\sigma \approx 0.3$ S/m, $\epsilon_r \approx 10^5$ and a frequency $f = \omega/2\pi \approx 100$ Hz, which is assumed as an upper bound for frequencies in neuromagnetism [30], we have $\epsilon_r \epsilon_0 \omega / \sigma \approx 2 \cdot 10^{-3} \ll 1$.
To show that we can neglect $\partial B/\partial t$ in (1.3), we take the rotation of (1.3) and with (1.4) we have

$$\nabla \times \nabla \times E = -\frac{\partial}{\partial t}(\nabla \times B) = -\mu_0 \frac{\partial}{\partial t}(\sigma E + \epsilon_r \epsilon_0 \frac{\partial E}{\partial t}) = \mu_0(i\sigma\omega - \epsilon_r \epsilon_0 \omega^2)E. \tag{1.7}$$

The solutions of this equation have a characteristic wavelength of $\lambda_c = |\mu_0 \sigma \omega (1 - \epsilon_r \epsilon_0 \omega / \sigma)|^{-1/2} \approx$ 65 m, which is much larger then the diameter of the human head, and the contribution to E can be neglected.

1.3 Derivation of the Forward Equation

With $\nabla \times E = 0$ we know that E is a gradient field and we can relate it to a scalar potential V:

$$E = -\nabla V. \tag{1.8}$$

We split the current density $J(x)$ into two parts. The primary current $J^p(x)$ is an effect of neural activity and spatially bounded in a small volume; the *passive volume* or *return current*, $J^v(x) = \sigma(x)E(x)$, flows in the whole medium as an effect of the macroscopic electric field:

$$J(x) = J^p(x) + \sigma(x)E(x) = J^p(x) - \sigma(x)\nabla V(x), \tag{1.9}$$

with the macroscopic conductivity σ being either a non-negative scalar (isotropic case) or a symmetric positive definite tensor (anisotropic case), i.e., $\sigma : \Omega \to \mathbb{R}$ or $\sigma : \Omega \to \mathbb{R}^{3\times 3}$, depending on whether the anisotropy of, e.g., white matter is taken into account or not. We denoted the head domain by Ω.

Remark 1. *We assume that the head domain Ω is open and connected. We further assume that $\partial\Omega$ is sufficient regular (we will specify this with Definition 5).*

Taking the divergence of (1.4), where we neglect the temporal derivative, together with (1.9) and exploiting $\nabla \cdot \nabla \times B = 0$ yields

$$\begin{aligned} \nabla \cdot (\sigma \nabla V) = f = \nabla \cdot J^p \qquad & \text{in } \Omega, \\ \partial_{\mathbf{n}}(\sigma V) = 0 \qquad & \text{on } \partial\Omega = \Gamma, \end{aligned} \tag{1.10}$$

where we introduced f as abstract source term. The actual definition of f depends on the choice of a source model.
The forward problem of EEG now consists of finding a solution to the above equation system (1.10) that lives in an appropriate function space. Classical solutions, i.e., solutions that are sufficiently often differentiable, can only be found under very strong assumptions, e.g., a continuous conductivity σ, which is no suitable assumption in our case. Therefore, we will search for a solution in the *Sobolev space* $H^1(\Omega)$. Existence and uniqueness of the solution of (1.10) can be proven [47, 85]:

Theorem 1. (1.10) *has an unique solution in $H^1_*(\Omega)$ when f can be expressed as*

$$f = \sum_{i=1}^{3} \frac{\partial}{\partial x_i} g_i + g_0, \qquad g_i \in L^2(\Omega), \tag{1.11}$$

where

$$H^1_*(\Omega) = \{v \in H^1(\Omega) | \int_\Omega v dx = 0\}. \tag{1.12}$$

(1.11) implies $f \in H^{-1}(\Omega)$ and in terms of J^p we have $\partial/\partial x_i (J^p)_i \in L^2(\Omega)$. $H^1_*(\Omega)$ is the quotient of $H^1(\Omega)$ taken by the space of constant functions supported on Ω, i.e., the resulting solution is up to a constant unique in $H^1(\Omega)$. The condition $\int_\Omega v dx = 0$ provides advantages for the proof of this uniqueness, but is not feasible in the implementation of BE and FE methods and is usually replaced by other conditions, e.g.:

- The value of the potential V is fixed at a certain position (node): $V(x) = c,\ x \in \Omega$,
- The mean value of V on the surface of Ω is fixed: $\int_{\partial\Omega} V(x) d\gamma(x) = d$.

1.4 The Mathematical Dipole

Next, we need to model the source term f reasonably so that it represents electrical activity in the brain. A widely used concept in bioelectromagnetism is the *mathematical* or *current dipole*, which is a good approximation for a small source viewed from a relatively large distance [15, 30, 60], since the far-field of a realistic source is mainly dipolar (cf. Section 1.1). For a dipole at position x_0 the mathematical dipole is defined by

$$J^p(x) = p \cdot \delta_{x_0}(x), \tag{1.13}$$

where δ_{x_0} is the Dirac delta distribution and p is the dipole moment. It can be illustrated as the limit case of two *electrical monopoles*, a source and a sink, with charge q and distance vector d that come infinitely close together in x_0, while the dipole moment $p = q \cdot d$ is constant:

$$p = \lim_{\substack{\|d\|\to 0 \\ q\to\infty}} \int x \cdot (q\delta_{x_0+d/2}(x) - q\delta_{x_0-d/2}(x))dx = \lim_{\substack{\|d\|\to 0 \\ q\to\infty}} q \cdot d. \tag{1.14}$$

p can then be related to the dipole term in the *multipole expansion* of the source distribution [35]. The corresponding source term f in (1.19) is given by $f = \nabla \cdot J^p = (p \cdot \nabla)\delta_{x_0}$. However, since we have

$$\delta(x) \in H^{-3/2-\epsilon}\ \forall \epsilon > 0 \qquad \text{and} \qquad D^\alpha \delta(x) \in H^{-3/2-|\alpha|-\epsilon}\ \forall \epsilon > 0 \text{ (cf. [42])}, \tag{1.15}$$

the requirements of Theorem 1 are not fulfilled.
The treatment of these singularities is the main problem when applying direct finite element methods to solve the forward problem in multi-compartment head models (see Chapter 3), while it is less critical with boundary element methods. Even though less singular source models using *Whitney forms* have been proposed [68, 53, 54], it is still today's standard to use the mathematical dipole as source model.
In the case of an unbounded, homogeneous medium with conductivity σ the resulting potential V can be calculated using the *fundamental solution* of the Poisson problem:

Definition 1. *We define*

$$G(x) \coloneqq \frac{1}{4\pi \|x\|_2} \qquad \text{for } x \in \mathbb{R}^3. \tag{1.16}$$

Remark 2. *G is the fundamental solution of the Poisson equation. It fulfills the property $-\Delta G(x) = \delta(x)$ in a distributive sense.*

Proof. cf. [35, 47].

For an isotropic conductivity σ, the solution is then given by the convolution of the source term f and G:

$$V = -\frac{1}{\sigma} f * G. \tag{1.17}$$

In the case of a mathematical dipole at position x_0 we obtain

$$\begin{aligned} V(x) = -\frac{1}{\sigma}(\nabla \cdot J^p) * G(x) = \frac{1}{\sigma}\int_{\mathbb{R}^3} (p \cdot \nabla)\delta_{x_0}(x-y) \cdot G(y)dy = \\ -\frac{1}{\sigma}\int_{\mathbb{R}^3} p\delta_{x_0}(x-y) \cdot \nabla G(y)dy = -\frac{p}{\sigma}\nabla G(x-x_0) = \frac{1}{4\pi\sigma}\frac{p \cdot (x-x_0)}{\|x-x_0\|_2^3}. \end{aligned} \tag{1.18}$$

See also [60].

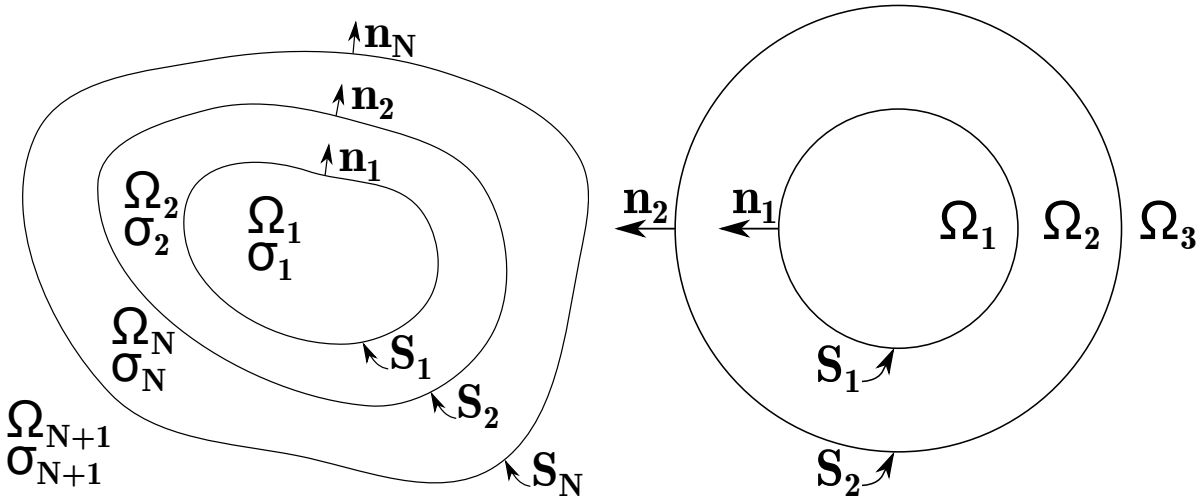

(a) Schematic N layer head model with nested shell topology

(b) Nested shell topology

Figure 1.2: BE head model and topography

1.5 BE Head Model

When applying the boundary element methods, we will assume a simplified head model consisting of the three compartments skin, skull and brain, each with constant isotropic conductivity. We further assume a nested shell topology (also referred to as hollow ball topology), i.e., skull holes caused by, e.g., the eye nerve, the brain stem or surgery, have to be neglected.
We will shortly indicate a simplified version of equation (1.10) for the special case of N nested compartments; Ω_{N+1} denotes the outside of the head ($\Omega_{N+1} = \bigcap_{i=1}^{N} \bar{\Omega}_i^{\complement}$). We assume a constant conductivity $\sigma_i \in \mathbb{R}$ in each head compartment Ω_i so that $\nabla\sigma$ is non-zero only at the boundaries $\bar{\Omega}_i \cap \bar{\Omega}_{i+1} = S_i$ (see Figure 1.2 and Subsection 2.6.2). When we further assume that no sources lie outside the head and that we have boundary conditions $[V] = 0$ and $[\sigma\partial_{\mathbf{n}}V] = 0$ with $\sigma_{N+1} = 0$ (where square brackets denote the jump of a function, see Definition 3), imposing the continuity of the potential and the current (charge) flow across boundaries, this yields the set of equations

$$\begin{aligned} \sigma_i \Delta V = f = \nabla \cdot J^p \quad & \text{in } \Omega_i, \text{ for all } i = 1, \dots, N, \\ \Delta V = 0 \quad & \text{in } \Omega_{N+1}, \\ [V]_{\Omega_j} = [\sigma\partial_{\mathbf{n}}V]_{\Omega_j} = 0 \quad & \text{on } S_j, \text{ for all } j = 1, \dots, N. \end{aligned} \tag{1.19}$$

Thus, we will have to solve the Poisson equation in each of the compartments. The solutions are linked by the jump properties. Still, the solution is only known up to a constant, which has to be fixed by an additional condition, examples were given in Section 1.3.

1.6 Analytical Solution

For some special geometries the EEG forward problem (1.19) can be solved analytically even if the conductivity of the medium is not constant, e.g., for a multi-layer sphere model. The analytical formulas allow for an easy calculation of the electric potentials under the constraint to model the human head by nested spheres of piecewise constant conductivities (see Figure 1.2). In practice, analytical solutions were (and still are) used to solve the forward problem of EEG with the major drawback that the assumption of a spherical head is rather inexact. Thereby, the model error exceeds the numerical errors of methods being able to solve the forward problem for realistically shaped head models, e.g., those presented in Chapters 2 and 3. Nevertheless,

analytical solutions are still required as an important tool to evaluate the accuracy of numerical solutions.

Different formulas to obtain an analytical solution for the EEG forward problem have been proposed. While first solutions were only valid for a constant number of spheres with isotropic conductivities [22, 34], solutions that are able to handle arbitrary many spheres and with restrictions even anisotropic conductivities are available nowadays [45, 44, 13, 91]. We will use the solution derived in [45] throughout this thesis, which enables us to treat arbitrary many spheres (and anisotropy; we however do not need this possibility in this thesis). We will shortly present the necessary formulas subsequently.

We assume a model consisting of N nested shells with radii $r_1 < r_2 < \ldots < r_N$ and constant radial and tangential conductivities $\sigma^{rad}(x) = \sigma_j^{rad} \in \mathbb{R}^+$ and $\sigma^{tan}(x) = \sigma_j^{tan} \in \mathbb{R}^+$ in each shell, $r_j < x < r_{j+1}$. We further assume that the source at position x with radial coordinate $x^r \in \mathbb{R}$ is in a more interior layer than the measurement electrode at position y_i with radial coordinate $y_i^r \in \mathbb{R}$, $i = 1, \ldots, s$, s being the number of electrodes. Then the potential evoked at y_i by a source at x with dipole moment p is given by

$$V(x, p, y_i) = \frac{1}{4\pi} \langle p, y_i \frac{S_0}{y_i^r} + x \left(\frac{S_1}{x^r} - \cos \omega_{x,y_i} \frac{S_0}{x^r} \right) \rangle \tag{1.20}$$

with ω_{x,y_i} being the angular distance between x and y_i,

$$S_0 = \frac{F_0}{x^r} \frac{\Lambda}{(1 - 2\Lambda \cos \omega_{x,y_i} + \Lambda^2)^{3/2}} + \frac{1}{x^r} \sum_{n=1}^{\infty} \left[(2n+1) R_n(x^r, y_i^r) - F_0 \Lambda^n \right] P_n'(\cos \omega_{x,y_i}), \tag{1.21}$$

$$S_1 = F_1 \frac{\Lambda \cos \omega_{x,y_i} - \Lambda^2}{(1 - 2\Lambda \cos \omega_{x,y_i} + \Lambda^2)^{3/2}} + \sum_{n=1}^{\infty} \left[(2n+1) R_n'(x^r, y_i^r) - F_1 n \Lambda^n \right] P_n(\cos \omega_{x,y_i}). \tag{1.22}$$

P_n and P_n' denote the Legendre polynomial and its derivative, respectively, and can be computed recursively; the coefficients R_n and their derivatives R_n' can be computed analytically. The definitions of F_0, F_1 and Λ are given in [45], as well as the exact derivation of the above formulas. This results in the vector of electrode potentials $(V^{ana})_i = V(x, p, y_i)$ for a dipole at position x and with dipole moment p and electrode positions y_i.

2 The Boundary Element Method

Boundary element methods are one possibility to overcome the restriction to a multi-layer sphere model. Most BE methods are limited to a nested shell topology where the interfaces between different compartments of isotropic conductivity may be realistically shaped (see Figure 1.2). A reformulation of the forward problem into a *boundary integral equation* is the basis to apply BEM. Afterwards, the resulting equations are discretized, i.e., the surfaces have to be triangulated and the unknowns are approximated by (finite) linear combinations of basis functions.
For reasons of computational complexity, BE methods are commonly used in combination with three-layered head models (see Section 1.5). Skull holes have to be neglected, amongst other things, due to the restriction of current BE implementations to nested domain topologies. Since the resulting surfaces of skin, inner skull and outer skull are relatively smooth, they can be adequately modeled by a few hundred nodes, keeping the computational demand relatively low, while at the same time the accuracy is strongly improved compared to spherical models [89]. The low computational demand was (and in some cases still is) a major advantage over FE methods. In contrast, including the CSF compartment, which was shown to have an important volume current tunneling function [76] and whose conductivity is inter-individually not varying [4], is a challenging task when using BE methods. The cortex surface, which would be needed to include the CSF compartment, has a complicatedly folded structure. A realistically shaped triangulation of the cortex surface would require at least 15,000 to 20,000 nodes to model deep sulci appropriately [79]. With 20,000 additional nodes, the computation time grows considerably, making the integration of the CSF into a BE model not feasible yet [36]. The distinction between skull spongiosa and skull compacta [12] is even more complicated, since the occurring domains are not nested. Theoretically, it is possible to deal with such topologies, but an extension of the framework would be necessary. In practice, other problems might occur, e.g., when generating the corresponding surface meshes.
Our goal in this chapter is to derive a symmetric integral representation for the Poisson problem as presented in [36], which requires miscellaneous preliminaries. We will compare the symmetric BEM to the classical double-layer BEM regarding time consumption and accuracy, subsequently. Therefore, we will briefly deduce the double-layer formulation and its discretization for reasons of completeness before we run numerical experiments in a three-layer sphere model.

2.1 Representation Theorem for Harmonic Functions

We begin this chapter by proving a theorem that relates the limit values of a harmonic function at a (closed) surface to the value of the function in- and outside this surface via the calculation of specific integrals. This identity will be of great use later on: To derive the integral representations that are underlying the BE methods, we will have to find tailored harmonic functions.
In a nutshell, we will first calculate a solution v for our source term f under the assumption of an infinite, homogeneous conductor (see Section 1.4). We will then search for a harmonic adjustment function u, i.e., $\Delta u = 0$, to obey the boundary conditions so that the potential is finally given by $V = u + v$. The *Representation Theorem* will be an important tool to gain an expression for u in terms of surface integrals.
Before indicating the Representation Theorem, we give some definitions and notations.

Definition 2 (Interior and exterior limits)**.** *The interior and exterior limits of a function*

$f : \mathbb{R}^3 \to \mathbb{R}$ at an interface Γ, f_Γ^- and f_Γ^+, are defined as

$$f_\Gamma^-(x) = \lim_{\epsilon \nearrow 0} f(x + \epsilon n), \tag{2.1}$$

$$f_\Gamma^+(x) = \lim_{\epsilon \searrow 0} f(x + \epsilon n) \qquad \text{for } x \in \Gamma, \tag{2.2}$$

with n being the unit normal vector to Γ at point $x \in \mathbb{R}^3$ (by definition pointing outwards, see Figure 1.2).

Definition 3 (Jump of a function)**.** *The jump of a function $f : \mathbb{R}^3 \to \mathbb{R}$ at an interface Γ is defined as*

$$[f]_\Gamma = f_\Gamma^- - f_\Gamma^+. \tag{2.3}$$

Notation 1 (Normal derivative)**.** *In the following we denote the partial derivative of a function $f : \mathbb{R}^3 \to \mathbb{R}$ in the direction of the unit normal vector n, $n \cdot \nabla f$, by $\partial_{\mathbf{n}} f$.*

Definition 4 (Hölder space)**.** *We define the Hölder space $\mathcal{C}^{k+\lambda}$, it consists of functions having derivatives up to order k so that the derivatives are Hölder continuous with exponent $\lambda \in (0, 1)$.*

Definition 5 (Regularity of surfaces)**.** *A subset $S \subset \mathbb{R}^3$ is called a regular surface, if for each point $p \in S$ there exists a neighborhood $V \subset \mathbb{R}^3$ of p and a map $\phi : U \to V \cap S$ of an open set $U \subset \mathbb{R}^2$ such that*

- *ϕ is a homeomorphism,*
- *ϕ is continuously differentiable*
- *ϕ is a regular patch, i.e., its* Jacobian *has full range in every point $p \in S$.*

We say that a surface S is of class $\mathcal{C}^k$ ($\mathcal{C}^{k+\lambda}$), if each of the homeomorphisms as well as their inverses are in the space $\mathcal{C}^k$ ($\mathcal{C}^{k+\lambda}$). In the following we will demand a regularity of $k = 1 + \mu$, $\mu \in (0, 1)$.

We are now able to formulate the Representation Theorem:

Theorem 2 (Representation Theorem)**.** *Let $\Omega \subset \mathbb{R}^3$ be a bounded open set with a regular boundary Γ. Let $u : (\Omega \cup (\bar{\Omega})^{\complement}) \to \mathbb{R}$ be harmonic, i.e.,*

$$\begin{aligned} \Delta u &= 0 \qquad \text{in } \Omega, \\ \Delta u &= 0 \qquad \text{in } (\bar{\Omega})^{\complement}, \end{aligned}$$

satisfy an outgoing radiation condition

$$\begin{aligned} \lim_{r \to \infty} r|u(r)| &< \infty, \\ \lim_{r \to \infty} r \frac{\partial u}{\partial r}(r) &= 0, \end{aligned} \tag{2.4}$$

and the traces of u, u_Γ^- and u_Γ^+, $(\partial_{\mathbf{n}} u)_\Gamma^-$ and $(\partial_{\mathbf{n}} u)_\Gamma^+$ all belong to $C^0(\Gamma)$.
For $y \notin \Gamma$, the following representation formula holds:

$$u(y) = \int_\Gamma G(x - y) \left[\partial_{\mathbf{n}} u(x)\right]_\Gamma d\gamma(x) - \int_\Gamma \partial_{\mathbf{n}_x}(G(x - y))[u(x)]_\Gamma d\gamma(x). \tag{2.5}$$

For $y \in \Gamma$

$$\frac{u_\Gamma^-(y) + u_\Gamma^+(y)}{2} = \int_\Gamma G(x - y) \left[\partial_{\mathbf{n}} u(x)\right]_\Gamma d\gamma(x) - \int_\Gamma \partial_{\mathbf{n}_x} G(x - y)[u(x)]_\Gamma d\gamma(x). \tag{2.6}$$

Remark 3. *The assumption regarding the traces will prohibit sources placed on compartment boundaries. This is no restriction in our case, since sources lying directly on boundaries are physiologically not reasonable.*

Before actually proving the Representation Theorem, some preliminaries are necessary. In effect, the proof of the Representation Theorem itself will reduce to a few lines. First, we remind one of the well known *Green's identities* and indicate a lemma specifying requirements for the existence of surface integrals over singular functions.

Lemma 1 (Green's second identity)**.** *Let Ω be an open, bounded set; $\Gamma := \partial\Omega$ a regular surface. Let ϕ, $\psi \in C^2(\Omega)$ and continuously continuable on Γ. Then*

$$\int_\Omega (\phi\Delta\psi - \psi\Delta\phi)dx = \int_\Gamma (\phi\partial_{\mathbf{n}}\psi - \psi\partial_{\mathbf{n}}\phi)\, d\gamma(x). \tag{2.7}$$

Proof. cf. [19].

Remark 4. *Let $\Gamma \subset \mathbb{R}^3$ be a regular surface, $f : \Gamma \to \mathbb{R}$ a function with a singularity in $x_0 \in \Gamma$ and continuous in $\Gamma\backslash\{x_0\}$.*
For $|f(x)| \leq C\|x - x_0\|_2^{-\lambda}$ with $\lambda < 2$ the improper integral of f on Γ exists.

Proof. cf. [26].

The next lemma will be the basis of the closing proof.

Lemma 2. *Let Ω as in Lemma 1 and u harmonic in Ω. Then*

$$\begin{aligned} -\int_\Gamma G(x-y)(\partial_{\mathbf{n}}u)^-_\Gamma(x)d\gamma(x) + \int_\Gamma \partial_{\mathbf{n}_x}G(x-y)u^-_\Gamma(x)d\gamma(x) \\ = \begin{cases} -u(y) \text{ if } y \in \Omega, \\ -u^-_\Gamma(y)/2 \text{ if } y \in \Gamma, \\ 0, \text{ otherwise.} \end{cases} \end{aligned} \tag{2.8}$$

Proof. We have to distinguish two situations: $y \in \Omega$ and $y \in \Gamma = \partial\Omega$.
1. $y \in \Omega$: Let B_ϵ be a ball with center y and radius ϵ so that $B_\epsilon \subsetneq \Omega$. We apply Lemma 1 with $\phi(x) = u(x)$ and $\psi(x) = G(x-y)$ in $\Omega\backslash B_\epsilon$. G is obviously continuously continuable on Γ, u by assumption. With $\Delta u = 0$ in Ω and $\Delta_x G(x-y) = -\delta(x-y)$ (see Remark 2) this yields

$$\begin{aligned} 0 &= \int_{\Omega\backslash B_\epsilon} (u(x)\Delta_x G(x-y) - G(x-y)\Delta_x u(x))\, dx \\ &\overset{(2.7)}{=} \int_{\partial(\Omega\backslash B_\epsilon)} (u(x)\partial_{\mathbf{n}_x}G(x-y) - G(x-y)\partial_{\mathbf{n}_x}u(x))\, d\gamma(x), \end{aligned} \tag{2.9}$$

where we replace $u(x) = u^-_\Gamma(x)$ for $x \in \partial\Omega = \Gamma$. Splitting up into the contributions on ∂B_ϵ and Γ gives us

$$\begin{aligned} \int_\Gamma G(x-y)\partial_{\mathbf{n}_x}u^-_\Gamma(x)d\gamma(x) - \int_\Gamma \partial_{\mathbf{n}_x}G(x-y)u^-_\Gamma(x)d\gamma(x) \\ - \int_{\partial B_\epsilon} G(x-y)\partial_{\mathbf{n}_x}u(x)d\gamma(x) + \int_{\partial B_\epsilon} \partial_{\mathbf{n}_x}G(x-y)u(x)d\gamma(x) = 0 \end{aligned} \tag{2.10}$$

Since u is harmonic in Ω, it is harmonic in $\bar{B}_\epsilon$, too, and thus $\partial_{\mathbf{n}}u(x)$ is bounded for $x \in B_\epsilon$. As $G(x-y) = \frac{1}{4\pi\epsilon}$ for $x \in \partial B_\epsilon$ we estimate

$$\begin{aligned} \left|\int_{\partial B_\epsilon} G(x-y)\partial_{\mathbf{n}}u(x)d\gamma(x)\right| &\leq \frac{1}{4\pi\epsilon}\sup_{x\in B_\epsilon}|\partial_{\mathbf{n}}u(x)| \cdot \left|\int_{\partial B_\epsilon} d\gamma(x)\right| \\ &= \epsilon \sup_{x\in B_\epsilon}|\partial_{\mathbf{n}}u(x)|\,. \end{aligned} \tag{2.11}$$

This tends to zero with $\epsilon \to 0$. The second integral on ∂B_ϵ has the value

$$\int_{\partial B_\epsilon} \partial_{\mathbf{n}_x} G(x-y)u(x)d\gamma(x) = \\ u(y)\int_{\partial B_\epsilon} \partial_{\mathbf{n}_x} G(x-y)d\gamma(x) + \int_{\partial B_\epsilon} \partial_{\mathbf{n}_x} G(x-y)(u(x)-u(y))d\gamma(x). \quad (2.12)$$

Using $n_x = (x-y)/\|x-y\|_2$ (since $x \in \partial B_\epsilon(y)$), we compute

$$\partial_{\mathbf{n}_x} G(x-y) = n_x \cdot \nabla G(x-y) = \frac{x-y}{\|x-y\|_2} \cdot \frac{-(x-y)}{4\pi\|x-y\|_2^3} = -\frac{1}{4\pi\|x-y\|_2^2}. \quad (2.13)$$

and estimate

$$\begin{aligned} \left|\int_{\partial B_\epsilon} \partial_{\mathbf{n}_x} G(x-y)(u(x)-u(y))d\gamma(x)\right| &\le \sup_{x\in B_\epsilon} |u(x)-u(y)| \cdot \left|\int_{\partial B_\epsilon} \frac{1}{4\pi\|x-y\|_2^2}\right| \\ &= \sup_{x\in B_\epsilon} |u(x)-u(y)|, \end{aligned} \quad (2.14)$$

which tends to zero since u is harmonic and thus continuous, and

$$\begin{aligned} u(y)\int_{\partial B_\epsilon} \partial_{\mathbf{n}_x} G(x-y)d\gamma(x) &= u(y)\cdot\frac{-1}{4\pi\epsilon^2}\int_{\partial B_\epsilon} d\gamma(x) \\ &= -u(y). \end{aligned} \quad (2.15)$$

2. $y \in \Gamma$: We integrate over $\Omega\backslash B_\epsilon$ with B_ϵ being a ball with center y and radius ϵ, again. Like before, we split this integral into two parts on $\Gamma\backslash B_\epsilon$ and on $\partial B_\epsilon \cap \Omega$:

$$\int_{\Gamma\backslash B_\epsilon} G(x-y)\partial_{\mathbf{n}_x} u(x)^-_\Gamma d\gamma(x) - \int_{\Gamma\backslash B_\epsilon} \partial_{\mathbf{n}_x} G(x-y)u(x)^-_\Gamma d\gamma(x) \\ - \int_{\partial B_\epsilon\cap\Omega} G(x-y)\partial_{\mathbf{n}_x} u(x)d\gamma(x) + \int_{\partial B_\epsilon\cap\Omega} \partial_{\mathbf{n}_x} G(x-y)u(x)d\gamma(x) = 0. \quad (2.16)$$

The third term can be treated similar to the first case and tends to zero for $\epsilon \to 0$. The first and second term converge to the integrals over Γ, since the singularity at y is integrable due to Remark 4. This is obvious for the first term, as $|G(x-y)\partial_{\mathbf{n}_x} u(x)^-_\Gamma| \le C\|x-y\|_2^{-1}$ for $x \in \Gamma$ where we exploit that $\partial_{\mathbf{n}_x} u^-_\Gamma$ is continuous and thus bounded. We treat the second term making use of

$$\partial_{\mathbf{n}_x} G(x-y) = n_x \cdot \frac{x-y}{\|x-y\|_2^3}. \quad (2.17)$$

Due to the demanded regularity of Γ, there exists a neighborhood of y where $x-y$ and n_x are never parallel, thus $\|n_x \cdot (x-y)\|_2 < C_1\|x-y\|_2^{1+\mu}$, $\mu > 0$ [26], and $|\partial_{\mathbf{n}_x} G(x-y)| < C_1\|x-y\|_2^{2-\mu}$ hold locally. Then $|\partial_{\mathbf{n}_x} G(x-y)u(x)^-_\Gamma| < C_2\|x-y\|_2^{2-\mu}$ holds on Γ as u^-_Γ is continuous in Γ and $\partial_{\mathbf{n}} G(x-y)$ is continuous in $B_\epsilon^{\complement}$.
Treating the fourth term as in the first case and directly using (2.13), yields

$$\int_{\partial B_\epsilon\cap\Omega} \partial_{\mathbf{n}_x} G(x-y)u(x)d\gamma(x) = \\ u(y)\int_{\partial B_\epsilon\cap\Omega} \frac{-1}{4\pi\epsilon^2} d\gamma(x) + \int_{\partial B_\epsilon\cap\Omega} \frac{-1}{4\pi\epsilon^2}(u(x)-u(y))d\gamma(x). \quad (2.18)$$

The second part converges to zero, while we compute for the first term:

$$u(y)\int_{\partial B_\epsilon} \frac{-1}{4\pi\epsilon^2} d\gamma(x) = -u(y)\cdot\frac{1}{4\pi\epsilon^2}|\partial B_\epsilon \cap \Omega|. \quad (2.19)$$

Since for small ϵ, B_ϵ is asymptotically cut into two halves of the same size by Γ, $|\partial B_\epsilon \cap \Omega|$ converges to $4\pi\epsilon^2$ and thus this term takes the limit $-u(y)/2$. □

Reconsidering the Representation Theorem, we will extend the previous lemma to unbounded domains (under certain assumptions).

Corollary 1. *Lemma 2 also holds for a function that is harmonic in $\bar{\Omega}^{\complement}$ with $-u_\Gamma^+$ instead of u_Γ^- on the left hand side and u_Γ^+ instead of u_Γ^- on the right hand side if u fulfills the outgoing radiation condition (2.4) and Ω is bounded.*

Proof. We choose a ball B_R with radius R around y large enough so that $\bar{\Omega} \cup \{y\} \subsetneq B_R$. Using Lemma 2 in $B_R \backslash \bar{\Omega}$ gives us

$$\begin{aligned} -\int_{\partial(B_R\backslash\bar{\Omega})} G(x-y)(\partial_{\mathbf{n}} u^-_{\partial(B_R\backslash\bar{\Omega})})(x)d\gamma(x) + \int_{\partial(B_R\backslash\bar{\Omega})} \partial_{\mathbf{n}_x} G(x-y)u(x)^-_{\partial(B_R\backslash\bar{\Omega})}d\gamma(x) = \\ + \int_\Gamma G(x-y)(\partial_{\mathbf{n}}u)^+_\Gamma(x)d\gamma(x) - \int_\Gamma \partial_{\mathbf{n}_x} G(x-y)u^+_\Gamma(x)d\gamma(x) \\ - \int_{\partial B_R} G(x-y)(\partial_{\mathbf{n}}u)(x)d\gamma(x) + \int_{\partial B_R} \partial_{\mathbf{n}_x} G(x-y)u(x)d\gamma(x), \end{aligned} \tag{2.20}$$

since $u^-_{\partial(B_R\backslash\bar{\Omega})}(x) = u^+_\Gamma(x)$ and $n_{x,\Gamma} = -n_{x,\partial(B_R\backslash\Omega)}$ for $x \in \Gamma$.
We show that the integrals on B_R converge to zero for $R \to \infty$:

$$\begin{aligned} \left| \int_{\partial B_R} G(x-y)(\partial_{\mathbf{n}}u)(x)d\gamma(x) \right| &\leq \sup_{x\in B_R\backslash\bar{\Omega}} |\partial_{\mathbf{n}}u(x)| \cdot \left| \int_{\partial B_R} \frac{1}{4\pi\|x-y\|} d\gamma(x) \right| \\ &\leq \sup_{x\in B_R\backslash\bar{\Omega}} |\partial_{\mathbf{n}}u(x)| \cdot \frac{1}{4\pi R} \int_{\partial B_R} d\gamma(x) \\ &= \sup_{x\in B_R\backslash\bar{\Omega}} |\partial_{\mathbf{n}}u(x)| \cdot R \\ &\xrightarrow{R\to\infty} 0 \end{aligned} \quad , \tag{2.21}$$

since $G(x-y) = 1/4\pi R$ for $x \in B_R$ and u fulfills (2.4).

$$\begin{aligned} \left| \int_{\partial B_R} \partial_{\mathbf{n}_x} G(x-y)u(x)d\gamma(x) \right| &\leq \left| \int_{\partial B_R} \frac{n_x \cdot x}{4\pi\|x-y\|} u(x)d\gamma(x) \right| \\ &\leq \sup_{x\in B_R\backslash\bar{\Omega}} |u(x)| \cdot \sup_{x\in B_R\backslash\bar{\Omega}} \frac{\|x\|}{4\pi R^3} \cdot \left| \int_{\partial B_R} d\gamma(x) \right|, \\ &= \sup_{x\in B_R\backslash\bar{\Omega}} |u(x)| \cdot sup_{x\in B_R\backslash\bar{\Omega}} \frac{\|x\|}{R} \\ &\xrightarrow{R\to\infty} 0 \end{aligned} \tag{2.22}$$

since $\|x\|/R \overset{r\to\infty}{\to} 1$ for $x \in B_R$ and u fulfills (2.4). □

The proof of the Representation Theorem now consists in simply merging our preliminaries:

Proof of Theorem 2 (Representation Theorem). Using Lemma 2 in Ω, Corollary 1 in $\bar{\Omega}^{\complement}$, and taking the sum of both expressions gives us

$$\begin{aligned} -\int_\Gamma G(x-y)(\partial_{\mathbf{n}}u)^-_\Gamma(x)d\gamma(x) + \int_\Gamma \partial_{\mathbf{n}_x} G(x-y)u^-_\Gamma(x)d\gamma(x) \\ + \int_\Gamma G(x-y)(\partial_{\mathbf{n}}u)^+_\Gamma(x)d\gamma(x) - \int_\Gamma \partial_{\mathbf{n}_x} G(x-y)u^+_\Gamma(x)d\gamma(x) \\ = -\int_\Gamma G(x-y)[\partial_{\mathbf{n}}u]_\Gamma(x)d\gamma(x) + \int_\Gamma \partial_{\mathbf{n}_x} G(x-y)[u]_\Gamma(x)d\gamma(x) \\ = \begin{cases} -u(y) \text{ if } y \in \Omega \\ -(u^-_\Gamma(y) + u^+_\Gamma(y))/2 \text{ if } y \in \Gamma. \end{cases} \end{aligned} \tag{2.23}$$

□

Having the topology of the BE head model in view (see Figure 1.2), we will extend Theorem 2 to a nested domain topology. We will compute the case of three domains here; the case of more domains follows by iteration if needed.

Corollary 2. *Let Ω_1, Ω_2 and Ω_3 be disjoint open sets such that $\bar{\Omega}_1 \cup \bar{\Omega}_2 \cup \Omega_3 = \mathbb{R}^3$, separated by regular boundaries $\partial\Omega_1 \cap \partial\Omega_2 = S_1$, $\partial\Omega_2 \cap \partial\Omega_3 = S_2$ and $\partial\Omega_1 \cap \partial\Omega_3 = \emptyset$.*
Let $u : (\Omega_1 \cup \Omega_2 \cup \Omega_3) \to \mathbb{R}$ be harmonic. Then Theorem 2 holds with $\Gamma = S_1 \cup S_2$.

Proof. We apply Lemma 2 in Ω_1 and Ω_2 (where we keep in mind that the orientation of normals on S_1 is by definition outwards pointing when integrating on S_1, but pointing from Ω_2 to Ω_1, when integrating on S_1 as part of $\partial\Omega_2$) and Corollary 1 in Ω_3.
We have

$$\int_{\partial\Omega_1} G(x-y)(\partial_{\mathbf{n}}u)^-_{\partial\Omega_1}(x)d\gamma(x) + \int_{\partial\Omega_1} \partial_{\mathbf{n}_x}G(x-y)u^-_{\partial\Omega_1}(x)d\gamma(x) =$$
$$\int_{S_1} G(x-y)(\partial_{\mathbf{n}}u)^-_{S_1}(x)d\gamma(x) + \int_{S_1} \partial_{\mathbf{n}_x}G(x-y)u^-_{S_1}(x)d\gamma(x) =$$
$$\begin{cases} -u(y) \text{ if } y \in \Omega_1, \\ -u^-_\Gamma(y)/2 \text{ if } y \in S_1, \\ 0 \text{ otherwise} \end{cases} \tag{2.24}$$

$$\int_{\partial\Omega_2} G(x-y)(\partial_{\mathbf{n}}u)^-_{\partial\Omega_2}(x)d\gamma(x) + \int_{\partial\Omega_2} \partial_{\mathbf{n}_x}G(x-y)u^-_{\partial\Omega_2}(x)d\gamma(x) =$$
$$-\int_{S_1} G(x-y)(\partial_{\mathbf{n}}u)^+_{S_1}(x)d\gamma(x) - \int_{S_1} \partial_{\mathbf{n}_x}G(x-y)u^+_{S_1}(x)d\gamma(x)$$
$$+\int_{S_2} G(x-y)(\partial_{\mathbf{n}}u)^-_{S_2}(x)d\gamma(x) + \int_{S_2} \partial_{\mathbf{n}_x}G(x-y)u^-_{S_2}(x)d\gamma(x) =$$
$$\begin{cases} -u(y) \text{ if } y \in \Omega_2, \\ -u^-_\Gamma(y)/2 \text{ if } y \in S_2, \\ -u^+_\Gamma(y)/2 \text{ if } y \in S_1, \\ 0 \text{ otherwise} \end{cases} \tag{2.25}$$

$$\int_{\partial\Omega_3} G(x-y)(\partial_{\mathbf{n}}u)^-_{\partial\Omega_3}(x)d\gamma(x) + \int_{\partial\Omega_3} \partial_{\mathbf{n}_x}G(x-y)u^-_{\partial\Omega_3}(x)d\gamma(x) =$$
$$-\int_{S_2} G(x-y)(\partial_{\mathbf{n}}u)^+_{S_2}(x)d\gamma(x) - \int_{S_2} \partial_{\mathbf{n}_x}G(x-y)u^+_{S_2}(x)d\gamma(x) =$$
$$\begin{cases} -u(y) \text{ if } y \in \Omega_3, \\ -u^+_\Gamma(y)/2 \text{ if } y \in S_2, \\ 0 \text{ otherwise} \end{cases} \tag{2.26}$$

Summing up the three contributions finishes the proof. □

Instead of representing a known harmonic function by its jump at a surface Γ as in Theorem 2, we are also able to obtain a (harmonic) function u defined on $\mathbb{R}^3\backslash\Gamma$ out of a continuous function on the particular surface:

Definition 6. *The following integral expressions are called* single- *and* double-layer potential *with* density q *and* φ*, respectively:*

$$u(y) = \int_\Gamma G(x-y)q(x)d\gamma(x), \text{ with } q \in C^0(\Gamma), \tag{2.27}$$

$$u(y) = \int_\Gamma \partial_{\mathbf{n}_x} G(x-y)\varphi(x)d\gamma(x), \text{ with } \varphi \in C^0(\Gamma). \tag{2.28}$$

The relation between the densities q and φ and the jump terms $[\partial_{\mathbf{n}} u]_\Gamma$ and$[u]_\Gamma$ will be resolved in Corollary 3 and 4.

2.2 Properties of Single and Double Layer Potential

To gain the symmetric integral representation (see Section 2.3) we aim to express the adjustment function u as the sum of a single- and a double-layer potential. In this section we will present some continuity properties of these potentials that will be needed for the derivation of the integral representation, and show that the representation in terms of a single- and double-layer potential is unique. Additionally, we will introduce a set of operators corresponding to the single- and double-layer potential and their derivatives, respectively.

Theorem 3. *The single-layer potential* (2.27) *is continuous with respect to* y *in* $\mathbb{R}^3$ *(especially when crossing the surface* Γ*). Its normal derivatives have discontinuities when crossing* Γ*. Their limit values on both sides of* Γ *are*

$$\partial_{\mathbf{n}} u_\Gamma^-(y) = \frac{q(y)}{2} + \int_\Gamma \partial_{\mathbf{n}_y} G(x-y)q(x)d\gamma(x), \tag{2.29}$$

$$\partial_{\mathbf{n}} u_\Gamma^+(y) = -\frac{q(y)}{2} + \int_\Gamma \partial_{\mathbf{n}_y} G(x-y)q(x)d\gamma(x), \quad \text{for } y \in \Gamma. \tag{2.30}$$

The double-layer potential (2.28) *has a discontinuity when crossing* Γ*. If* $\varphi \in C^0(\Gamma)$*, the corresponding limit values on both sides of* Γ *are*

$$u_\Gamma^-(y) = -\frac{\varphi(y)}{2} + \int_\Gamma \partial_{\mathbf{n}_x} G(x-y)\varphi(x)d\gamma(x), \tag{2.31}$$

$$u_\Gamma^+(y) = \frac{\varphi(y)}{2} + \int_\Gamma \partial_{\mathbf{n}_x} G(x-y)\varphi(x)d\gamma(x), \quad \text{for } y \in \Gamma. \tag{2.32}$$

The normal derivative of a double-layer potential is continuous when crossing Γ*. It is given by an improper integral and can be formally written as*

$$\partial_{\mathbf{n}} u(y) = \int_\Gamma \partial^2_{\mathbf{n}_x,\mathbf{n}_y} G(x-y)\varphi(x)d\gamma(x), \quad \text{for } y \in \Gamma. \tag{2.33}$$

Proof. cf. [26] or [47], Theorem 3.1.2.

Definition 7. *Four integral operators (*$\mathcal{S}$*,* $\mathcal{D}$*,* $\mathcal{D}^*$*,* $\mathcal{N}$*) on the surface* Γ *have appeared so far. They are:*

$$\begin{aligned}
\mathcal{S}u &= \int_\Gamma G(x-y)u(x)d\gamma(x),\\
\mathcal{D}u &= \int_\Gamma \partial_{\mathbf{n}_x} G(x-y)u(x)d\gamma(x),\\
\mathcal{D}^*u &= \int_\Gamma \partial_{\mathbf{n}_y} G(x-y)u(x)d\gamma(x),\\
\mathcal{N}u &= \int_\Gamma \partial^2_{\mathbf{n}_x,\mathbf{n}_y} G(x-y)u(x)d\gamma(x).
\end{aligned} \tag{2.34}$$

Remark 5. *The operator $\mathcal{D}^*$ is the adjoint of the operator $\mathcal{D}$ with respect to the $L^2(\Gamma)$ scalar product (defined by $\langle f, g\rangle \coloneqq \int_\Gamma f(x)g(x)d\gamma(x),\ f, g \in L^2(\Gamma)$).*

Proof. cf. [47], p. 116, 119.

Corollary 3. *Any potential u that is the sum of a single-layer potential with density q and a double-layer potential with density φ, i.e., $u = \mathcal{S}q + \mathcal{D}\varphi$ is such that $q = [\partial_{\mathbf{n}} u]_\Gamma$ and $\varphi = -[u]_\Gamma$.*

Proof. Since the single-layer potential and the normal derivative of the double-layer potential are continuous across Γ, the calculation of the jump terms reduces to subtracting (2.30) and (2.29) and (2.32) and (2.31), respectively. □

We will proof the uniqueness of this representation without exploiting the jump properties of single- and double-layer potential as a consequence of Theorem 4 in Corollary 4. Therefore, we will make use of the *Calderon projectors*:

Theorem 4. *Let us denote by $\mathcal{H}$ the operator*

$$\mathcal{H} = \begin{pmatrix} -\mathcal{D} & \mathcal{S} \\ -\mathcal{N} & \mathcal{D}^* \end{pmatrix} \tag{2.35}$$

The associated operators

$$\mathcal{C}_{int} = \frac{\mathcal{I}}{2} + \mathcal{H}, \qquad \mathcal{C}_{ext} = \frac{\mathcal{I}}{2} - \mathcal{H} \tag{2.36}$$

are projectors and complementary, i.e., they satisfy

$$\mathcal{C}_{ext}^2 = \mathcal{C}_{ext}, \qquad \mathcal{C}_{int}^2 = \mathcal{C}_{int}, \qquad \mathcal{C}_{int} + \mathcal{C}_{ext} = \mathcal{I}. \tag{2.37}$$

They are called Calderon projectors.

Remark 6. *The identities* (2.37) *are equivalent to the set of relations*

$$\mathcal{H}^2 = \frac{\mathcal{I}}{4} \tag{2.38}$$

or more explicitly

$$\mathcal{D}\mathcal{S} = \mathcal{S}\mathcal{D}^*, \qquad \mathcal{N}\mathcal{D} = \mathcal{D}^*\mathcal{N}, \tag{2.39}$$

$$\mathcal{D}^2 - \mathcal{S}\mathcal{N} = \frac{\mathcal{I}}{4}, \qquad \mathcal{D}^{*2} - \mathcal{N}\mathcal{S} = \frac{\mathcal{I}}{4}. \tag{2.40}$$

Proof. cf. [47], Theorem 3.1.3.

Proof of Theorem 4. The proof follows [47], Proof of Theorem 3.1.3. Let us consider a potential of the form

$$u = \mathcal{S}q - \mathcal{D}\varphi, \quad q, \varphi \in C_0(\Gamma). \tag{2.41}$$

We identify $\varphi = [u]_\Gamma$ and $q = [\partial_{\mathbf{n}} u]_\Gamma$ corresponding to Theorem 2. We conclude the identities

$$u_\Gamma^+ = -\left(\frac{\mathcal{I}}{2} + \mathcal{D}\right)\varphi + \mathcal{S}q, \tag{2.42}$$

$$\partial_{\mathbf{n}} u_\Gamma^+ = -\mathcal{N}\varphi + \left(-\frac{\mathcal{I}}{2} + \mathcal{D}^*\right) q. \tag{2.43}$$

The first identity follows directly from (2.6) when exploiting the definition of $[u]_\Gamma = \varphi$; the second is gained when taking the normal derivative on both sides of (2.42) and interchanging integration and differentiation.

(2.42) and (2.43) can be shortened using the definition of $\mathcal{H}$ and C_{ext}, respectively:

$$\begin{bmatrix} -u_\Gamma^+ \\ -\partial_{\mathbf{n}} u_\Gamma^+ \end{bmatrix} = \left(\frac{\mathcal{I}}{2} - \mathcal{H}\right) \cdot \begin{bmatrix} \varphi \\ q \end{bmatrix} = \mathcal{C}_{ext} \cdot \begin{bmatrix} \varphi \\ q \end{bmatrix}. \tag{2.44}$$

We define a potential v given by

$$v = -\mathcal{S}\partial_{\mathbf{n}} u_\Gamma^+ + \mathcal{D} u_\Gamma^+. \tag{2.45}$$

Theorem 2 shows that v vanishes in Ω and takes the value u in $\bar{\Omega}^{\complement}$. Thus, the exterior limits of v at the surface Γ are u_Γ^+ and $\partial_{\mathbf{n}} u_\Gamma^+$.
Applying $\mathcal{C}_{ext}$ on $([v]_\Gamma, [\partial_{\mathbf{n}} v]_\Gamma) = (-u_\Gamma^+, -\partial_{\mathbf{n}} u_\Gamma^+)$ yields $(u_\Gamma^+, \partial_{\mathbf{n}} u_\Gamma^+)$ (replace φ and q by u_Γ^+ and $\partial_{\mathbf{n}} u_\Gamma^+$ in (2.42) and (2.43), respectively). Therefore, $\mathcal{C}_{ext}$ is a projector.
With $\mathcal{C}_{ext}$ being a projector, $\mathcal{C}_{int}$ is a projector, too, as $\mathcal{C}_{int} = \mathcal{I} - \mathcal{C}_{ext}$. $\mathcal{C}_{int}$ projects to the kernel of $\mathcal{C}_{ext}$ and vice versa. □

Corollary 4. *The integral representation $u = \mathcal{S}q - \mathcal{D}\varphi$ is unique.*

Proof. We note that the Calderon projectors $\mathcal{C}_{int}$ and $\mathcal{C}_{ext}$ project the jumps of u and its normal derivative at the boundary Γ, $(\varphi, q) = ([u]_\Gamma, [\partial_{\mathbf{n}} u]_\Gamma)$, to the unique interior and exterior limits of u and $\partial_{\mathbf{n}} u$. The Representation Theorem shows that these limits already define u in Ω and $\Omega^{\complement}$, respectively. We conclude that the integral representation $u = \mathcal{S}q - \mathcal{D}\varphi$ is unique. □

Finally, we indicate some regularity properties of the integral operators in Definition 7, which will be of use in Subsection 2.4.2.

Remark 7. *The four previously defined integral operators have certain properties with regard to the regularity of their arguments:*

- *the operator $\mathcal{S}$ increases the regularity of its argument by one,*
- *the operators $\mathcal{D}$ and $\mathcal{D}^*$ do not change it,*
- *the operator $\mathcal{N}$ decreases the regularity of its argument by one.*

Proof. cf. [47] Theorem 3.3.1, 3.3.2.

We further introduce restrictions of these operators:

Notation 2. *The operator $\mathcal{S}_{i,j}$ is a restriction of the operator $\mathcal{S}$. It acts on a function $u : S_j \to \mathbb{R}$ and yields a function $\mathcal{S}_{i,j}u : S_i \to \mathbb{R}$:*

$$\begin{aligned} \mathcal{S}_{i,j} &: (u : S_j \to \mathbb{R}) \to (\tilde{u} : S_i \to \mathbb{R}), \\ \tilde{u} &\coloneqq \mathcal{S}u|_{S_i} = \int_{S_j} G(x-y)u(x)d\gamma(x)\Big|_{S_i}. \end{aligned} \tag{2.46}$$

In the same manner we define $\mathcal{D}_{i,j}$, $\mathcal{D}_{i,j}^*$ and $\mathcal{N}_{i,j}$.
We will further use the notation $\mathcal{S}_{\partial\Omega_i} \coloneqq \mathcal{S}_{i,i} + \mathcal{S}_{i-1,i} - \mathcal{S}_{i,i-1} - \mathcal{S}_{i-1,i-1}$ and analogous for $\mathcal{D}$, $\mathcal{D}^*$ and $\mathcal{N}$.

2.3 Symmetric Integral Representation

We will now derive the symmetric integral representation for the EEG forward problem (1.19) closely following the ideas of [36], and present the resulting matrix equations in a clearly arranged way. The source singularity will be treated in the framework of *Newtonian potentials* (in this case also called *Coulomb potentials*), which are, e.g., briefly described in [27].

As already mentioned, the idea is to eliminate the singularity at the source position using the fundamental solution of the Poisson equation. We compute a homogeneous solution v, which takes the source term f into account, but does not respect the boundary conditions necessarily. Then, we search for a harmonic function u so that $V = u + v$ fulfills both the boundary conditions and solves the Poisson equation $\sigma_i \Delta V = f$ in every Ω_i.
There are different possibilities to express the harmonic function u. Besides the possibility to gain the integral representation for the single- or double-layer approach, we will choose a third way exploiting both single- and double-layer potentials. For reasons of completeness, we will shortly deduce the double-layer approach afterwards, since we want to compare the two approaches regarding their accuracy later in this chapter.

2.3.1 Homogeneous Solution

To obtain the homogeneous solution of (1.19), we decompose the source term f into its contributions from each of the Ω_i, $f = \sum_{i=1}^{N} f_{\Omega_i}$ with $f_{\Omega_i} = f \cdot \mathbb{1}_{\Omega_i}$ and $\mathbb{1}_{\Omega_i}$ being the indicator function of Ω_i, $i = 1, ..., N$. By definition there are no sources in Ω_{N+1} and we assume that there are also no sources directly on any of the boundaries $S_i = \partial\Omega_i \cap \partial\Omega_{i+1}$ (see Remark 3).
Since G is a fundamental solution for the Poisson problem (see Remark 2), we can calculate the homogeneous medium solution for each partial source term f_{Ω_i} using convolution, $v_{\Omega_i}(x) = -f_{\Omega_i} * G(x)$. Considering $f_{\Omega_i} \equiv 0$ in $\Omega_i^{\complement}$, the v_{Ω_i} are obviously harmonic in $\Omega_i^{\complement}$, $i = 1, ..., N$.

Notation 3. *We will use the abbreviation $[\ldots]_i = [\ldots]_{S_i}$ in the following. We will further use the abbreviation $[\ldots]_{\partial\Omega_i} = [\ldots]_i \cdot \mathbb{1}_{S_i} - [\ldots]_{i-1} \cdot \mathbb{1}_{S_{i-1}}$. If internal and external limit at a surface S_i coincide for a function f, we use the notation f_{S_i} for the joint limit. Thus, $f_{S_i} : S_i \to \mathbb{R}$.*

2.3.2 Symmetric Approach

We consider in each $\Omega_1, \ldots, \Omega_N$ the function

$$u_{\Omega_i} = \begin{cases} V - v_{\Omega_i}/\sigma_i, \text{ in } \Omega_i, \\ \quad -v_{\Omega_i}/\sigma_i, \text{ in } \mathbb{R}^3 \backslash \bar{\Omega}_i. \end{cases} \tag{2.47}$$

Obviously, each u_{Ω_i} is harmonic in $\mathbb{R}^3 \backslash \partial\Omega_i$, since an application of the Laplace operator Δ to V and v yields the particular source distribution f_{Ω_i}, which is non-zero only in Ω_i and equal for V and v. Considering the orientations of normals, the jumps of u_{Ω_i} across S_i satisfy the relations

$$[u_{\Omega_i}]_i = V_{S_i}, \qquad [u_{\Omega_i}]_{i-1} = -V_{S_{i-1}}, \tag{2.48}$$

and the jumps of their derivatives satisfy

$$[\partial_{\mathbf{n}} u_{\Omega_i}]_i = (\partial_{\mathbf{n}} V)^-_{S_i}, \qquad [\partial_{\mathbf{n}} u_{\Omega_i}]_{i-1} = -(\partial_{\mathbf{n}} V)^+_{S_{i-1}}. \tag{2.49}$$

We define $p_{S_i} = \sigma_i [\partial_{\mathbf{n}} u_{\Omega_i}]_i = \sigma_i (\partial_{\mathbf{n}} V)^-_{S_i}$. Since $[\sigma \partial_{\mathbf{n}} V] = 0$, we have $p_{S_i} = \sigma_i (\partial_{\mathbf{n}} V)^-_{S_i} = \sigma_{i+1} (\partial_{\mathbf{n}} V)^+_{S_i}$ at the interface S_i.
u_{Ω_i} is harmonic in $\mathbb{R}^3 \backslash \partial\Omega_i$ due to its definition and satisfies (2.4). Applying Theorem 2 yields the internal limit of u_{Ω_i} on S_i:

$$(u_{\Omega_i})^-_{S_i} = \frac{[u_{\Omega_i}]_{\partial\Omega_i}}{2} - \mathcal{D}_{\partial\Omega_i} [u_{\Omega_i}]_{\partial\Omega_i} + \mathcal{S}_{\partial\Omega_i} [\partial_{\mathbf{n}} u_{\Omega_i}]_{\partial\Omega_i}. \tag{2.50}$$

We split up the jump terms across $\partial\Omega_i = S_{i-1} \cup S_i$ into their contributions on each surface. We further take into account identities (2.48) and obtain

$$(V - v_{\Omega_i}/\sigma_i)^-_{S_i} = (u_{\Omega_i})^-_{S_i} = \frac{V_{S_i}}{2} + \mathcal{D}_{i,i-1} V_{S_{i-1}} - \mathcal{D}_{i,i} V_{S_i} - \sigma_i^{-1} \mathcal{S}_{i,i-1} p_{S_{i-1}} + \sigma_i^{-1} \mathcal{S}_{i,i} p_{S_i}. \tag{2.51}$$

Similarly, we find the external limit

$$(V - v_{\Omega_{i+1}}/\sigma_{i+1})^+_{S_i} = (u_{\Omega_{i+1}})^+_{S_i} = \frac{V_{S_i}}{2} + \mathcal{D}_{i,i}V_{S_i} - \mathcal{D}_{i,i+1}V_{S_{i+1}} - \sigma_{i+1}^{-1}\mathcal{S}_{i,i}p_{S_i} + \sigma_{i+1}^{-1}\mathcal{S}_{i,i+1}p_{S_{i+1}}. \quad (2.52)$$

We subtract (2.51) and (2.52); under the assumption that V is continuous across S_i (see (1.19)) and exploiting that $v_{\Omega_{i+1}}$ and v_{Ω_i} are continuous across S_i, too, we gain

$$\sigma_{i+1}^{-1}(v_{\Omega_{i+1}})_{S_i} - \sigma_i^{-1}(v_{\Omega_i})_{S_i} = \mathcal{D}_{i,i-1}V_{S_{i-1}} - 2\mathcal{D}_{i,i}V_{S_i} + \mathcal{D}_{i,i+1}V_{S_{i+1}} - \sigma_i^{-1}\mathcal{S}_{i,i+1}V_{S_{i+1}} - \sigma_i^{-1}\mathcal{S}_{i,i-1}p_{S_{i-1}} + (\sigma_i^{-1} + \sigma_{i-1}^{-1})\mathcal{S}_{i,i}p_{S_i} - \sigma_{i+1}^{-1}\mathcal{S}_{i,i+1}p_{S_{i+1}}, \quad (2.53)$$

for $i = 1, \dots, N$. As internal and external limit of v do not differ, we do not explicitly distinguish between the inner and outer limit values on the left hand side.
We evaluate the quantities $(\sigma_i\partial_{\mathbf{n}}u_{\Omega_i})^-_{S_i} = (p - \partial_{\mathbf{n}}v_{\Omega_i})^-_{S_i}$ and $(\sigma_{i+1}\partial_{\mathbf{n}}u_{\Omega_{i+1}})^+_{S_i} = (p - \partial_{\mathbf{n}}v_{\Omega_{i+1}})^+_{S_i}$ in the same manner, making use of the Representation Theorem and subtracting the resulting expressions, and obtain

$$(\partial_{\mathbf{n}}v_{\Omega_{i+1}})_{S_i} - (\partial_{\mathbf{n}}v_{\Omega_i})_{S_i} = \sigma_i\mathcal{N}_{i,i-1}V_{S_{i-1}} - (\sigma_i + \sigma_{i+1})\mathcal{N}_{i,i}V_{S_i} + \sigma_{i+1}\mathcal{N}_{i,i+1}V_{S_{i+1}} - \mathcal{D}^*_{i,i-1}p_{S_{i-1}} + 2\mathcal{D}^*_{i,i}p_{S_i} - \mathcal{D}^*_{i,i+1}p_{S_{i+1}}, \quad (2.54)$$

for $i = 1, \dots, N$.
We exploit these quantities for each surface S_i, $i = 1, \dots, N$. After introducing the abbreviations

$$\mathcal{A}_i \coloneqq \begin{bmatrix} \sigma_{i,i+1}\mathcal{N}_{ii} & -2\mathcal{D}^*_{ii} \\ -2\mathcal{D}_{ii} & \sigma_{1,2}^{-1}\mathcal{S}_{11} \end{bmatrix}, \quad \mathcal{B}_{i,j} \coloneqq \begin{bmatrix} -\sigma_j\mathcal{N}_{ij} & \mathcal{D}^*_{ij} \\ \mathcal{D}_{ij} & -\sigma_j^{-1}\mathcal{S}_{ij} \end{bmatrix}, \quad \mathcal{B}^*_{j,i} \coloneqq \begin{bmatrix} -\sigma_j\mathcal{N}_{ji} & \mathcal{D}^*_{ji} \\ \mathcal{D}_{ji} & -\sigma_j^{-1}\mathcal{S}_{ji} \end{bmatrix},$$
$$z_i \coloneqq \begin{bmatrix} V_{S_i} \\ p_{S_i} \end{bmatrix}, \quad d_i \coloneqq \begin{bmatrix} (\partial_{\mathbf{n}}v_{\Omega_i})_{S_i} - (\partial_{\mathbf{n}}v_{\Omega_{i+1}})_{S_i} \\ \sigma_{i+1}^{-1}(v_{\Omega_{i+1}})_{S_i} - \sigma_i^{-1}(v_{\Omega_i})_{S_i} \end{bmatrix},$$

$\sigma_{i,j}$ for the sums $\sigma_i + \sigma_j$ and $\sigma_{i,j}^{-1} = \sigma_i^{-1} + \sigma_j^{-1}$, where $\mathcal{B}_{i,j} = \mathcal{B}^*_{j,i}$, this yields the equation system

$$\underbrace{\begin{bmatrix} \mathcal{B}^*_{1,0} & \mathcal{A}_1 & \mathcal{B}_{1,2} & & & & \\ & \mathcal{B}^*_{2,1} & \mathcal{A}_2 & \mathcal{B}_{2,3} & & & \\ & & \ddots & \ddots & \ddots & & \\ & & & \mathcal{B}^*_{N-1,N-2} & \mathcal{A}_{N-1} & \mathcal{B}_{N-1,N} & \\ & & & & \mathcal{B}^*_{N,N-1} & \mathcal{A}_N & \mathcal{B}_{N,N+1} \end{bmatrix}}_{\mathcal{T}} \cdot \underbrace{\begin{bmatrix} z_0 \\ z_1 \\ z_2 \\ \vdots \\ z_{N-1} \\ z_N \\ z_{N+1} \end{bmatrix}}_{z} = \underbrace{\begin{bmatrix} d_1 \\ d_2 \\ \vdots \\ d_{N-1} \\ d_N \end{bmatrix}}_{d} \quad (2.55)$$

We notice that terms corresponding to the non-existing surfaces S_0 and S_{N+1} appear and have to be set to zero. p_{S_N} must be set to zero, too, since $\sigma_{N+1} = 0$ implies $p_{S_N} = 0$. Thus, the vanishing conductivity is taken into account by deleting the last line and column of the matrix (and the last entries of z and d). The equation system is then given by

$$\underbrace{\begin{bmatrix} \mathcal{A}_1 & \mathcal{B}_{1,2} & 0 & \dots & 0 \\ \mathcal{B}^*_{2,1} & \mathcal{A}_2 & \ddots & \ddots & \vdots \\ 0 & \ddots & \ddots & \ddots & 0 \\ \vdots & \ddots & \ddots & \mathcal{A}_{N-1} & (\mathcal{B}_{N-1,N})_{:,1} \\ 0 & \dots & 0 & (\mathcal{B}^*_{N,N-1})_{1,:} & (\mathcal{A}_N)_{1,1} \end{bmatrix}}_{\bar{\mathcal{T}}} \cdot \underbrace{\begin{bmatrix} z_1 \\ z_2 \\ \vdots \\ z_{N-1} \\ (z_N)_1 \end{bmatrix}}_{\bar{z}} = \underbrace{\begin{bmatrix} d_1 \\ d_2 \\ \vdots \\ d_{N-1} \\ (d_N)_1 \end{bmatrix}}_{\bar{d}}, \quad (2.56)$$

where the truncated matrices/vectors are given by

$$(\mathcal{A}_N)_{1,1} = \sigma_N \mathcal{N}_{N,N}, \quad (\mathcal{B}_{N-1,N})_{:,1} = \begin{bmatrix} -\sigma_N \mathcal{N}_{N-1,N} \\ \mathcal{D}_{N-1,N} \end{bmatrix}, \quad (\mathcal{B}^*_{N,N-1})_{1,:} = \begin{bmatrix} -\sigma_N \mathcal{N}_{N,N-1} & \mathcal{D}^*_{N-N-1} \end{bmatrix},$$
$$(z_N)_1 = V_{S_N}, \qquad (d_N)_1 = (\partial_{\mathbf{n}} v_{\Omega_N})_{S_N}.$$

The resulting matrix $\bar{\mathcal{T}}$ is tridiagonal, i.e., each surface only interacts with its neighbors, at the cost of introducing two sets of unknowns, V_{S_i} and p_{S_i}. Therefore, the matrix is larger than those for the double-layer approach, which will be derived later on. However, the resulting matrix after the discretization of the equation system will additionally be symmetric (see Subsection 2.4.2). The resulting tridiagonal and symmetric structure (in contrast to the fully populated, unsymmetric matrix of the double-layer approach) leads to a comparable number of elements that actually has to be stored and calculated.

2.4 Discretization and Implementation of the Symmetric BEM

The symmetric BEM is implemented in the open-source software package *OpenMEEG* [1, 23, 36]. The description of discretization and implementation will follow these papers. To solve equation (2.56) we turn it into a linear equation system. The first step is to divide the surfaces into small regions, the so-called *elements*. Next, basis functions are defined, being non-zero only on few elements. The potential V is then approximated by a (finite) linear combination of basis functions. Finally, the continuous equation is integrated over a set of *test functions*, yielding a linear equation system.

2.4.1 Discretization of the Boundaries

Surfaces are commonly represented by triangular meshes. As we lose regularity of the surfaces when discretizing, we have to expand the results derived previously in this chapter (especially Theorem 2/Corollary 2) to the concept of *weak regularity*. Illustratively, the concept of weak regularity states that the set of singular points, i.e., the discontinuities of the surface, is of zero measure. It is directly clear from this definition that the validity of the previous results is not affected as long as we do not evaluate functions explicitly in the singular points (since the edges of the surface triangles are of measure zero). Nevertheless, formulas to evaluate function values in the singular points exist [41]. We will avoid this by using a *Galerkin method* for the symmetric BEM, which does not evaluate functions pointwise (in contrast to, e.g., the *collocation method*, which will be used with the double-layer approach).

2.4.2 Discretization of the Integral Equation

Our next step in order to solve the forward problem is to discretize the continuous integral equations (2.56), and gain a set of discrete equations which can then be solved for the potential V.

First, we will discretize the unknowns, using a finite number of basis functions. Since we have two unknowns, the potential V and its derivative p, involved, we will choose the basis functions in a way that represents their relation. Two commonly used sets of basis functions are the spaces $P0$ and $P1$, whose elements have the following properties (when defined on a triangulated surface):

Remark 8. *A function $\psi_i \in P0$ is 1 on triangle T_i and 0 elsewhere:*

$$\psi_i(x) = \begin{cases} 1 & \text{if } x \in T_i, \\ 0 & \text{otherwise}, \end{cases} \tag{2.57}$$

A function $\phi_i \in P1$ is 1 on vertex i, 0 on all other vertices and linear on each triangle:

$$\phi_i(x) = \begin{cases} \frac{\det(x_1(T_j),x_2(T_j),x)}{\det(x_1(T_j),x_2(T_j),x_3(T_j))} & \text{if } x \in T_j,\ T_j \in \mathcal{T}_i, \\ 0, & \text{otherwise}, \end{cases} \tag{2.58}$$

where we introduced $\mathcal{T}_i \coloneqq \{T_k | i \text{ is vertex of } T_k\}$, and $x_l(T_j)$, $l = 1,2,3$, are the vertices of triangle T_j so that $x_3(T_j)$ corresponds to vertex i. The functions $\phi_i \in P1$ are also called piecewise linear Lagrange functions (hat functions).
In the following a superscript $^{(l)}$ will denote the surface S_l on which a function ψ_i or ϕ_i lives.

V will be approximated using $P1$ basis functions while $P0$ basis functions will be used for approximating p. This is a reasonably choice, since p is the normal derivative of V and $P0$ functions are the restriction of the derivative of a $P1$ function to one triangle. This gives us

$$V_{S_k} = \sum_i x_i^{(k)} \phi_i^{(k)}, \qquad p_{S_k} = \sum_i y_i^{(k)} \psi_i^{(k)}. \tag{2.59}$$

Next, we will integrate each of the integral equations over test functions $\tilde{\varphi}_j$. The easiest choice for $\tilde{\varphi}_j$ would be Dirac functions δ_j, which would lead to the collocation method, giving us a pointwise equality in few chosen points; usually the mass centers of the triangles (collocation with piecewise constant interpolation) or the triangle vertices (collocation with linear interpolation). With a Galerkin method, the pointwise equality is replaced by an equality in the mean sense. Therefore, we choose $P0$ and $P1$ functions as test functions.
In order to balance the approximation errors for the potential and its derivative, we keep the regularity properties of the integral operators exposed in Remark 7 in mind, since regularity is closely related to the approximation order [67]. We reconsider that (2.53) concerns the potential (a continuous function) and (2.54) the flow, i.e., the normal derivative of the potential. Thus, we multiply (2.53) by $P0$ test functions ψ_i and (2.54) by $P1$ test functions ϕ_i.
We remind the definition of the L^2-scalar product $\langle ., . \rangle$ on a surface S:

Notation 4.

$$\begin{aligned} \langle u, v \rangle &: L^2(S) \times L^2(S) \to \mathbb{R}, \\ \langle u, v \rangle &\coloneqq \int_S u(x) \cdot v(x) dx \end{aligned} \tag{2.60}$$

and get the equations

$$\begin{aligned} \langle \sigma_{k+1}^{-1} v_{\Omega_{k+1}} - \sigma_k^{-1} v_{\Omega_k}, \psi_i^{(k)} \rangle = \\ \sum_j x_j^{(k-1)} \langle \mathcal{D}_{k,k-1} \phi_j^{(k-1)}, \psi_i^{(k)} \rangle + \sum_j x_j^{(k+1)} \langle \mathcal{D}_{k,k+1} \phi_j^{(k+1)}, \psi_i^{(k)} \rangle \\ + \left(\sigma_k^{-1} + \sigma_{k+1}^{-1}\right) \sum_j y_j^{(k)} \langle \mathcal{S}_{k,k} \psi_j^{(k)}, \psi_i^{(k)} \rangle - \sigma_k^{-1} \sum_j y_j^{(k-1)} \langle \mathcal{S}_{k,k-1} \psi_j^{(k-1)}, \psi_i^{(k)} \rangle \\ - \sigma_{k+1}^{-1} \sum_j y_j^{(k+1)} \langle \mathcal{S}_{k,k+1} \psi_j^{(k+1)}, \psi_i^{(k)} \rangle - 2 \sum_j x_j^{(k)} \langle \mathcal{D}_{k,k} \phi_j^{(k)}, \psi_i^{(k)} \rangle \end{aligned} \tag{2.61}$$

and

$$\begin{aligned} \langle \partial_{\mathbf{n}} v_{\Omega_{k+1}} - \partial_{\mathbf{n}} v_{\Omega_k}, \phi_i^{(k)} \rangle = \\ \sigma_k \sum_j x_j^{(k-1)} \langle \mathcal{N}_{k,k-1} \phi_j^{(k-1)}, \phi_i^{(k)} \rangle + \sigma_{k+1} \sum_j x_j^{(k+1)} \langle \mathcal{N}_{k,k+1} \phi_j^{(k+1)}, \phi_i^{(k)} \rangle \\ - (\sigma_k + \sigma_{k+1}) \sum_j x_j^{(k)} \langle \mathcal{N}_{k,k} \phi_j^{(k)}, \phi_i^{(k)} \rangle - \sum y_j^{(k-1)} \langle \mathcal{D}_{k,k-1}^* \psi_j^{(k-1)}, \phi_i^{(k)} \rangle \\ - \sum_j y_j^{(k+1)} \langle \mathcal{D}_{k,k+1}^* \psi_j^{(k+1)}, \phi_i^{(k)} \rangle, + 2 \sum_j y_j^{(k)} \langle \mathcal{D}_{k,k}^* \psi_j^{(k)}, \phi_i^{(k)} \rangle, \end{aligned} \tag{2.62}$$

both for all $k = 1, \ldots, N$.
We note that all scalar products on the right hand sides are of the same approximation order, as result of the operator properties. In each case the scalar product of a function of the order of a $P1$ function with a function of the order of a $P0$ function is executed. Furthermore, the approximation orders of the left hand sides of the above equations are comparable.
If we express this set of equations in (already truncated) matrix form, cf. (2.56), we have

$$\underbrace{\begin{bmatrix} A_1 & B_{1,2} & 0 & \ldots & 0 \\ B_{2,1}^* & A_2 & \ddots & \ddots & \vdots \\ 0 & \ddots & \ddots & \ddots & 0 \\ \vdots & \ddots & B_{N-2,N-1}^* & A_{N-1} & (B_{N-1,N})_{:,1} \\ 0 & \ldots & 0 & (B_{N,N-1}^*)_{1,:} & (A_N)_{1,1} \end{bmatrix}}_{T} \cdot \underbrace{\begin{bmatrix} z_1 \\ z_2 \\ \vdots \\ z_{N-1} \\ (z_N)_1 \end{bmatrix}}_{z} = \underbrace{\begin{bmatrix} d_1 \\ d_2 \\ \vdots \\ d_{N-1} \\ (d_N)_1 \end{bmatrix}}_{d} \tag{2.63}$$

with

$$A_i = \begin{bmatrix} (\sigma_i + \sigma_{i+1})N_{i,i} & -2D_{i,i}^* \\ -2D_{i,i} & (\sigma_i^{-1} + \sigma_{i+1}^{-1})S_{i,i} \end{bmatrix}, \qquad B_{i,j} = \begin{bmatrix} -\sigma_j N_{i,j} & D_{i,j}^* \\ D_{i,j} & -\sigma_j^{-1} S_{i,j} \end{bmatrix},$$
$$B_{j,i}^* = \begin{bmatrix} -\sigma_j N_{j,i} & D_{j,i}^* \\ D_{j,i} & -\sigma_j^{-1} S_{j,i} \end{bmatrix},$$

$$d_k = [b_k,\ c_k]^T, \quad (b_k)_i = \langle \partial_{\mathbf{n}} v_{\Omega_k} - \partial_{\mathbf{n}} v_{\Omega_{k+1}}, \phi_i^{(k)} \rangle, \quad (c_k)_i = \langle \sigma_{k+1}^{-1} v_{\Omega_{k+1}} - \sigma_k^{-1} v_{\Omega_k}, \psi_i^{(k)} \rangle,$$
$$z_k = [x_k,\ y_k]^T, \quad (x_k)_i = x_i^{(k)}, \quad (y_k)_i = y_i^{(k)},$$

and

$$(N_{k,l})_{(i,j)} = \langle \mathcal{N}_{k,l} \phi_j^{(l)}, \phi_i^{(k)} \rangle, \qquad (S_{kl})_{(i,j)} = \langle \mathcal{S}_{k,l} \psi_j^{(l)}, \psi_i^{(k)} \rangle,$$
$$(D_{k,l})_{(i,j)} = (D_{l,k}^*)_{(j,i)} = \langle \mathcal{D}_{k,l} \phi_j^{(l)}, \psi_i^{(k)} \rangle.$$

With $D_{k,l} = (D_{l,k}^*)^T$, we recognize $B_{i,j} = B_{j,i}^*$. Thus, the matrix T is now tridiagonal and symmetric. In order to set the matrix T up, both the integral operators and the scalar products (each corresponding to the calculation of a surface integral) have to be evaluated. The execution of $D_{k,l}$ and $S_{k,l}$ allows for an analytical solution for both kinds of basis functions [14, 77], while the integrals resulting from the scalar products have to be computed numerically [70, 45]. The $N_{k,l}$ can be calculated from the intermediate results of calculating $S_{k,l}$ by a formula given in [47]:

$$\langle \mathcal{N}_{k,l}\, {}^i\phi_r^{(l)}, {}^j\phi_s^{(k)} \rangle = -(q_r \times n_i)(q_s \times n_j) \langle \mathcal{S}_{k,l} \psi_i^{(l)}, \psi_j^{(k)} \rangle. \tag{2.64}$$

With an adequate choice of q_r and α_r, ${}^i\phi_r^{(l)}(x) = (q_r \cdot x + \alpha_r)\psi_i^{(l)}(x)$ corresponds to the restriction of $\phi_r^{(l)}$ to triangle T_i. One possible choice is $\alpha_r = 1 - \nabla\phi_r^{(l)} \cdot x_3(T_i)$ (with $x_3(T_i)$ being the position of node r, cf. Remark 8) and $q_r = \nabla\phi_r^{(l)}$. The same formula can, of course, be applied to ${}^j\phi_s^{(k)}$. Summing up the contributions from the triangles on which $\phi_r^{(l)}$ and $\phi_s^{(k)}$ are supported yields $(N_{k,l})_{(s,r)}$.

2.4.3 Deflation

The potential V is only determined up to a constant until now, since we did not exploit the condition $\int_\Omega v dx = 0$ or one of the possible alternatives given in relation with Theorem 1. Thus, T is singular and the matrix equation (2.63) admits no unique solution, yet. Imposing an additional

condition to remove this indetermination, and to gain an equation system with a unique solution is called *deflation* [18].
We will additionally claim

$$\int_{S_N} u^-_{S_N}(x) d\gamma(x) = \langle u^-_{S_N}, 1 \rangle = 0, \tag{2.65}$$

i.e., we establish a zero mean on the outermost surface. This condition is equivalent to $\sum_i x_i^{(N)} = 0$ in the discrete scenario (2.63). $y^{(N)}$, the result for $\partial_{\mathbf{n}} u^-_{S_N}$, automatically fulfills this assumption as a consequence of Stokes' theorem and the fact that u is a harmonic function.
To achieve our demand we follow the ideas of [18]. We substitute $N_{N,N}$ by $N_{N,N} + \omega \cdot ee^T$, $e^T = (1, 1, \ldots, 1)$ in the bottom right block of T, where we choose $\omega = (N_{N,N})_{(1,1)} / M_N$ with M_N being the number of unknowns, i.e., the number of vertices on the outermost surface. We can avoid a costly calculation for the optimal ω, since the choice of ω is not crucial [55]. For a regular mesh with elements of similar size and shape, the elements $(N_{N,N})_{(i,i)}$ are almost equal and therefore we can simply choose the first element as an approximation. The resulting matrix is regular and can be inverted. Therefore, the matrix is factorized using the Bunch-Kaufman diagonal pivoting method [2] and subsequently inverted.

2.4.4 Adaptive Integration

Especially for sources close to a surface, setting up the elements of the right hand side vector in (2.63), b_k and c_k, is crucial as the numerical evaluation of the scalar products may become inaccurate. To avoid this problem, an adaptive integration scheme is implemented in OpenMEEG [23]. During the integration, the triangles are subdivided until the required precision is achieved. We will shortly deal with the influence of the adaptive integration in Section 2.6.

2.5 Double-Layer BEM

The boundary integral equation underlying the double-layer approach was described in [22, 3]. However, it can easily be derived in the theoretical framework we already introduced by choosing the function $u_d = \sigma_i V - v_d$ in every Ω_i, $v_d = \sum_{i=1}^N v_{\Omega_i}$ and v_{Ω_i} as in Subsection 2.3.1, as starting point. Implying the boundary conditions of the forward problem (1.19) and the jump properties of a double-layer potential (see Section 2.2), leads to the double-layer representation [36]

$$\frac{2}{\sigma_j + \sigma_{j+1}} v_d = V|_{S_j} - \sum_{i=1}^{N} 2 \cdot \frac{\sigma_{i+1} - \sigma_i}{\sigma_j + \sigma_{j+1}} \mathcal{D}_{ji} V|_{S_i} \qquad \text{on each } S_j. \tag{2.66}$$

If we assume that all sources lie in the same compartment (usually Ω_1), we can rewrite $v_d = \sigma_1 V^\infty$, where V^∞ is the potential in an infinite homogeneous medium with the conductivity σ_1. In the case of a three- or four-layer head model, this is no restriction of generality.
(2.66) is discretized using collocation with linear interpolation (also called vertex method), applying the piecewise linear basis functions defined in (2.58) and Dirac functions $\delta_i^{(k)}$ that are defined in the vertices i [89]. After approximating V by $V_{S_l} = \sum_j x_j^{(l)} \phi_j^{(l)}$ on each surface and integrating against $\delta_i^{(k)}$ this yields

$$\underbrace{\begin{bmatrix} I_1 + A_{1,1} & A_{1,2} & \ldots & A_{1,N} \\ A_{2,1} & I_2 + A_{2,2} & \ddots & A_{2,N} \\ \vdots & \ddots & \ddots & \vdots \\ A_{N,1} & A_{N,2} & \ldots & I_N + A_{N,N} \end{bmatrix}}_{I+A} \cdot \underbrace{\begin{bmatrix} x_1 \\ x_2 \\ \vdots \\ x_N \end{bmatrix}}_{x} = \underbrace{\begin{bmatrix} b_1 \\ b_2 \\ \vdots \\ b_N \end{bmatrix}}_{b}, \tag{2.67}$$

where

$$(A_{k,l})_{(i,j)} = -2 \cdot \frac{\sigma_{l+1} - \sigma_l}{\sigma_k + \sigma_{k+1}} (D_{k,l})_{(i,j)} = -2 \cdot \frac{\sigma_{l+1} - \sigma_l}{\sigma_k + \sigma_{k+1}} \langle \mathcal{D}_{k,l} \phi_j^{(l)}, \delta_i^{(k)} \rangle,$$

$$(I_k)_{(i,j)} = \delta_{i,j}, \qquad (b_k)_i = \frac{2\sigma_1}{\sigma_k + \sigma_{k+1}} \langle V^\infty, \delta_i^{(k)} \rangle,$$

$$(x_k)_i = x_i^{(k)}.$$

We note that the scalar products with the delta distributions lead to an evaluation of the particular expression in singular points and special care is needed accordingly. We will not discuss this in detail here and only indicate that solutions to this problem exist [41].
The matrix equation could be solved directly by applying matrix inversion after a proper deflation. However, the low conductivity of the skull in relation to brain and skin leads to an ill condition of the matrix equation. To avoid arising numerical errors, the *isolated problem* or *isolated skull approach* (ISA) was proposed [31, 41]. We decompose the potential vector $x_k = \omega_k + \omega_k^{iso}$ with $\omega_2^{iso} = \ldots = \omega_N^{iso} = 0$ and ω_1^{iso} being the solution of the integral equation for the isolated brain compartment, i.e., we have to solve (2.66) with $N = 1$:

$$\omega_1^{iso} = H^{-1} b_1^{iso} \qquad \text{with } H \coloneqq I + 2D_{1,1},\ b_1^{iso} = \frac{\sigma_1 + \sigma_2}{\sigma_1} b_1. \tag{2.68}$$

The multi layer integral equation for the unknown ω can then be solved numerically more accurately [31, 89]. This results in the numerically stable formula for the computation of the potential vector x (in the three compartment case):

$$x = Cb \tag{2.69}$$

with

$$C \coloneqq \frac{\sigma_2}{\sigma_1} (I + A)^{-1} \begin{bmatrix} I & 0 & 0 \\ 0 & I & 0 \\ 0 & 0 & I - 2H^{-1} \end{bmatrix} + \frac{\sigma_1 + \sigma_2}{\sigma_1} \begin{bmatrix} 0 & 0 & 0 \\ 0 & 0 & 0 \\ 0 & 0 & H^{-1} \end{bmatrix}. \tag{2.70}$$

Again, this matrix is singular due to the fact that V is only known up to a constant and needs to be deflated. This is done similar to Subsection 2.4.3 by replacing H with $H + ee^T/M_N$ in both terms on the right hand side. The inversion of the matrix is executed on the basis of a LU-decomposition.

2.6 Experiments

We want to compare the results obtained with the symmetric BEM with the common double-layer approach. The variety of different implementations of the double-layer BEM is huge. Some examples are:

- *double-layer approach using linear collocation: BEMCP* [51], available from *FieldTrip*[1] and the default forward solver in *SPM*[2],
- *double-layer approach using linear collocation and ISA: Dipoli* [50], available from FieldTrip, *Helsinki BEM*[3] [66], *MNE*[4] [66, 31], *SimBio*[5] and *ASA*[6] [64, 90, 89],

[1] http://fieldtrip.fcdonders.nl
[2] http://www.fil.ion.ucl.ac.uk/spm/
[3] http://peili.hut.fi/BEM/
[4] http://www.nmr.mgh.harvard.edu/martinos/userInfo/data/MNE_register/
[5] https://www.mrt.uni-jena.de/simbio
[6] http://www.ant-neuro.com/products/asa

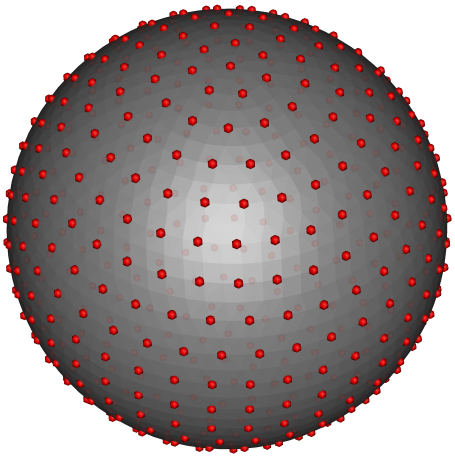

Figure 2.1: The 522 electrode sensor cap on the 2056 node surface mesh

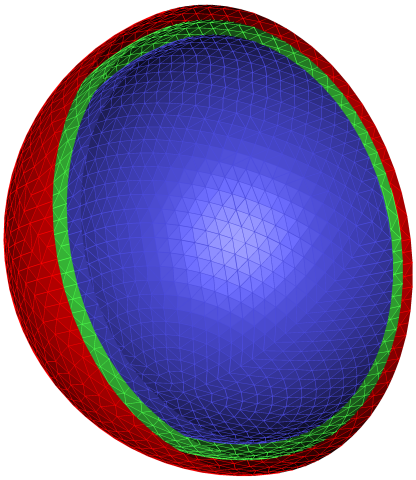

Figure 2.2: The three-layer sphere model used for the BE approaches

- *double-layer approach using linear collocation, ISA and virtual mesh refinement: CURRY*[7] [20].

It was shown that the double-layer approach can be improved by means of a Galerkin instead of a collocation approach [44]. Nevertheless, the collocation double-layer approach is applied by the large majority of users, and we choose to compare the results of the double-layer BE approach implemented in the SimBio-toolbox to those gained with the symmetric BEM implemented in the OpenMEEG-toolbox. We will use a three-layer sphere model where a quasi-analytical solution exists (see Section 1.6) and can be used as reference. The accuracy achieved by the SimBio implementation in former comparisons was equal or slightly better compared to other implementations of the double-layer approach [23].

2.6.1 Error Criteria

First we have to choose the discrete set of points in which we will evaluate the numerical solution, i.e., the outcome of our BE/FE method, and the analytical solution (see Section 1.6) in order to compute the numerical error. Due to the triangulation of the surfaces it would be conceivable to evaluate the error function in the vertices or mass centers of the triangles either only on surface S_N or on all surfaces $S_1, \ldots, S_n$ [36]. However, each choice would discriminate one of the implementations, since the collocation method benefits from an evaluation in the collocation points, i.e. the triangle vertices, while the galerkin method is less sensitive to the placement of evaluation points and would thus benefit when the mass-centers are chosen. We avoid this problem by choosing a more realistic way of comparison that does not take the geometry of the surface triangulation into account.
We created an artificial sensor cap by distributing $s = 522$ electrodes uniformly on the outermost surface S_N (see Figure 2.1) where we used the approximation of point-like electrodes (see [65] for other electrode models). The vector with the numerically calculated electrode potentials, V^{num}, is gained by applying a restriction matrix R to the potential at the surface nodes x_N. In the SimBio implementation it is simply searched for the mesh node closest to the sensor position and its potential is returned as result at the sensor node, resulting in only one non-zero entry per line in the restriction matrix R. The OpenMEEG implementation determines the triangle which contains the sensor position, and calculates its potential with trilinear interpolation out

[7] http://www.neuroscan.com

of the potential values at the triangle vertices so that up to three matrix entries per line may be non-zero. The two ways lead to slightly different results and thus influence the error of the two methods. However, for a growing number of mesh nodes on the outermost surface this error converges to zero and becomes negligible in our case.
V^{num} can now be compared to the analytical electrode potential V^{ana}. Three error criteria are commonly used to measure the accuracy of different solutions to the EEG forward problem:

$$RE(V^{num}, V^{ana}) := \frac{\|V^{num} - V^{ana}\|_2}{\|V^{ana}\|_2}, \tag{2.71}$$

$$RDM(V^{num}, V^{ana}) := \left\| \frac{V^{num}}{\|V^{num}\|_2} - \frac{V^{ana}}{\|V^{ana}\|_2} \right\|_2, \tag{2.72}$$

$$MAG(V^{num}, V^{ana}) := \frac{\|V^{num}\|_2}{\|V^{ana}\|_2} \tag{2.73}$$

with $\|u\|_2 = \sqrt{\sum_{i=1}^{s}(u_i)^2}$ being the discrete l_2 norm, s being the number of sensor nodes and u_i the $i-th$ entry of vector u. The *relative l_2-error* (RE) has the major drawback of not differentiating between magnitude and topographic errors. This lack of information is cleared by introducing the *relative difference measure* (RDM) and the *magnitude error* (MAG) [41]. Due to the normalization of the potential the RDM measures only topography errors. It is bounded above by 2. The magnitude error has an optimal value of 1 expressing how well the norm of the numerical solution fits those of the analytical solution. Because of the differing influence of topography and magnitude errors, we will mainly use the combination of RDM and MAG to interpret our results in the following. Additional figures concerning the RE are shown in the appendix (see Section A.2).

2.6.2 Evaluation Platform

We constructed an isotropic three compartment head model consisting of concentric spheres with radii 80 mm, 86 mm and 92 mm to evaluate the two BE approaches. We chose the commonly used conductivities of 0.33 S/m, 0.0042 S/m and 0.33 S/m for the three compartments (see Table A.1). The spheres were discretized using 2056 vertices per layer, leading to an overall vertex number of 6152 (see Figure 2.2). Meshes with the same cumulative number of vertices, but different numbers of vertices on the particular spheres, led to worse results (see Figure A.2). The majority of previous studies used only one set of dipoles placed on a ray from the center of the sphere to the outer [36, 89] with the drawback that the resulting error may highly depend on the mesh structure as it has a non-negligible effect whether the ray is pointing towards a triangle vertex or a triangle center. Hence, a conclusion with regard to the absolute accuracy is difficult. To avoid this, we generated a set of 125 randomly distributed unit vectors and placed dipoles in each direction in steps of 1 mm starting at a radius of 2 mm up to a radius of 77 mm. This corresponds to a maximal eccentricity, i.e., the quotient of source radius and radius of the innermost layer, of $96,25\%$ in the three layer case; in the (later examined) four layer case the most eccentric sources are only 1 mm below the cortex surface, leading to a maximal eccentricity of $98,72\%$. For each dipole position we computed results for both radial and tangential sources. The orientations of the tangential dipoles were, again, distributed randomly. The resulting orientations are shown in Figure 2.3. On this basis, we hope to deduce a more general result regarding the accuracy of the numerical solutions.
As indicated, we choose RDM and MAG as evidence. Two types of diagrams will be used. One will depict the *arithmetic mean* of the error for all dipoles with the same radius as a common lineplot, allowing no detailed analysis but giving a rough overview. The other applied type are so-called *boxplots*. The black dash marks the *median* of the errors at the particular radius, the box envelopes the *upper and lower quartile* and the errorbars show the minimal and maximal error. See, e.g., the left and right column of Figure 2.5 for a line- and a boxplot, respectively.

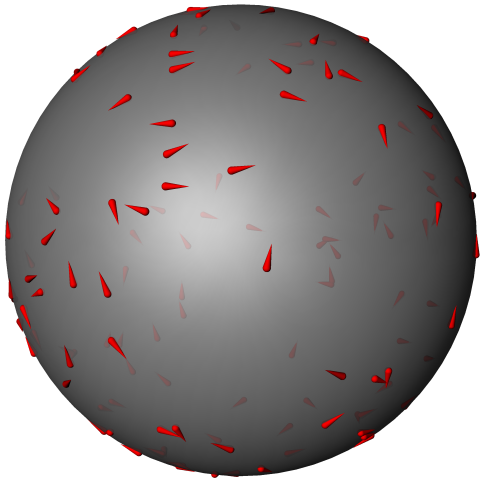

Figure 2.3: Distribution of the 125 dipoles and their tangential moments

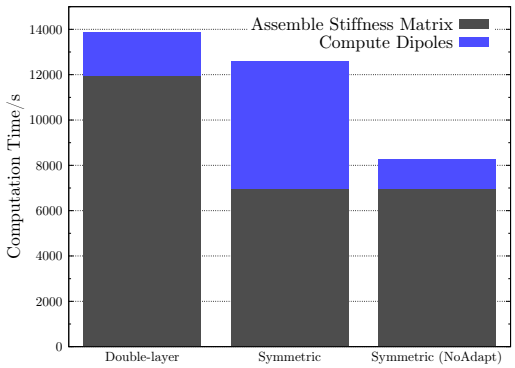

Figure 2.4: Computation times of the different BE approaches for 19,000 dipoles

Besides the numerical errors, we will observe the time effort of the different solution approaches, since a maintainable time consumption is an important criterion when considering the practical usage of realistic head models. A well-balanced comparison would need to oppose the accuracy of the different approaches while the overall computation time is kept constant or just the other way round. However, this is difficult to realize so that we will choose different references in our experiments, i.e., we simply use the same BE model to compare the BE approaches and we will keep the (unique) setup time constant when comparing BE and FE approaches. All measurements regarding computation time were carried out on a PC with an Intel Core2 Quad Processor at 2.83 GHz with 8 Gb of RAM and Ubuntu 9.10 installed. All computations were run in non-parallelized mode.

2.7 Results

As prearrangement, we evaluated the symmetric BE method implemented in OpenMEEG with and without the use of adaptive integration (see Subsection 2.4.4). The results of these computations are shown in Figure A.1. While the results for deep lying sources are more or less identical, showing good precision and low variance, the adaptive integration has, as to be expected, a huge effect for shallow sources, keeping the error and its variance small. Even though the errors without adaptive integration are small, too, we notice that the adaptive integration improves the stability of the method, avoiding the strong increase of the RDM for sources with large eccentricities. The difference with respect to the mean error is moderate, but the boxplots show some outliers with disproportional large errors when omitting the adaptive integration. The gain in precision has the cost of a higher computation time for the calculation of a single forward solution, since the numerical integration becomes more complex (see Table A.3, Figure 2.4). Nevertheless, we will use the adaptive integration in the following as its higher precision justifies the additional time effort.

In Figures 2.5 and A.5 the results of the symmetric BEM with adaptive integration implemented in OpenMEEG are opposed to those of the double-layer implementation in SimBio. We are able to confirm the results of [23], finding that the symmetric BEM clearly outperforms the double-layer BEM.

For very deep sources symmetric and double-layer BEM lead to similar results. Both implementations have a negligible RDM error, the double-layer BEM shows even less variance

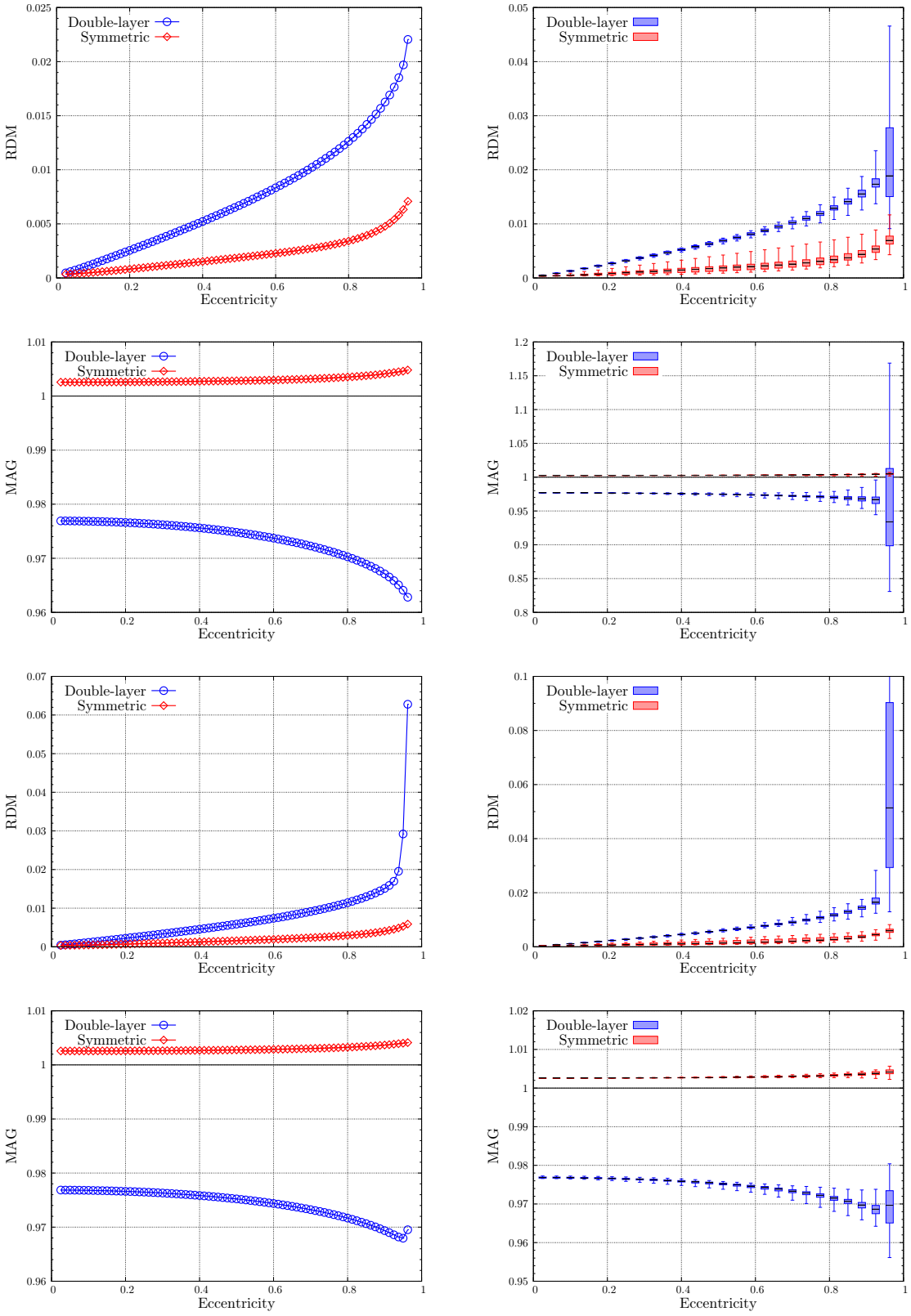

Figure 2.5: RDM and MAG versus eccentricity. The upper graphs are showing the results for radial dipoles, the lower graphs those for tangential dipoles. Note that the y-axes are scaled individually. Larger versions of the boxplots are shown in Figures A.3 and A.4. The maximal source eccentricity is 96.25%.

than the symmetric BEM. With growing eccentricity the graphs concerning the mean error show a clearly reduced increase of the RDM for the symmetric BEM compared to the common double-layer implementation. Even for the most eccentric radial sources, the RDM stays below 0.01 while the variance is in a range of approximately 0.005. In contrast, the double-layer method has a maximal RDM of 0.1 with a spread of nearly 0.09. For radial sources the differences are less drastic but the symmetric BEM still leads to clearly better results.
Comparing these results to Figure A.1 shows that the low RDM and its moderate increase with growing eccentricity is mainly a result of the symmetric formulation of the boundary integral equation (and not of the adaptive integration). The adaptive integration shows a major contribution at large eccentricities preventing outliers as possible effect of disadvantageous geometry. A notable result of the combination of adaptive integration and symmetric BEM is that the magnitude error for both dipole orientations is nearly erased; the MAG is bounded between 1.00 and 1.01 while it is mainly in a range of 0.95 to 0.98 for the double-layer approach. With the contribution of the low MAG the symmetric BEM has an about ten times lower mean RE compared to the double-layer approach (see Figure A.5).
When comparing the computation times of the three approaches we note that symmetric BEM with adaptive integration has an overall time effort for 19,000 forward computations comparable to those of the SimBio double-layer implementation. At the same time it is much more accurate. The setup of the BE head matrix that only has to be done once per head model, is the by far most time consuming part for the double-layer implementation, whereas setup and forward computations have an almost equal time consumption for the symmetric BEM. Thus, the computation time increases stronger with the number of dipoles than for the double-layer implementation. We find one origin for this in the higher computational demand of the Galerkin method with adaptive integration, in contrast to the relatively simple collocation approach, when setting up the right hand side vector. Consequently, the symmetric BEM without adaptive integration performs a single forward computation faster than the double-layer BEM, and still leads to better accuracies than the double-layer BEM. In [23] it was assumed that the long setup time is the result of a slower execution of algebraic routines in SimBio (possibly due to a less sophisticated implementation). Other implementations of the double-layer BEM with linear collocation are clearly faster than the symmetric BEM implementation of OpenMEEG. Nevertheless, the OpenMEEG symmetric BEM implementation is claimed to be the “fastest solver method for a prescribed accuracy”.

3 The Finite Element Method

In contrast to the boundary element method described in Chapter 2, where we reformulated the forward problem (1.19) as a boundary integral equation and thus only needed to discretize the surfaces of the brain compartments, finite element methods are applied directly to the "original" PDE (cf. Section 1).
FE methods have some advantages compared to BEM, e.g., the possibility to model anisotropic conductivities or to deal with arbitrary complex geometries. In our field of application this can be useful when modeling the CSF [4, 76, 56, 82], taking into account white matter anisotropy [71, 81, 33, 82, 29, 25], the three layeredness of the skull [59, 11, 12] or when facing anatomical anomalies in clinical applications, e.g., non-negligible skull holes due to surgery [49, 58]. The huge time consumption, which prevented the practical usage of FE methods for a long time, could be heavily reduced by the introduction of *transfer matrices* that allow for a direct mapping of the right hand side vector to the electrode potentials [83, 21]. Furthermore, the computational load of the BEM grows heavily when modeling more than the commonly used three compartments, especially when these have complex geometries like the cortex surface (which is needed to incorporate the cerebrospinal fluid). In contrast, this can be carried out at negligible costs with FE methods (see Section 3.6).
The main issue when realizing FE approaches to the EEG forward problem is the treatment of the singularity caused by the model assumption of a mathematical dipole. Three solution approaches are presented and evaluated in the next sections.
As a first step to apply FEM, the base domain is discretized into small regions; commonly tetrahedra or cubes are used, though higher order elements exist. Next, a set of basis functions is chosen, usually piecewise linear with support on only few elements, and the potential V is projected into the space of basis functions, yielding an approximation by a (finite) linear combination of basis functions. After treating the singularity caused by the point dipole and setting up the right hand side vector we gain a linear equation system that has to be solved to obtain the solution V.
We will apply different approaches to deal with the source singularity. For the subtraction approach a strategy similar to the BE methods is chosen by previously subtracting a homogeneous solution and calculating a correction potential to take the boundary conditions into account. We will further use direct approaches, which aim at approximating the singularity locally.
Independent of the particular element type, we will use piecewise linear basis functions ϕ_i throughout this section, having value 1 on node i, 0 on all other nodes and being piecewise linear in each element. In all three approaches the source will be modeled as a mathematical point dipole with moment p at position x_0 as defined in Section 1.4.

3.1 The Partial Integration Direct Potential Approach

One possibility to handle the source term is *partial integration* [39, 87, 24]. We multiply equation (1.10) by a basis function ϕ_i and integrate over the whole head domain Ω:

$$\int_\Omega \nabla(\sigma\nabla V)\cdot\phi_i dx = \int_\Omega f\cdot\phi_i dx = \int_\Omega \nabla J^p\cdot\phi_i dx. \tag{3.1}$$

Integration by parts applied to both sides of the equation yields

$$-\int_\Omega (\sigma\nabla V)\cdot\nabla\phi_i dx + \int_{\partial\Omega}\sigma\partial_{\mathbf{n}}V\cdot\phi_i d\gamma(x) = -\int_\Omega J^p\cdot\nabla\phi_i dx + \int_{\partial\Omega}\partial_{\mathbf{n}}J^p\cdot\phi_i d\gamma(x). \tag{3.2}$$

The partial integration on the right hand side has to be understood rather symbolically, since the strong singularity inherent to J^p does not allow the application in a strict sense.
We use the Neumann boundary condition from (1.10) and the fact that the current density vanishes at the head surface and obtain

$$\int_\Omega (\sigma \nabla V) \cdot \nabla \phi_i dx = \int_\Omega J^p \cdot \nabla \phi_i dx \overset{(1.13)}{=} p \nabla \phi_i(x_0) \cdot \mathbb{1}_i(x_0), \tag{3.3}$$

where $\mathbb{1}_i$ denotes the indicator function of element i. Approximating the potential V by its projection to the space of basis functions, $V = \sum_j x_j \phi_j$, yields

$$\sum_j x_j \cdot \int_\Omega \sigma \nabla \phi_j \cdot \nabla \phi_i dx = p \nabla \phi_i(x_0) \cdot \mathbb{1}_i(x_0). \tag{3.4}$$

We define the (symmetric) stiffness matrix K and the right hand side vector j^{part},

$$K_{ji} = \int_\Omega \sigma \nabla \phi_j \cdot \nabla \phi_i dx,$$
$$(j^{part})_i = \begin{cases} p \cdot \nabla \phi_i(x_0) \text{ if } i \in \{\text{Nodes of } element | x_0 \in element\}, \\ 0 \text{ otherwise.} \end{cases}$$

The linear equation system

$$Kx = j^{part} \tag{3.5}$$

with $x = (x_1, \ldots, x_N)^T$ has to be solved. This can be done directly using iterative solvers, e.g., *AMG-CG* or *IC(0)-CG* [83, 39, 86]. A fast method to calculate the results for many sources is presented in Section 3.4.
We note that the gradient of the linear ansatz functions, $\nabla \phi_i$, is constant inside an element for tetrahedral meshes and thus the right hand side vector, too. It is not distinguished between different source positions inside one particular element; this results in the same potential V for all dipoles inside the particular element. However, for cube meshes the gradient of the trilinear ansatz functions still depends on the position inside the cube. One can calculate that for dipoles pointing in one of the Cartesian directions, the right hand side vector is constant when moving the dipole position in the direction of its moment. We will keep this in mind when analyzing the error distribution inside a particular element in Section 3.7. With the use of higher order ansatz functions the spatial variability can be increased (also for tetrahedra).

3.2 The Venant Direct Approach

3.2.1 Dipole Modeling

The Venant approach transfers *St. Venant's principle*, originally established for elasticity theory, to electrostatics. The original conclusion is that complicated stress distributions can be simplified under certain conditions without notable influence in a relatively large distance. Accordingly, Venant's principle allows us to replace a point dipole by a distribution of electrical monopoles with very local extent and specific strength if the original dipole moment is conserved. Then, the influence of the approximation on the electric field in a relatively far distance, e.g., at the EEG electrodes, is negligible (see Appendix A.3.1). The theory for the approach implemented in the SimBio-toolbox was described in [7, 62, 80] and we will follow these ideas.
We want to represent our point dipole by a set of electrical monopoles and make use of the relation $p = \int (x - x_0)\rho(x)dx$ for the dipole moment [35]. We decide to place monopole sources of strength q_i only on the $k-1$ neighboring FE nodes $x_2, x_3, \ldots, x_k$ of the FE node x_1 which is closest to the dipole position x_0 (but not on FE node x_1 itself), i.e., we load the nodes sharing a

vertex with x_1. The distance between x_0 and x_1 can become arbitrarily small inducing a very high load q at this position, which might lead to numerical instabilities, disposing us to place no monopole at this position. The number of neighboring nodes is 27 for cubic meshes and usually about 30 for tetrahedral meshes [7]. We approximate the source distribution by a monopole distribution $\rho = \sum_{i=2}^{k} q_i \delta_{x_i}$ whose first moment, denoted ${}^1T$, reads

$$ {}^1T = p = \sum_{i=2}^{k} (x_i - x_0) q_i = \sum_{i=2}^{k} \Delta x_i q_i. \tag{3.6} $$

After scaling with a suitable reference length a^{ref}, chosen larger then twice the element edge length so that $\Delta x / a^{ref} < 1 \; \forall i = 2, \dots k$ (see Appendix A.3.2), we formulate (3.6) for general moments ${}^l\bar{T}$, $l \leq 0$,

$$ ({}^l\bar{T})_j = \sum_{i=2}^{k} (\Delta \bar{x}_i)_j^l \, q_i, \qquad j = 1, 2, 3, \tag{3.7} $$

with a bar indicating scaled variables. The use of higher order moments ${}^l\bar{T}$ is suggested in [57]. We indicate that these moments should not be confused with the higher moments of the common multipole expansion. For $l = 0$, (3.7) is the sum of charges $\sum_{i=2}^{k} q_i$, which must be zero since the resulting far-field may not contain any monopole contributions. With the zeroth, all other odd moments vanish, too. This implies

$$ \underbrace{\begin{bmatrix} ({}^0\bar{T})_j \\ ({}^1\bar{T})_j \\ \vdots \\ ({}^n\bar{T})_j \end{bmatrix}}_{\bar{t}_j} = \underbrace{\begin{bmatrix} (\Delta\bar{x}_1)_j^0 & (\Delta\bar{x}_2)_j^0 & \dots & (\Delta\bar{x}_k)_j^0 \\ (\Delta\bar{x}_1)_j^1 & (\Delta\bar{x}_2)_j^1 & \dots & (\Delta\bar{x}_k)_j^1 \\ \vdots & \vdots & \ddots & \vdots \\ (\Delta\bar{x}_1)_j^n & (\Delta\bar{x}_2)_j^n & \dots & (\Delta\bar{x}_k)_j^n \end{bmatrix}}_{\bar{X}_j} \cdot \underbrace{\begin{bmatrix} q_1 \\ q_2 \\ \vdots \\ q_n \end{bmatrix}}_{q}. \tag{3.8} $$

We can compute the ${}^l\bar{T}$ up to $l = 2$ for the given dipole moment p:

$$ {}^l\bar{T} = \frac{1 - (-1)^l}{\left(2a^{ref}\right)^l} \cdot p. \tag{3.9} $$

In the case of a point dipole all higher orders admit the limit zero, too. Further, we define the matrix $\bar{W}_j$ by $(\bar{W}_j)_{(m,s)} = (\Delta\bar{x}_m)^r \, \delta_{m,s}$ for $r = 0$ or $r = 1$. Then, the vector q is the result of minimizing the functional

$$ F_\lambda(q) = \|\bar{t}_j - \bar{X}_j q\|_2^2 + \lambda \|\bar{W}_j q\|_2^2 \tag{3.10} $$

with $\bar{X}_j$ and $\bar{t}_j$ defined as in (3.8). The first term measures the difference between the original dipole moment and our approximation, while the second term penalizes loads of large absolute value $|q_i|$ in a least square sense and ensures the uniqueness of the solution of minimizing F_λ. Thereby, we avoid sources with large value that do not contribute to the far-field, so-called *blind sources*. Differentiation with respect to the q_i yields the solution of the minimization problem:

$$ \left(\bar{X}_j^T \bar{X}_j + \lambda \bar{W}_j^T \bar{W}_j\right) q = \bar{X}_j^T \bar{t}_j, \tag{3.11} $$

and as result for the vector q,

$$ q = \left[\sum_{j=1}^{3} \left(\bar{X}_j^T \bar{X}_j + \lambda \bar{W}_j^T \bar{W}_j\right)\right]^{-1} \cdot \sum_{j=1}^{3} \bar{X}_j^T \bar{t}_j. \tag{3.12} $$

The approximation order n is commonly not chosen larger than two. Order two results in a spatial concentration of loads in the dipole axis compared to order one. The choice $r = 1$ effects a spatial concentration of loads around the dipole node for large products $\Delta\bar{x}_i q_i$ being penalized. The parameter λ should be chosen as small as possible in order to approximate the desired moments accurately, but large enough to avoid indetermination of the equation system.
We fix $a^{ref} = 20$ mm, $n = 2$, $r = 1$ and $\lambda = 10^{-6}$ for our computations.

3.2.2 Derivation of the Matrix Equation

We will only give a short heuristic derivation of the discretization here, more detailed ones are found in the literature [7, 78]. The first Maxwell equation (1.1) stating that the divergence of an electric field exposes sources and sinks of yonder allows us to replace the divergence of the primary current J^p by the current sources. These current sources correspond to our previously computed monopoles q_i. Accordingly, we approximate the source term $f = \nabla J^p$ generated by our primary current J^p through

$$\nabla \cdot J^p = \sum_{l=2}^{k} q_l \delta_{x_l}. \tag{3.13}$$

We insert this into (3.1), applicate partial integration on the left hand side and replace V by its projection to obtain

$$\sum_j x_j \cdot \int_\Omega \sigma \nabla \phi_j \cdot \nabla \phi_i dx = \int_\Omega \nabla \cdot J^p \cdot \phi_i dx = \sum_{l=2}^{k} \int_\Omega q_l \delta_{x_l} \cdot \phi_i dx = \sum_{l=2}^{k} q_l \delta_{il} \tag{3.14}$$

where we use the fact that ϕ_i is 1 on node i and vanishes on all other nodes. This yields the equation system

$$Kx = j^{ven} \tag{3.15}$$

with the same stiffness matrix K as in Section 3.1 and the right hand side vector j^{ven} defined as

$$(j^{ven})_i = \begin{cases} q_l \text{ if } i = node(l), \\ 0 \text{ otherwise.} \end{cases} \tag{3.16}$$

3.3 The Subtraction Approach

When assuming that there exists a non-empty open neighborhood Ω^∞ of the source with constant isotropic conductivity σ^∞, we can erase the singularity in a manner similar to Section 2.5 [6, 85, 17]. The case of an anisotropic conductivity is possible, too, but will not be treated here. We split up the potential V and the conductivity σ into two parts:

$$V = V^\infty + V^{cor}, \tag{3.17}$$

$$\sigma = \sigma^\infty + \sigma^{cor}. \tag{3.18}$$

The potential V^∞ in an unbounded, homogeneous conductor can be calculated analytically, applying (1.17): $\sigma^\infty V^\infty = -(\nabla \cdot J^p) * G$. Inserting the decomposition of V into (1.10) and subtracting the homogeneous solution, results in a Poisson equation for the correction potential:

$$-\nabla \cdot (\sigma \nabla V^{cor}) = f \quad \text{in } \Omega, \qquad f := \nabla \cdot (\sigma^{cor} \nabla V^\infty), \tag{3.19}$$

$$\sigma \partial_{\mathbf{n}} V^{cor} = g \quad \text{on } \Gamma, \qquad g := -\sigma \partial_{\mathbf{n}} V^\infty. \tag{3.20}$$

Multiplication with a basis function ϕ_i and partial integration gives us

$$\int_\Omega \sigma \nabla V^{cor} \cdot \nabla \phi_i dx = \\ - \int_\Omega \sigma^{cor} \nabla V^\infty \cdot \nabla \phi_i dx - \int_{\partial\Omega} \sigma^\infty \partial_{\mathbf{n}} V^\infty \cdot \phi_i d\gamma(x) + \int_{\partial\Omega} \sigma \partial_{\mathbf{n}} (V^{cor} + V^\infty) \cdot \phi_i d\gamma(x), \tag{3.21}$$

where we already reorganized terms and exploited (3.18). The third term vanishes as a consequence of the Neumann boundary condition. Approximating V^{cor} by a linear combination of our basis functions, $V^{cor} = \sum_j x_j \phi_j$, results in the equation system

$$Kx^{cor} = j^{cor}, \tag{3.22}$$

where K is defined as above and j^{cor} is given by

$$(j^{cor})_i = -\int_\Omega \sigma^{cor} \nabla V^\infty \cdot \nabla \phi_i dx - \int_{\partial\Omega} \sigma^\infty \partial_{\mathbf{n}} V^\infty \cdot \phi_i d\gamma(x), \tag{3.23}$$

and needs to be calculated numerically [17]. Finally, the potential V is gained by adding up V^{cor} and V^∞.
The subtraction approach is theoretically well understood, existence and uniqueness of a solution and convergence of the solution can be shown [85, 17]. As the right hand side vector j^{cor} has many non-zero entries, the computational demands are higher than those of the Venant or the partial integration approach.

3.4 Transfer Matrices

The equation systems resulting from the FEM, (3.5), (3.15) and (3.22), are of similar shape with the same symmetric stiffness matrix K:

$$Kx = j. \tag{3.24}$$

For n FE nodes the vector x has as many entries resulting in up to 3 million unknowns (for a 1 mm cubic headgrid). It is common standard to use precomputed *leadfield matrices* to solve the inverse problem, relating the activity of dipoles at a chosen set of positions, the so-called *influence nodes*, to the resulting potential at the EEG sensors. It is necessary to compute a forward solution for potentially many thousand dipoles, and thus, to solve the above large equation system just as often. The computation time for many dipoles can be drastically reduced by exploiting the associativity of the matrix multiplication [83]. The basic idea is that it is not necessary to compute the potential V for every node as we are only interested in the resulting potential at the sensor nodes. To imply this, we introduce a restriction matrix R, which maps the potential V to the particular potentials of the measurement sensors (stored in the vector V^{eeg}). We assign each sensor the potential of the FE node that is next to its position. Thus, with s electrodes, we have a $(s-1) \times n$ restriction matrix R (when assuming that the potential at the reference electrode is fixed to zero). This yields

$$V^{eeg} = R \cdot x, \tag{3.25}$$

where x is the solution vector of the FE method, thus containing the potentials of the FE nodes. The matrix R has only one non-zero entry per line; $R_{(i,j)} = 1$ means that FE node j corresponds to electrode $i+1$ if the reference electrode is defined as first electrode. Next, we define the transfer matrix T,

$$T = R \cdot K^{-1}, \tag{3.26}$$

that gives us a direct mapping of a right hand side vector j to the unknown electrode potentials,

$$Tj = (RK^{-1})j = R(K^{-1}j) = RV = V^{eeg}. \tag{3.27}$$

Thereby, the calculation of the electrode potentials V^{eeg} reduces to the multiplication of a fully populated matrix with a sparse vector for the Venant and the partial integration approach and with a fully populated vector for the subtraction approach. Furthermore, the homogeneous medium solution V^∞ needs to be calculated and summed up here, indicating that the speed-up will not be as large as for the direct approaches.
Even though the inverse of the stiffness matrix K^{-1} exists, its calculation is not feasible, since the sparseness of K will be lost while inverting. Instead, we express the transfer matrix T by a matrix equation so that the computation of T reduces to numerically solving $(s-1)$ equation systems. Multiplying equation (3.26) with matrix K from the right side and transposing gives us

$$KT^T = R^T, \tag{3.28}$$

where we exploited the symmetry of K. T can now be computed line by line solving (3.28) for the column vectors of R^T. As the resulting equation systems are large but sparse we use, again, iterative methods for their solution.

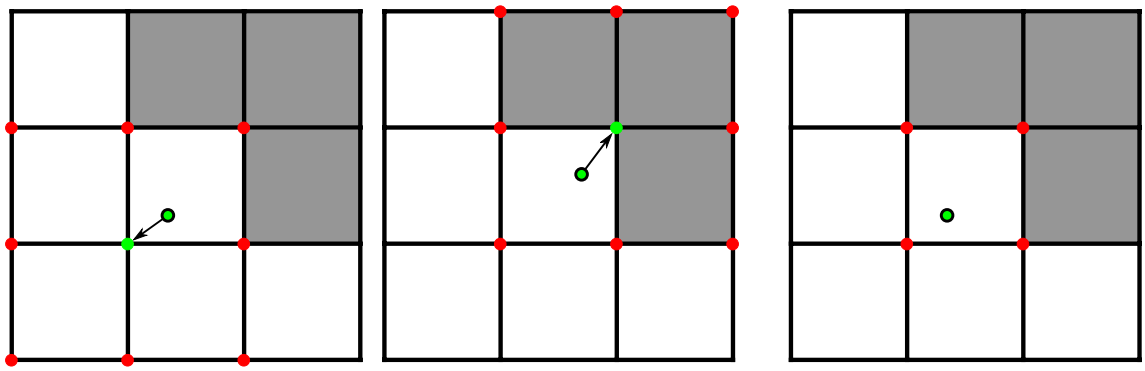

(a) Venant **(b)** Partial integration

Figure 3.1: Distribution of loaded nodes. Red dots mark loaded nodes, the green filled dot the dipole position and the green dot the FE node x_1 next to the dipole position.

3.5 Distribution of Loaded Nodes for Shallow Sources

For the direct approaches, Venant and partial integration, the right hand side vector j is sparse. Only few FE nodes are loaded, i.e., have non-zero entries. When sources are very close to compartment boundaries, loaded nodes may lie directly on compartment boundaries or even in the wrong compartment. This may affect the numerical accuracy heavily, especially when the outer compartment has a significantly higher conductivity. For instance, we will assume a conductivity of 1.79 S/m for the CSF in relation to 0.33 S/m for the brain. To demonstrate this issue, an artificial scenario in a regular cube model is depicted in Figure 3.1, where the distribution of loaded nodes for sources lying in cubes that are adjacent to a conductivity jump is shown.
The actual influence cannot be estimated in advance. Nevertheless, we expect the partial integration approach to be very sensitive to loaded nodes that are placed on compartment boundaries. Since only eight entries in the right hand side vector are non-zero, few deficient nodes may already have huge influence to the accuracy. Thus, we expect a raise of the numerical error, as soon as dipoles are placed in the outermost layer of cubes. In contrast, the Venant approach has 27 loaded nodes, permitting less influence of single nodes. As long as the node closest to the source position, x_1, is no surface node itself, we expect only moderate inaccuracies. However, when x_1 lies on a compartment boundary, the inaccuracies should be huge. We will validate our assumptions in the next Section 3.7.

3.6 Experiments

We will compare the three previously derived FE approaches in three and four layer tetrahedral sphere models and a four layer hexahedral sphere model in the following. We will use the results gained in the three layer tetrahedral model to compare them with the results of the symmetric BEM. Therefore, we will use the same dipole configuration and electrode cap as in Section 2.6. Again, most previous studies using FE methods only used dipoles placed on only one or two rays [84, 39, 17], whereas the influence of the local mesh geometry is expected to be even larger than in the BEM case.

Besides other reasons the use of the three layer tetrahedral mesh when confronting BE and FE approaches serves clarity, since the process of creating a three layer tetrahedral head mesh in practice has requirements comparable to those of BE model generation. Both times triangulated surfaces of skin, outer skull and inner skull that need to be extracted out of, e.g., MR images, and have to be closed and non-intersecting are basic. The gained surface meshes could then be directly applied with BE methods, while for an application of FEM the whole volume has to be tetrahedralized furthermore (see Subsection 3.6.2). The four layer tetrahedral model embeds an additional surface representing the cortex surface. This has the consequence of a significantly increased number of nodes and, thus, computation time in a BE model, while it is uncritical in the FEM case. The extra surface can be easily embedded in the mesh generation without demanding notably more nodes in the final mesh.
In contrast to these approaches, hexahedral FE meshes have the huge advantage that they can be obtained directly from labeled MR images without further preliminaries. The surface generation can be dropped by exploiting the coincidence between mesh elements and voxels. Thus, the creation of hexahedral meshes needs less preliminary worksteps.
Since periodic oscillations have appeared when using the Venant and the partial integration approach with hexahedral meshes [84, 38], we will study the distribution of the RE inside an element more detailed than possible with usual diagrams (see Subsection 3.6.4). This is examined as a preparation of Chapter 4.

3.6.1 Finite Element Model Generation

The three layer models have the same parametrization as the BE models (see Table A.1); the additional CSF compartment in the four layer models has an inner radius of 78 mm and a conductivity of 1.79 S/m (see Table A.2). Thus, the maximal source eccentricity is at 98.72 %.

3.6.2 Tetrahedra Model

In order to justify a comparison of the results of the FE approaches to those we achieved in the previous chapter, the computational demand should not differ too much. We chose to adjust the number of elements of the tetrahedral FE meshes so that the time consumption for the setup of the transfer matrix and of the BE head matrix, which has to be carried out once per head model, are expected to be roughly the same. The resolution of the grid for the subtraction approach was chosen with the goal to have a similar accuracy for the three FE approaches. Due to the high computational complexity of the subtraction approach the computation time for our set of dipoles is expected to be much higher in this case.
We made use of the software Tetgen[1] which implements a *Constrained Delaunay Tetrahedralization* (CDT) [63]. Our starting point were surface meshes of the compartment boundaries, similar to those in Subsection 2.6.2 but with a higher resolution of some ten thousand nodes per surface. In practical usage this allows an adequate fitting to the head anatomy. On this basis a tetrahedralization of the whole volume conductor conforming to the surface meshes was generated.
Two different constraints were imposed to achieve a good mesh quality. The first constraint, called *quality constraint*, influences the shape of the tetrahedra. By fixing an upper bound for the ratio between the radius of the tetrahedras circumsphere and the length of its shortest edge, most types of unwanted tetrahedra shapes can be excluded - apart from very flat tetrahedra. Those can be avoided by the *volume constraint*, being an upper bound for the volume of a particular tetrahedra. The volume constraint can be chosen independently for each compartment.
Different choices of the volume constraint for specific compartments - leading to variable mesh densities - and their influence on the accuracy of the solution have been examined [58, 39]. While a homogeneous distribution of nodes over the whole volume is optimal for the Venant and

[1] http://tetgen.berlios.de/

the partial integration approach, the subtraction approach performs best when modeling the surfaces with a high resolution, implying no volume constraint in the innermost compartment (which contains the source) and a very small volume constraint in the other compartments. This creates a dense mesh at the compartment boundaries and the numerical accuracy and stability is increased.
Following these results and our previous considerations we constructed two tailored FE meshes; the chosen parameters and the resulting meshes are shown in Table A.4 and Figure A.6.

3.6.3 Hexahedra Model

In order to build up regular hexahedra meshes we generated an artificial MR image of a four layered sphere (see Figure 3.2) having an isotropic resolution of $256 \times 256 \times 256$ voxels, each voxel containing a volume of 1 mm^3. Exploiting the cubic voxel structure, we generated hexahedra meshes using the software *Vgrid*[2], which is an outcome of the SimBio project [32, 5]. We chose an edge length of 1 mm so that each voxel forms one element. The elements are labeled according to the corresponding voxels label.

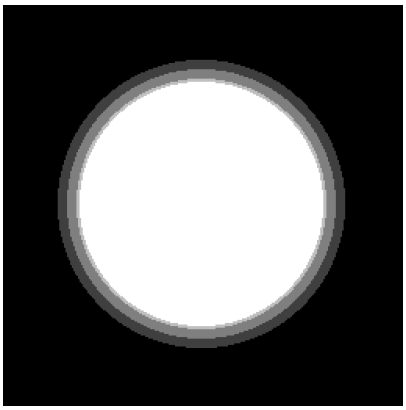

Figure 3.2: The artificial MR image of a sphere used for the generation of the cubic models. Cut is made through the $x = 127$ plane.

We further created a geometry-adapted hexahedral mesh. Regular hexahedra meshes do not respect the geometry very well, e.g., so-called staircase effects may appear. To avoid these effects we applied a *node shift* algorithm, allowing smoother and more accurate boundaries [8]. A two-dimensional example of the node shift algorithm is illustrated in Figure 3.3. For a node on a compartment interface the materials of the eight elements sharing the node are determined. If a material is represented by three or less of the surrounding elements, the centroid (x, y, z) of the elements being assigned to this minority material is calculated in a coordinate system relative to the node. We chose a *shift constraint* of 0.49, thus the particular node is shifted by the vector

$$(\Delta x, \Delta y, \Delta z)^T = (0.49 \cdot x, 0.49 \cdot y, 0.49 \cdot z)^T. \tag{3.29}$$

Previous studies have shown that both the topography and magnitude error can be reduced by a factor greater than 2 for tangential and greater than 1.5 for radial sources [80]. Hence, we will use the geometry-adapted mesh if possible, i.e., if implemented. Since the use of node shift meshes is not yet implemented for the subtraction approach, we will use ordinary cube meshes there.
In Figure A.7 the created meshes are visualized, their parametrization is given in Table A.5.

[2] http://www.rheinahrcampus.de/∼medsim/vgrid/

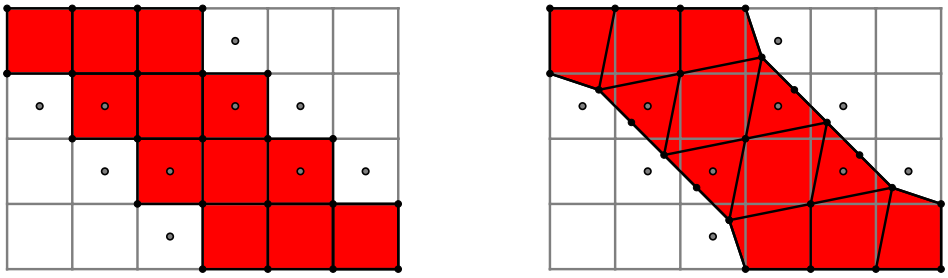

Figure 3.3: Node shift in two dimensions. On the left the staircase like boundary before the node shift, on the right the smoothed boundary afterwards. The filled dots mark the centroids of the elements belonging to the minority material.

3.6.4 Error Maps

In order to be able to visualize the already mentioned oscillations of the Venant and the partial integration approach, we will create *error maps*. We distribute dipoles on a fine grid (width $d = 0.05$ mm) on the surface of a small cubic domain having its bottom left corner at $(155, 155, 155)^T$ (the center of the sphere is at $(127, 127, 127)^T$) and an edge length of 4 mm. At each dipole position we calculate forward solutions in the three Cartesian directions and visualize the relative error (RE) for each direction and the mean over the RE in the different directions. Thereby, we hope to gain insight into the influence of the local mesh structure on the numerical accuracy.
Due to the theoretical derivation, we expect minimal errors for the Venant approach when dipoles are placed directly on FE nodes. This was experimentally verified and visualized for tetrahedral models in [37]. In contrast, we assume the best results for sources placed in the center of an element with the partial integration approach. Our estimation is that the constancy of the solution inside the element leads to higher errors for source positions apart the element center.

3.7 Results

3.7.1 Tetrahedral Models

We will first examine the results attained with tetrahedral three layer models. As intended, the setup time of the FE approaches differs hardly from those of the symmetric BE approach (see Table A.6 and Figure 3.4). This gives us a reference point regarding the validity of our comparison between BE and FE approaches. Nevertheless, a single forward computation is much faster for the Venant and the partial integration approach than for the symmetric BEM. This is not surprising, as it consists in the simple setup of the right hand side vector, which has only few non-zero entries and can be calculated easily, and a following multiplication of a matrix and a sparse vector, while the BE right hand side is dense and numerical integration is necessary for its setup. Thus, the overall computation time for the direct FE approaches is clearly the shortest. The subtraction approach has the by far highest time consumption. It benefits less from the transfer matrix approach than the Venant or the partial integration approach, since the setup of the right hand side is more complex in this case, requiring both a numerical volume and surface integration. Furthermore, the singularity potential V^{∞} has to be calculated analytically in addition to the numerical solution of V^{cor}. We intend to reduce the computation time drastically by the use of leadfield interpolation (see Chapter 4).
The MAG and RDM of the FE approaches are shown in Figure 3.5. Regarding the mean RDM, the Venant approach performs best, the subtraction has a slightly larger error and the partial integration approach has the largest mean error. All approaches show a tendency to have higher errors for superficial sources. The MAG error is negligible for all approaches being bounded

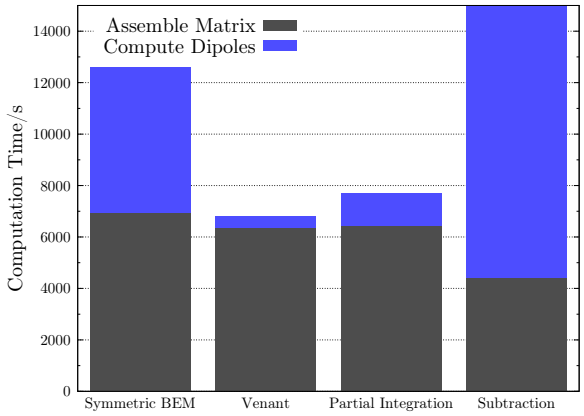

Figure 3.4: Computation times for the different FE approaches and the symmetric BEM. The computation time of the subtraction approach exceeds the y-range (the computation time is 2579 min 18 s, cf. Table A.6).

between 0.995 and 1.01. A close look at the boxplots shows that the unsteady behavior of the errors for the Venant and the partial integration observed in earlier studies results in a wide gap between minimal and maximal error so that the boxes are widespread in y-direction. Especially for the partial integration approach the RDM shows a relatively large difference between minimal and maximal error of up to 0.04 at a particular radius, having some outliers with a RDM up to four times higher for radial sources and nearly three times higher for tangential sources than the other approaches. The errors of the Venant solution vary less with a maximal gap of 0.02 regarding the RDM. The maximal error is the lowest of the three approaches. The variance appears to be nearly independent of the source eccentricity in both cases. Due to the analytical treatment of the source singularity the subtraction approach does not show oscillatory behavior, represented through a very smooth curve for the mean error with the errors at a particular radius lying within a small band in the boxplot. Even though the variance grows for superficial sources it is still beneath those of the other approaches. Apart from some outliers, none of the FE approaches shows a remarkable sensitivity regarding the dipole orientation in the tetrahedral model.

The symmetric BEM outperforms the three FE approaches, providing the clearly most accurate solution in the three layer sphere model. While its MAG error is slightly higher, but still negligible, the RDM is halved for eccentric sources. Reminding Figure 2.5, we notice that especially the small variance of the error exposes the symmetric BEM. At the same time, the common double-layer BEM performs worse than the FE methods particularly for eccentric sources. When examining the approaches at a fixed overall computation time instead of a fixed setup time, the direct FE approaches would probably achieve slightly better results, since meshes could be further refined. However, these numerical differences are negligible when obeying the error aroused by neglecting the distinction between different brain compartments, e.g., between CSF and grey and white matter as we will see in the following.

Turning towards the four layer tetrahedral sphere model, we mainly see the results of the three layer case approved (see Figure 3.6). The errors of the Venant and the subtraction approach grow a little while we note that the result for the partial integration approach has slightly improved even though the outermost sources at a radius of 77 mm lie only 1 mm below the CSF compartment now. This is most likely an accidental effect of advantageous mesh geometries. Besides, our considerations in Section 3.5 are demonstrated for the Venant approach at the outermost sources, even though we have a tetrahedral model here. We find a huge magnitude error especially for radial sources, while the RDM is more affected for tangential sources. In contrast, the subtraction approach shows topographic inaccuracies for radial moments at the

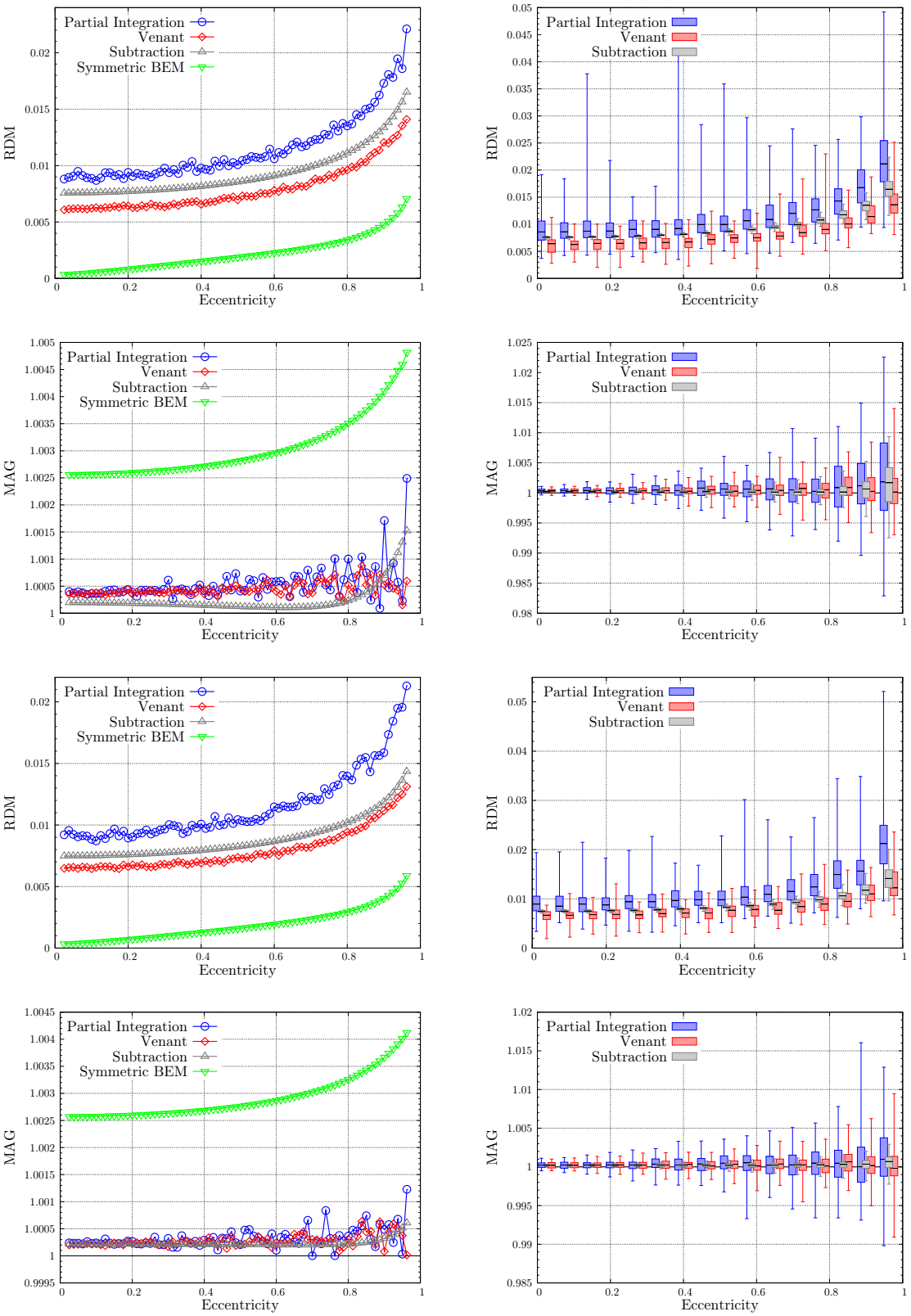

Figure 3.5: RDM and MAG versus eccentricity using the tetrahedral three layer FE models. The upper graphs showing the results for radial dipoles, the lower graphs those for tangential dipoles. Note that the y-axes are scaled individually. For a better readability the boxes for the Venant and the partial integration are shifted slightly into positive and negative x-direction, respectively. Larger versions of the boxplots are shown in Figures A.8 and A.9. The maximal source eccentricity is 98.72%.

most eccentric source position, performing worst of all approaches here, while the error of the partial integration approach even reduces here, not showing the assumed inaccuracies.
To clarify the importance of modeling the CSF compartment, we introduced an additional error curve named *effect* showing the pure analytical error of neglecting the CSF, i.e., we calculated RDM and MAG of the three layer analytical solution in reference to the four layer analytical solution. For both RDM and MAG the model error exceeds the errors of the three numerical approaches by far. This has special importance when deciding whether to use a BE or a FE method since embedding the cortex surface into BE models is not feasible with the current BE implementations (and the processing power of today's pcs) as we already explained.

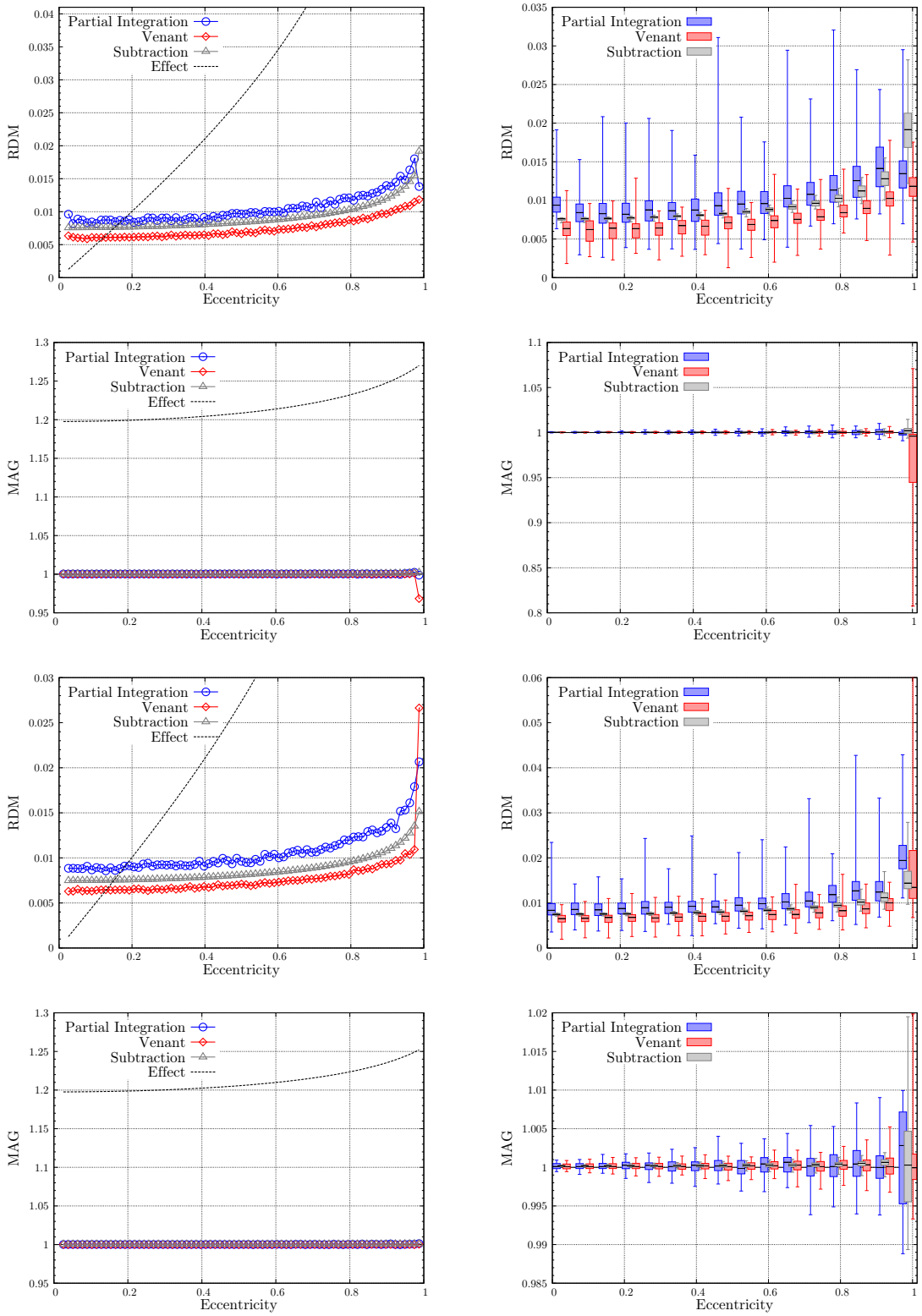

Figure 3.6: RDM and MAG versus eccentricity using the tetrahedral four layer FE models. The upper graphs show the results for radial dipoles, the lower graphs those for tangential dipoles. The curve marked *effect* shows the analytical error caused by neglecting the CSF compartment. Note that the y-axes are scaled individually. For a better readability the boxes for the Venant and the partial integration are shifted slightly into positive and negative x-direction, respectively. Larger versions of the boxplots are shown in Figures A.11 and A.12. The maximal source eccentricity is 98.72%.

3.7.2 Hexahedral Models

Since the current implementation of the subtraction approach is unable to deal with node shifting, we ran comparisons in a regular four layer cube model, first (see Figure 3.7). For deep sources all approaches lead to similar results. The amplitude of the oscillation is comparable to those observed with the tetrahedral models for the Venant and the partial integration approach, resulting in a comparable spread in the boxplots. All approaches have a RDM below 0.03 up to an eccentricity of over 0.92. For more superficial sources the results for radial dipoles become more inaccurate with the partial integration approach performing worst. It shows the outliers with the highest error while the accuracy is constantly good up to an eccentricity of 0.96 for tangential sources. At the most eccentric set of sources the errors grow rapidly with, again, the partial integration approach performing worst and the Venant approach providing the best result, admittedly with maximal errors above 0.1.
We suppose the unfavorable influence of the effects discussed in Section 3.5 occurring here for the direct approaches, again. The Venant approach is less affected than the partial integration approach since our sources have a maximal distance of 77 mm to the sphere center, and thus the dipole position should not be closest to a surface node, but might already be inside of a surface element. Low errors at the highest eccentricity are probably the results of advantageous geometry constellations. The subtraction approach is probably discriminated by the constant mesh density, leading to inaccuracies for superficial sources.
The use of geometry-adapted hexahedra can clearly improve the numerical accuracy for the Venant and the partial integration approach (see Figure 3.8), confirming the results of previous studies [80]. Especially the MAG is improved, the mean is reduced by 0.03 to below 1.02. The results comply with our expectations apart from the appearance of some outliers that lead to worse results with the introduction of the geometry-adapted mesh. However, the major problem of huge inaccuracies for very eccentric sources is still present. If we neglect the rapid growth of errors for the highest eccentricities, the gained accuracies are comparable to those computed with the tetrahedral model. The partial integration approach yields slightly improved results, while those of the Venant approach are in an identical range.
We illustrated the mean RE, RDM and MAG (i.e., the Cartesian mean of the errors for dipole moments oriented in the three coordinate directions) of the two direct approaches for highly eccentric sources in the upper row of Figures A.27 and A.28. We find our previous considerations approved with the partial integration approach, observing a sudden growth of errors when dipoles are placed in the last layer of cubes. The results of the Venant approach are less clear. The MAG shows the expected behavior of a sudden decrease of accuracy when the dipole position becomes adjacent to boundary nodes, while RE and RDM show some irregularities. This might be an admission to the simplifications in our setting, i.e., only observing mean errors and neglecting the three dimensional grid structure. Nevertheless, we aim to eliminate these problems applying leadfield extrapolation combined with cropped grids.

3.7.3 Investigation of Error Oscillations

We show error maps for the Venant and the partial integration approach in Figures A.20 and A.21, respectively. As intended, the oscillations of the accuracy can be observed nicely.
The solution attained with the Venant approach oscillates strongly with a period of 1 mm, i.e., one edge length, in the two Cartesian directions when moving the source in the plane that is perpendicular to the dipole moment. When displacing the dipole position in the other two planes orthogonal to the Cartesian unit vectors the oscillations are clearly weaker. In this case the error is constant when displacing the dipole into the direction of its momentum, while it oscillates with a period of, again, 1 mm, in the orthogonal direction. Regarding the mean RE the maps for dipoles oriented in the three Cartesian directions are nearly identical. Looking at a microscopic period defined by a cube with edge length 1 mm and vertices in the cube barycenters, we have

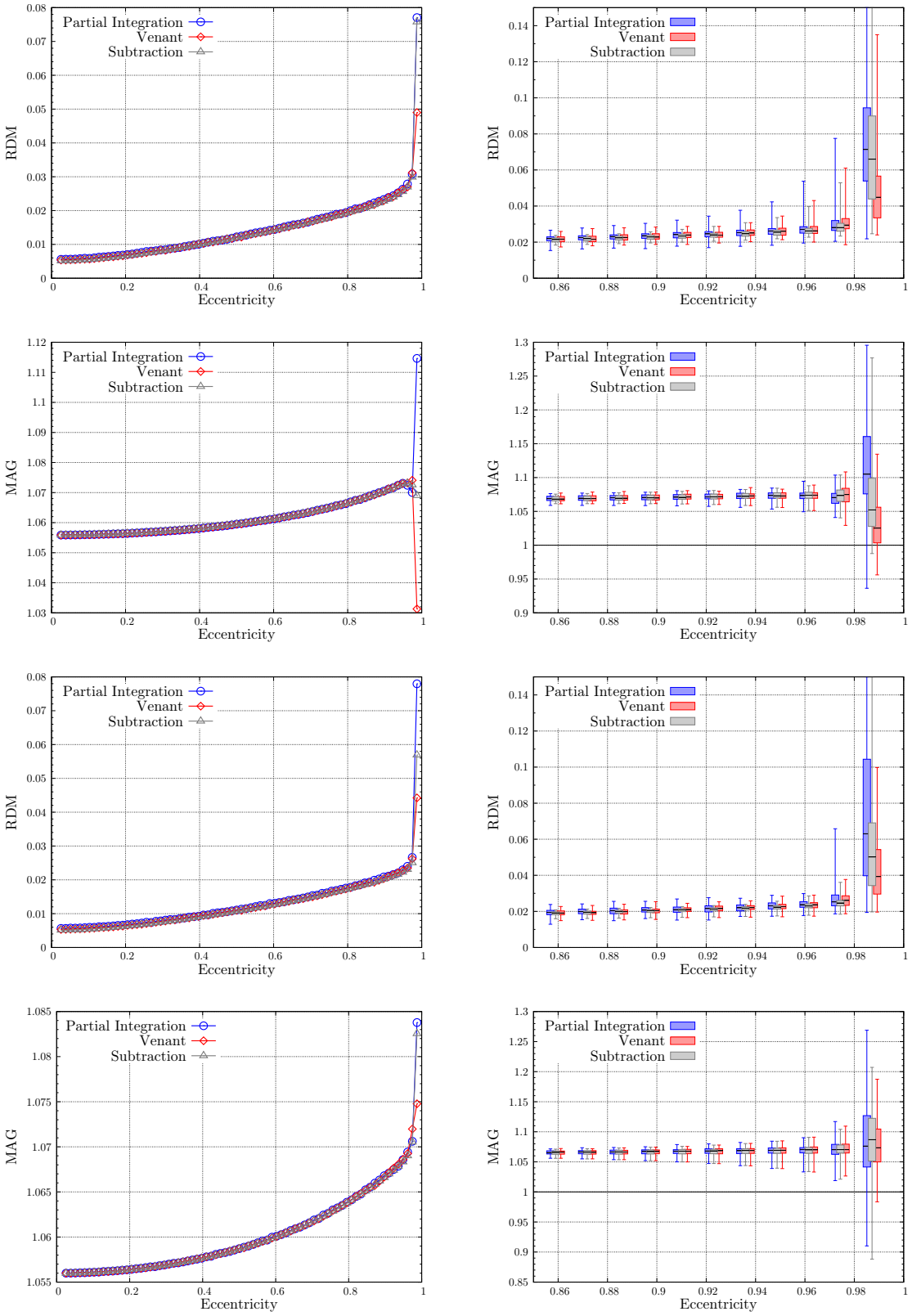

Figure 3.7: RDM and MAG versus eccentricity using the cubic four layer FE model without node shift. The upper graphs show the results for radial dipoles, the lower graphs those for tangential dipoles. Note that the axes are scaled individually. For a better readability the boxes for the Venant and the partial integration are shifted slightly into positive and negative x-direction, respectively. Larger versions of the boxplots are depicted in Figures A.14 and A.15. The maximal source eccentricity is 98.72%.

a constant error gradient in bottom left to top right direction. The error has its minimum at the top right corner and grows continuously towards the bottom left corner. In the orthogonal direction the error is nearly constant. The behavior of the error is expected to be mirrored on the other side of the sphere. Thus, we assume a constantly low error when placing dipoles directly onto the FE nodes, which was also our initial estimation.
The error distribution of the partial integration approach is contrary to those of the Venant approach. The error is nearly constant when moving the dipole in a direction orthogonal to its moment, while it oscillates when translating the dipole into the direction of its momentum. We conclude that the independency of the right hand side vector from displacements in the direction of the dipole moment is the origin of the oscillations. Hence, the oscillations have a period of 1 mm, again, resulting in continuous equi-error lines in the maps. Nevertheless, at first view the resulting distribution of the mean RE looks very similar to those of the Venant approach, except that it is shifted in all Cartesian directions by half an edge length. Therefore, we will choose cube centers as dipole positions in Chapter 4 for the partial integration approach.
Looking at the mean relative error in more detail, we notice that the straight equi-error lines of the Venant approach are bent towards the bottom left corner for the partial integration approach. Accordingly, we expect a bigger gain of accuracy through leadfield interpolation for the partial integration approach, where we will choose sources placed at cube barycenters and vertices as interpolation basis for the partial integration and the Venant approach, respectively.
Our results are compatible to previous studies where the Venant solution showed oscillatory behavior for tangential sources while the partial integration solution did for radial sources [84].

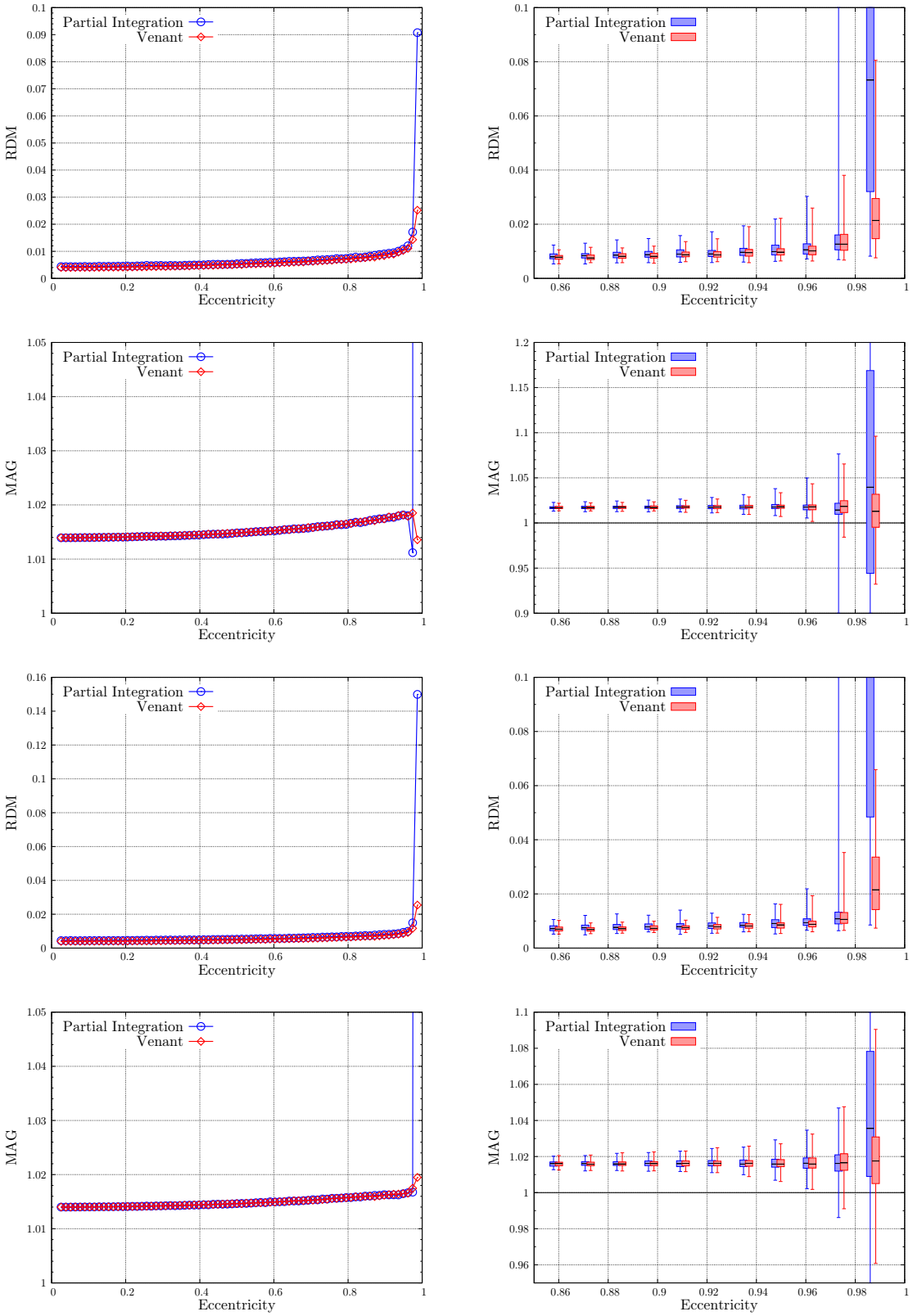

Figure 3.8: RDM and MAG versus eccentricity using the cubic four layer FE model with node shift. The upper graphs show the results for radial dipoles, the lower graphs those for tangential dipoles. Note that the axes are scaled individually. For a better readability the boxes for the Venant and the partial integration are shifted slightly into positive and negative x-direction, respectively. Larger versions of the boxplots are depicted in Figures A.17 and A.18. The maximal source eccentricity is 98.72%.

4 Leadfield Interpolation

Two challenges turned up when applying FE methods to solve the forward problem: One is the high computational demand of the subtraction approach, making it impossible to calculate forward solutions with an adequate high model resolution, e.g., 1 mm cubic, in an applicable time. Our second concern is the oscillation of the accuracy when using the Venant or the partial integration approach. While the behavior of the error is unsteady for tetrahedral meshes, it is clearly periodic for cube meshes [39, 84] and we were able to make estimations concerning the optimal dipole placement inside a particular element in the previous chapter.
Leadfield interpolation was proposed to reduce the computation time required to assemble a leadfield with BE methods [88], following the assumption that the electrode potentials vary continuously with the spatial coordinates when displacing the dipole inside a homogeneous medium with constant conductivity. Instead of calculating a forward solution for each dipole position, solutions on a predefined, (possibly) coarser grid are computed and solutions for arbitrary dipole positions and orientations are gained using interpolation.
We will apply this idea with multiple intentions. The first is to speed up the subtraction approach. Since the interpolation can be carried out very fast, the computation time mainly reduces to the effort for computing the leadfield with influence nodes placed on a rectangular grid (which will be denoted *interpolation grid* in the following), serving as basis for the interpolation. Using a coarse grid, the number of forward solutions that has to be calculated numerically can be drastically reduced to an acceptable level. Of course, the interpolation will not be exact and contributes to the overall numerical error. Thus, coarseness of the grid and required computation time have to be balanced.
Secondly, we want to reduce the oscillations occurring with the Venant and the partial integration approach. Therefore, we will generate leadfields with dipole positions adjusted to the underlying FE grid to reach minimal errors without oscillations. We will exploit our findings from Section 3.7 where we have analyzed the error distribution inside a single FE cube to estimate the optimal placement of dipoles in relation to the FE grid. After constructing our interpolation grid, the procedure is identical to the upper case. According to our results, we will use a grid where the dipoles are placed directly onto the FE nodes for the Venant approach and a grid with the dipoles placed in the barycenters of the cubes for the partial integration approach. The coarseness of the grid is not too important in this case, as the computation of a single forward solution is very fast for the direct approaches when using transfer matrices, while numerical errors induced by the interpolation should be avoided where possible.
Beside the decrease of computation time, it was shown that leadfield extrapolation can increase the numerical accuracy for superficial dipoles [88]. Therefore, the interpolation grid is *cropped*, i.e., shallow grid points exceeding a certain radius are removed since a higher eccentricity corresponds to higher numerical errors as we have observed previously (cf. Figure 4.5). Afterwards, for dipoles being located outside the grid, extrapolation is used. Of course, grid cropping is only reasonable, as long as the interpolation error does not exceed the increase of the numerical error. We will examine the impact of the three aspired advancements in Section 4.3.

4.1 Interpolation Techniques

Our starting point is a leadfield, i.e., a matrix containing the sensor potentials for dipoles placed on predefined positions and pointing in each of the three spatial directions, with the dipoles

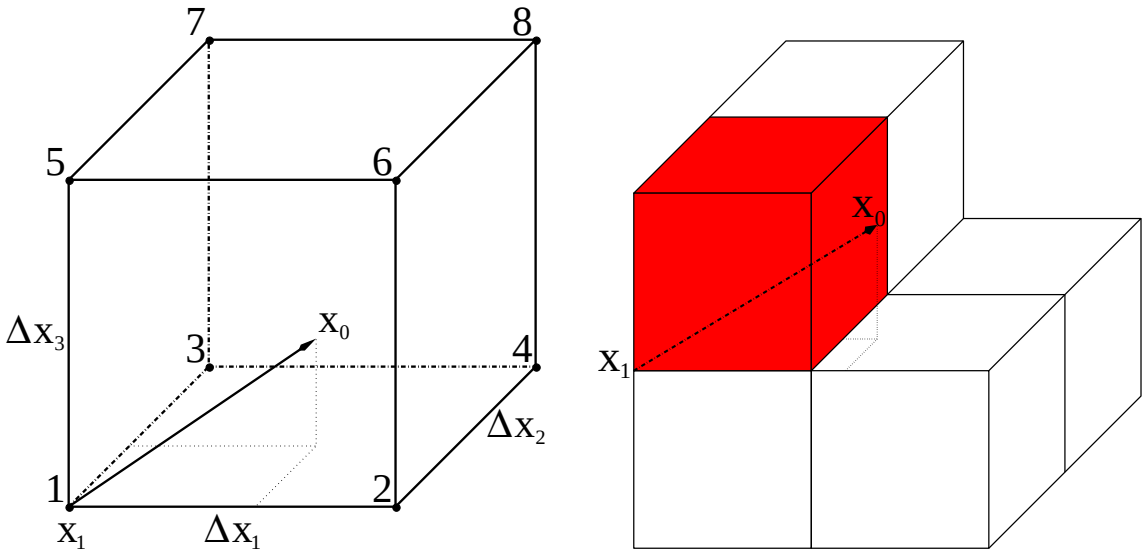

(a) x_0 is located inside the cube, interpolation is used.

(b) x_0 falls outside all cubes, the next cube (red) is chosen.

Figure 4.1: Leadfield interpolation

placed on a rectangular grid. On this basis the potential for arbitrary positions and finally dipole directions will be interpolated. Two (closely related) interpolation techniques will be used.

4.1.1 Trilinear Interpolation

Due to its simplicity we choose *trilinear interpolation*, first. It needs very few computations and is thus a very fast possibility for interpolation. Additionally, only one cubic element is needed as basis, which can be of advantage when complex geometries have to be taken into account in further numerical experiments, e.g., when using realistic head models with CSF compartment (see Chapter 6).

We consider step sizes Δx, Δy and Δz in our rectangular grid. For a source located inside a grid cube, we denote by x_1 the position of the vertex with minimal values in all three coordinates. The remaining vertices are numbered as shown in Figure 4.1(a); the potential vector corresponding to vertex i is denoted V_i, $i = 1, \ldots, 8$. The potential at dipole position x_0 is then given by the sum of the potentials at the cube nodes multiplied by weighting factors ω_i:

$$V^{int} = \sum_{i=1}^{8} \omega_i V_i. \tag{4.1}$$

We introduce local coordinates of x_0 inside the cube:

$$u_s = \frac{(x_0)_1 - (x_1)_1}{\Delta x}, \quad v_s = \frac{(x_0)_2 - (x_1)_2}{\Delta y}, \quad w_s = \frac{(x_0)_3 - (x_1)_3}{\Delta z}, \tag{4.2}$$

$u_s, v_s, w_s \in [0, 1]$. The weights are given by

$$\begin{aligned}
\omega_1 &= (1-u_s)(1-v_s)(1-w_s),\\
\omega_2 &= u_s(1-v_s)(1-w_s),\\
\omega_3 &= (1-u_s)v_s(1-w_s),\\
\omega_4 &= u_s v_s(1-w_s),\\
\omega_5 &= (1-u_s)(1-v_s)w_s,\\
\omega_6 &= u_s(1-v_s)w_s,\\
\omega_7 &= (1-u_s)v_s w_s,\\
\omega_8 &= u_s v_s w_s.
\end{aligned} \tag{4.3}$$

If the source position x_0 falls outside all grid cubes, we search the grid cube closest to x_0 and use this as a basis for extrapolation (see Figure 4.1(b)). Again, (4.1) is evaluated but the local coordinates are allowed to be negative or greater than 1.

4.1.2 Beziér Interpolation

The *Beziér interpolation* is an expansion of trilinear interpolation that may take into account more grid points and is therefore expected to lead to a more precise interpolation result (at the cost of a higher computational complexity). We assume that x_0 falls within a box of $m \cdot n \cdot p$ grid cubes, thus enveloping $(m+1) \cdot (n+1) \cdot (p+1)$ nodes. The Beziér interpolation uses a basis of *Bernstein polynomials* with degrees m, n and p along the corresponding axis. Let, again, x_1 denote the corner of the box with minimal coordinates and (u_s, v_s, w_s) the local coordinates of x_0 given through

$$u_s = \frac{(x_0)_1 - (x_1)_1}{m\Delta x}, \qquad v_s = \frac{(x_0)_2 - (x_1)_2}{n\Delta y}, \qquad w_s = \frac{(x_0)_3 - (x_1)_3}{p\Delta z}. \tag{4.4}$$

Accordingly, we have as correspondence between local and global coordinates of a grid point:

$$\begin{bmatrix} u_i = i/m \\ v_j = j/n \\ w_k = k/p \end{bmatrix} \quad \textit{and} \quad x_{i,j,k} = x_1 + \begin{pmatrix} i \cdot \Delta x \\ j \cdot \Delta y \\ k \cdot \Delta z \end{pmatrix}, \quad i = 0, \ldots, m,\ j = 0, \ldots, n,\ k = 0, \ldots, p. \tag{4.5}$$

The numerically calculated potential of a source with local coordinates (i, j, k) will be denoted $V_{i,j,k}$. The potential at x_0 is then interpolated via

$$V^{int} = \sum_{i=0}^{m} \sum_{j=0}^{n} \sum_{k=0}^{p} \omega_{i,j,k} b_{i,m}(u_s) b_{j,n}(v_s) b_{k,p}(w_s) \tag{4.6}$$

with

$$b_{\alpha,\mu}(t) = \frac{\mu!}{\alpha!(\mu-\alpha)!} t^{\alpha}(1-t)^{\mu-\alpha}, \qquad \alpha = i, j, k,\ \mu = m, n, p \tag{4.7}$$

being the Bernstein polynomial and the coefficients $\omega_{i,j,k}$ being determined by

$$\Omega = B^{-1} L \tag{4.8}$$

where:

$$\Omega = \begin{bmatrix} \omega_{0,0,0} \\ \omega_{1,0,0} \\ \omega_{2,0,0} \\ \vdots \\ \omega_{m,n,p} \end{bmatrix}, \qquad L = \begin{bmatrix} V_{0,0,0} \\ V_{1,0,0} \\ V_{2,0,0} \\ \vdots \\ V_{m,n,p} \end{bmatrix},$$

$$B = \begin{bmatrix} b_{0,m}(u_0)b_{0,n}(v_0)b_{0,p}(w_0) & b_{1,m}(u_0)b_{0,n}(v_0)b_{0,p}(w_0) & \cdots & b_{m,m}(u_0)b_{n,n}(v_0)b_{p,p}(w_0) \\ b_{0,m}(u_1)b_{0,n}(v_0)b_{0,p}(w_0) & b_{1,m}(u_1)b_{0,n}(v_0)b_{0,p}(w_0) & \cdots & b_{m,m}(u_1)b_{n,n}(v_0)b_{p,p}(w_0) \\ \vdots & \vdots & \ddots & \vdots \\ b_{0,m}(u_m)b_{0,n}(v_n)b_{0,p}(w_p) & b_{1,m}(u_m)b_{0,n}(v_n)b_{0,p}(w_p) & \cdots & b_{m,m}(u_m)b_{n,n}(v_n)b_{p,p}(w_p) \end{bmatrix}.$$

Again, extrapolation is executed by locating the box of $m \cdot n \cdot p$ grid cubes next to the source position and allowing local coordinates with values that are negative or greater than one. The matrix B is independent of the grid location and the source location x_0 and needs to be calculated and inverted only once.
For $m = n = p = 1$ the matrix B becomes the identity matrix and the Beziér interpolation coincides with the trilinear interpolation. Thus, we will not always distinguish between trilinear and Beziér interpolation in the following; trilinear interpolation is then considered as Beziér interpolation of order zero.

4.1.3 Arbitrary Dipole Directions

To gain the interpolated potential evoked by a dipole with arbitrary direction at position x_0, we make use of the linear combinability of solutions of (1.10). Thus, the potential is calculated as linear combination of the results for dipoles pointing in the three spatial directions that are stored in the leadfield. These have to be weighted by the value of the dipole momentum in the respective direction.

4.2 Implementation

We integrated both trilinear and Beziér leadfield inter- and extrapolation into the SimBio-toolbox, restricting the Beziér interpolation to cubic boxes, i.e., $m = n = p$. The implementation is straightforward. As there are different choices of the particular box possible when using Beziér interpolation of order two and higher, we decide to make use of the box whose barycenter is closest to x_0. The same choice is made when using trilinear interpolation and x_0 falls outside all grid cubes.

4.3 Experiments

We will first evaluate the leadfield interpolation using analytically calculated leadfields. This allows us to analyze the numerical error evoked by the interpolation without having to obey other influences. Trilinear as well as Beziér interpolation of order two, three and four will be considered. Beside the differences between the two interpolation techniques and orders of interpolation, we will be interested in the convergence of the results for grids with different step sizes, the computation time of the different approaches and especially the effect of grid cropping, i.e., nodes of the interpolation grid lying outside a certain radius will be removed. We will use grids with step sizes of 4, 7 and 10 mm that were cropped at radii of 74, 75.5 and 77 mm. As we are not interested in the specific error structure and for reasons of clarity, we will mainly observe the RE in the first subsection of Section 4.4.
Subsequently, we will apply leadfield interpolation to leadfields calculated with the three FE approaches and the four layer hexahedral mesh. As the computation time for a single dipole is negligible for the Venant and the partial integration approach we will use grids with step sizes of 4 mm; for the more complex subtraction approach we will use step sizes of 10 mm. Different radii of grid cropping between 70 and 75.5 mm will be tested.
We will further apply leadfield interpolation to leadfields calculated with the four layered tetrahedral meshes with the goal of smoothening the unsteady error characteristic.
The different interpolation grids used in the following are listed in Table A.7.

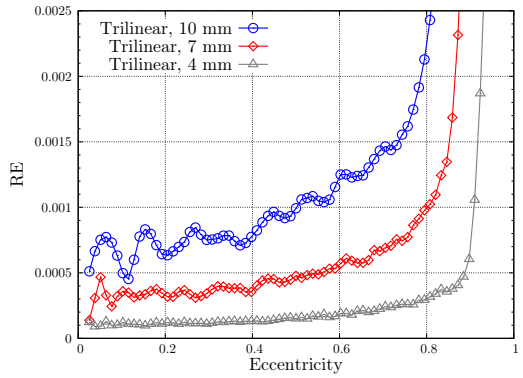

Figure 4.2: Convergence of the trilinear interpolation

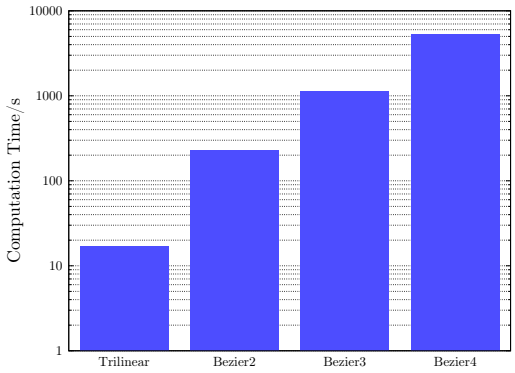

Figure 4.3: Computation times for the different interpolation approaches for 19,000 dipoles using a 4 mm grid as basis.

4.4 Results

In Figure 4.3 and Table A.8 the computation times for the different interpolation orders are shown. As to be expected, the computation time grows strongly with the order of interpolation, since the number of nodes that are taken into account (and thus the number of terms that have to be evaluated in (4.6)) grows cubic. For the highest considered order, Beziér interpolation of order four, the interpolation of the results for our set of 19,000 dipoles requires more than one hour of computation time. For this reason, order four interpolation is not further evaluated when it comes to numerically computed leadfields, as the gain of accuracy does not justify the additional computation time.

4.4.1 Analytically Calculated Leadfields

We first used leadfields calculated with the analytical solution (see Section 1.6) and interpolation grids cropped at 74.0 mm with edge lengths of 4 and 10 mm to compare the different methods directly. Our main interest concerns the effect of leadfield extrapolation. For deep sources the behavior can be denoted good-natured, as it can be observed in Figure A.22. We observe that the higher order Beziér interpolation benefits more from a finer grid than the trilinear. Using the 4 mm grid the maximal relative error stays below 0.013 with interpolation of order two and higher, even for the highest eccentricity (corresponding to an extrapolation over at least 3 mm). Trilinear interpolation results in a twice as high error; the induced error grows faster and especially earlier than for higher orders, beginning at an eccentricity between 0.86 and 0.88. When using the coarser grid as basis, the growth of the RE starts at considerable lower eccentricities for all interpolation orders. The differences between the different interpolation orders are less drastic here. The errors grow rapidly already below the cropping radius as a result of the inadequate fitting of the 10 mm grid into the sphere geometry (see Figure 4.5).
Figures 4.2 and A.22 show the convergence of the relative error with decreasing grid size. For deep sources the effect of a coarse grid is negligible as the RE is below 0.0025 for all orders of interpolation and eccentricities below 0.8. This is different for eccentric sources, where the maximal relative error halves for sources positioned at the highest eccentricity when reducing the grid size from 10 mm to 4 mm for trilinear interpolation; it even drops to its seventh part for order four Beziér interpolation. We conclude that the effect of a finer grid becomes more important when higher interpolation orders are used. A possible explanation is that the interpolation nodes have a huge extent for high interpolation orders and coarse grids, e.g., forming a box of 40 mm $\times$ 40 mm $\times$ 40 mm for interpolation of order four and a 10 mm grid; actually, only few boxes of these shape are contained in the grid, necessitating extrapolation into relatively large distances.

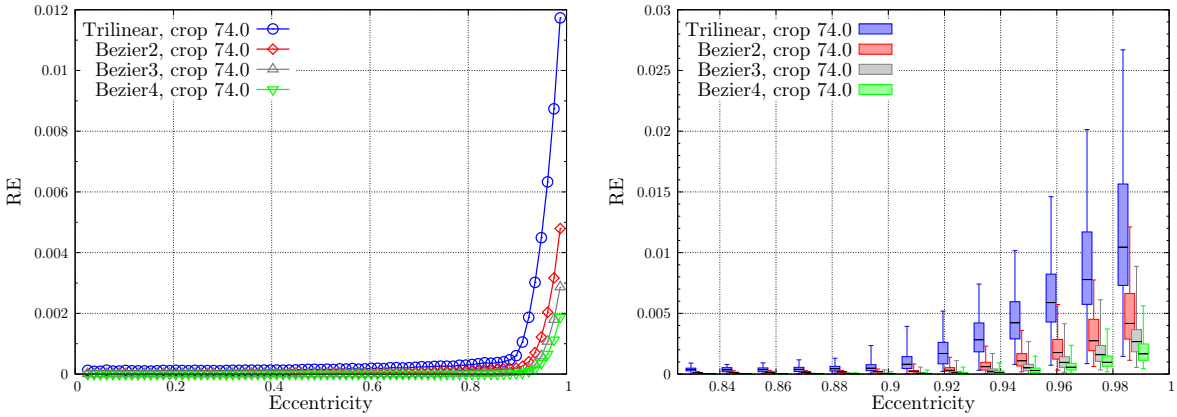

(a) RE for different interpolation approaches/orders for 4 mm grid cropped at a radius of 74.0 mm.

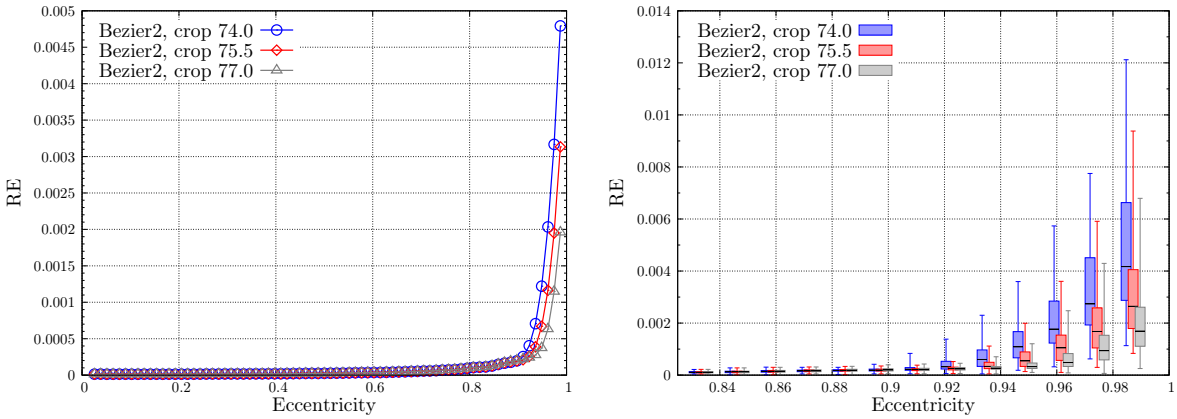

(b) RE for order two Beziér interpolation for 4 mm grid cropped at different radii.

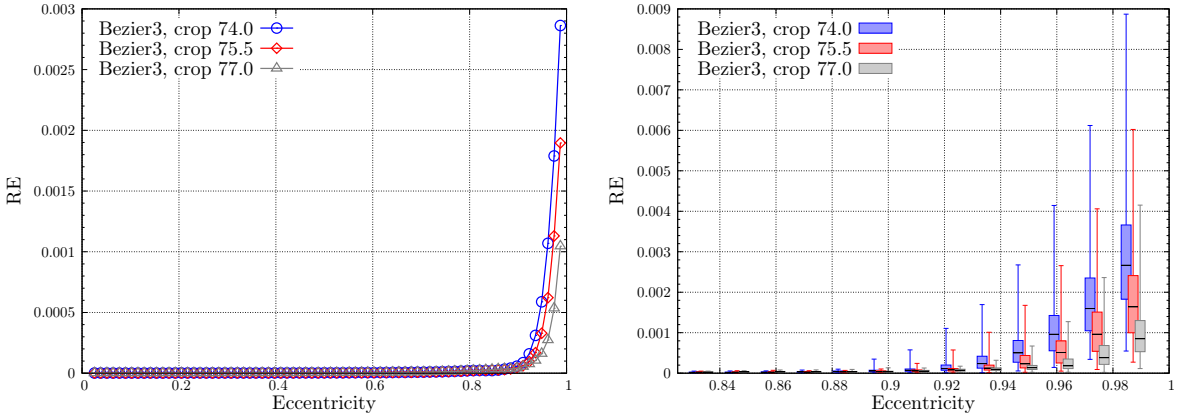

(c) RE for order three Beziér interpolation for 4 mm grid cropped at different radii.

Figure 4.4: RE versus eccentricity for 4mm grid. Note that the axes are scaled individually. The boxes are slightly shifted from their original x-position for a better readability. The maximal source eccentricity is 98.72%.

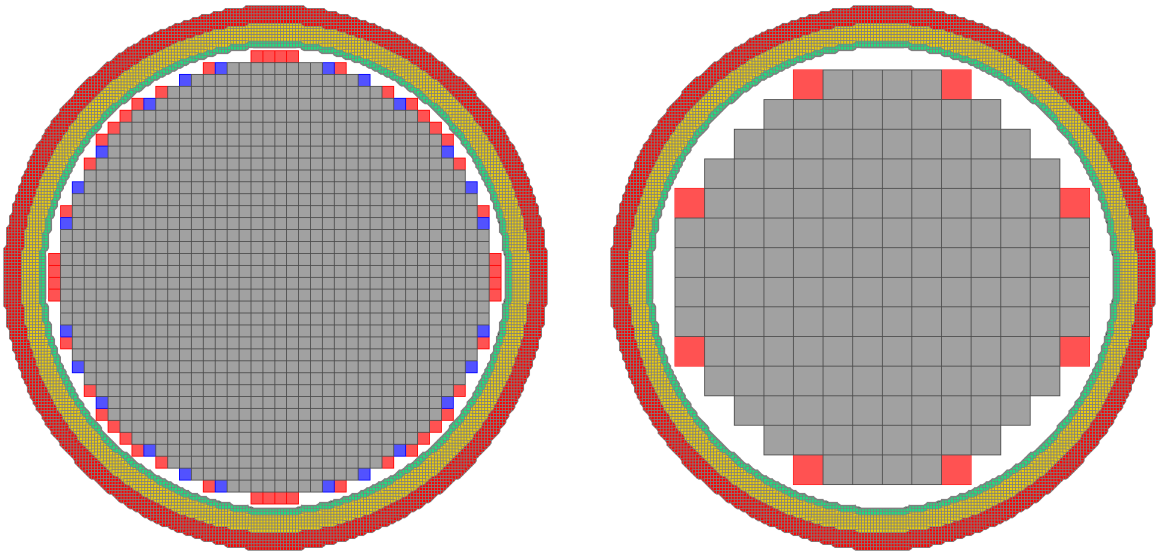

Figure 4.5: The 4 mm (left) and 10 mm (right) interpolation grid. The cubes inside a radius of 74 mm are grey, blue cubes are added when cropping at a radius of 75.5 mm and red cubes at a radius of 77 mm. Slice is made through the $x = 127$ mm plane.

A second effect observable for deep sources in these figures is a slight oscillation of the mean RE. It is probably evoked by the paraxial alignment of the grids and their symmetry relative to the center of the sphere, having a node (4 mm, 10 mm) or the barycenter of a cube (7 mm) sited at the origin. Particularly for the trilinear interpolation on the 10 mm grid it is nicely visible that the error drops in the vicinity of a node. For more eccentric sources the oscillation is hidden by other error sources and the previous averaging.

Next, we want to explore the effect of grid cropping. We concentrate on Beziér interpolation of order two and three from now on, since they represent the best compromise between accuracy and computation time in our opinion. These orders will be exclusively used with numerically calculated leadfields, where we will use grid cropping up to a radius of 70 mm, making the application of trilinear interpolation not reasonable.

The RE stays below 0.01 for almost all sources and all applied cropping radii in the 4 mm case (see Figures 4.4(b) and 4.4(c)). The differences between order two and three Beziér interpolation are negligible. In both cases the increase of the RE when sources are more eccentric is considerably lower than observed for the Venant or the partial integration approach with cubic meshes (Figure A.19). Hence, grid cropping at a radius of at least 74 mm might enable us to reduce the errors for sources with high eccentricity significantly. We will also use grids cropped at radii of 70 and 72 mm with the 1 mm cube model to discover whether a further improvement is achieved or if the interpolation error exceeds the numerical error of the forward calculation.

Using the 10 mm grid the effect of grid cropping is weaker than in the 4 mm case. Since the 10 mm grid approximates the inner volume worse than the finer 4 mm grid does, there are many source positions where extrapolation is already needed for a cropping radius of 77 mm, while only few additional cubes are erased when the cropping radius is further decreased (see Figure 4.5). Therefore, the differences between the three different radii are reduced, being below 0.01 regarding the maximal RDM. Comparing these results to Figure 3.7 we decide to use a grid cropped at a radius of 74 mm with the subtraction approach. With the coarse grid size of 10 mm we will have to observe whether a noticeable interpolation error is introduced.

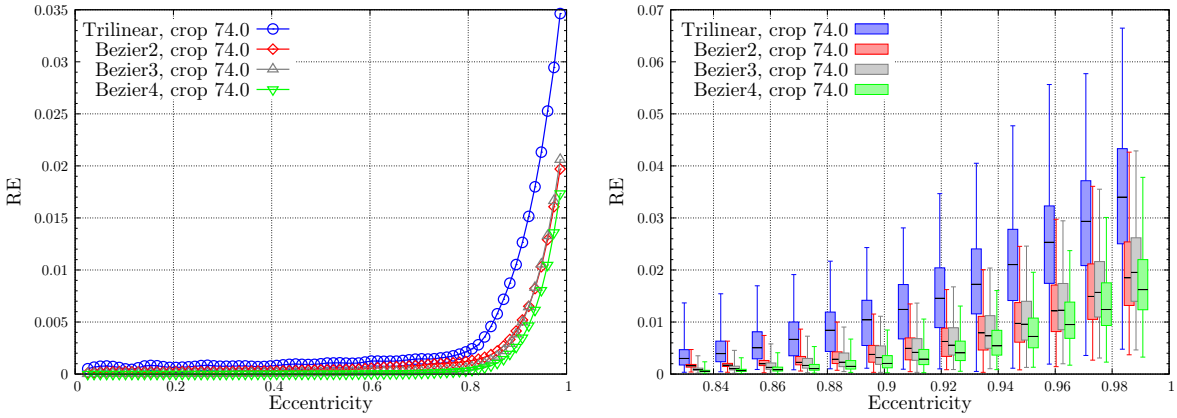

(a) RE for different interpolation approaches/orders for 10 mm grid cropped at a radius of 74.0 mm.

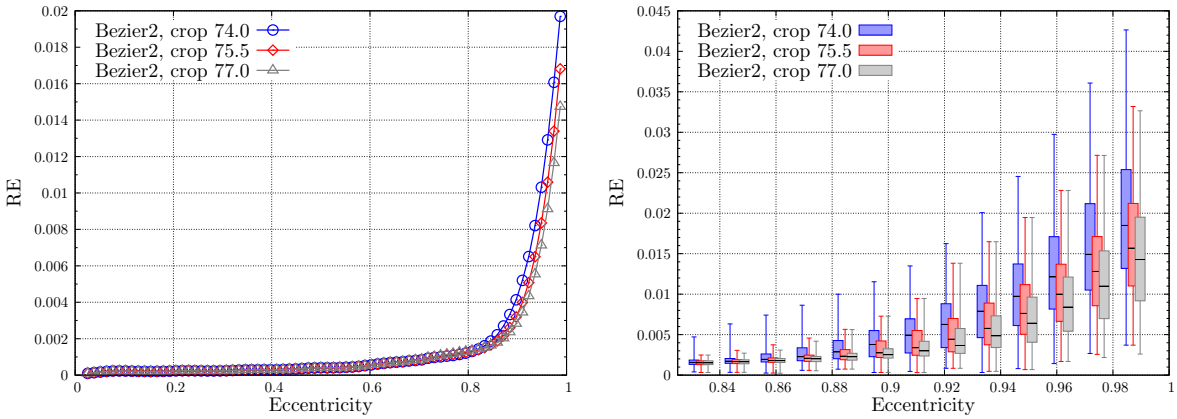

(b) RE for order two Beziér interpolation for 10 mm grid cropped at different radii.

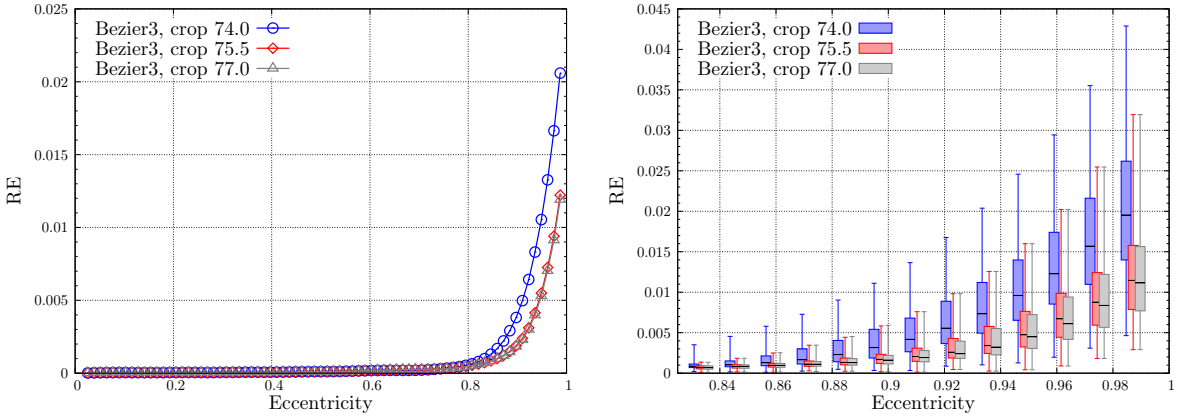

(c) RE for order three Beziér interpolation for 10 mm grid cropped at different radii.

Figure 4.6: RE versus eccentricity for 10mm grid. Note that the axes are scaled individually. The boxes are slightly shifted from their original x-position for a better readability. The maximal source eccentricity is 98.72%.

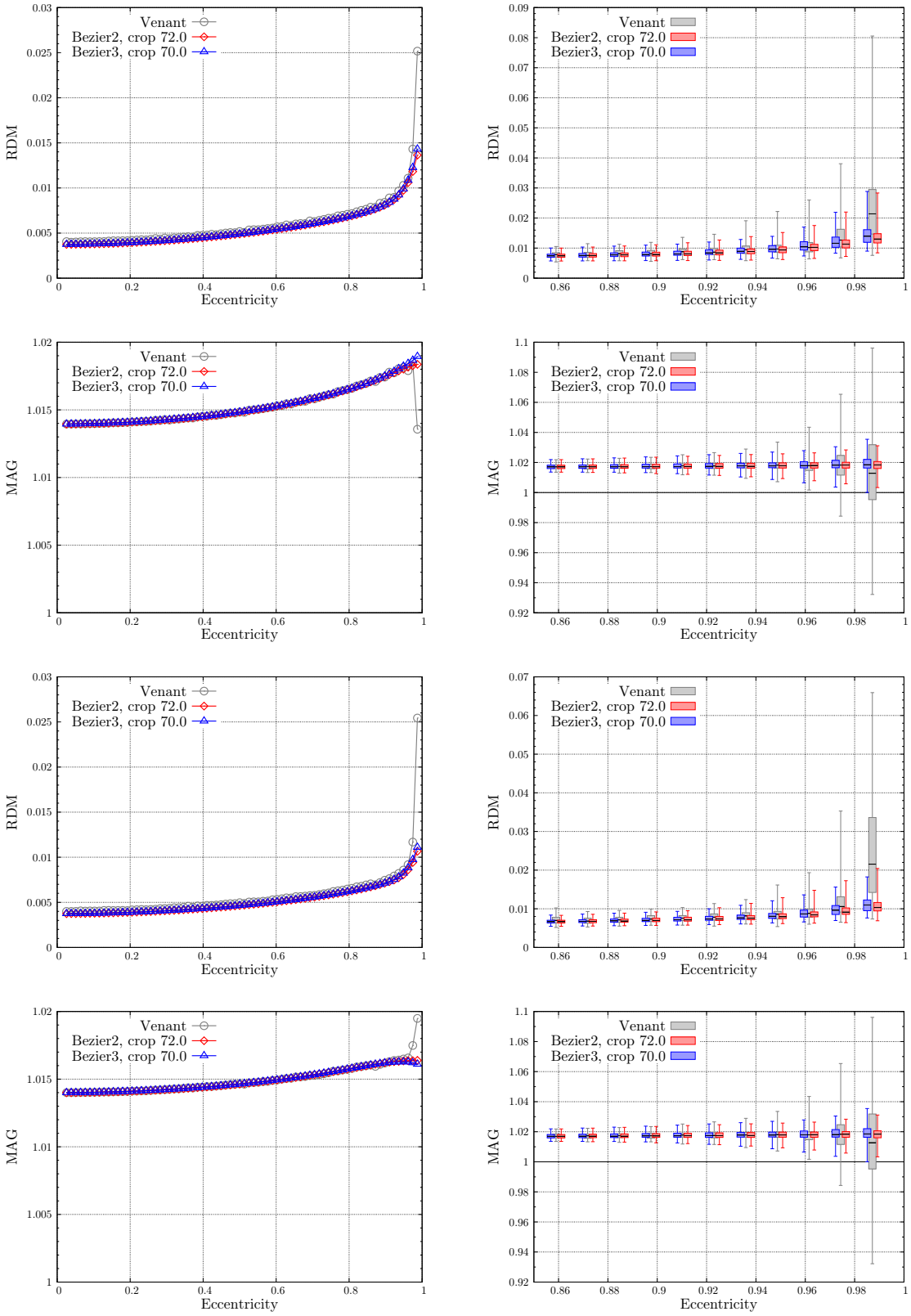

Figure 4.7: RDM and MAG versus eccentricity for leadfield interpolation with Beziér interpolation using a leadfield computed with the Venant approach. The upper graphs show the results for radial dipoles, the lower those for tangential dipoles. Note that the axes are scaled individually. The boxes are slightly shifted from their original x-position for a better readability. The maximal source eccentricity is 98.72%.

4.4.2 Numerically Calculated Leadfields

Hexahedra Models

Our examination of the error distributions in the previous chapter allows us to select the positions of the grid nodes in a manner that promises an optimal interpolation result for the direct approaches. Accordingly, we place the nodes of the interpolation grid directly onto FE nodes for the Venant approach, while we choose cube barycenters for the partial integration approach. We will choose cube barycenters for the subtraction approach, too, in order to avoid possible numerical instabilities when sources are very close to FE nodes.

We will first examine the direct approaches. In order to estimate the cropping radius generating an optimal extrapolation result, we calculated solutions with grids cropped at different radii (70 mm, 72 mm, 74 mm, 75.5 mm) with Beziér interpolation of both order two and three.

Looking at the numerical errors presented in the previous chapter we notice that the loss of numerical accuracy is moderate up to an eccentricity of about 0.93, i.e., a radius of 72.5 mm, and increasing more and more for higher eccentricities. We further note that the numerical instability induced by loaded nodes close to a conductivity jump generates errors exceeding the error of leadfield extrapolation over a distance of 5 mm by far. We conclude that a cropping radius of at least 74 mm should lead to the best results.

Indeed, we found a cropping radius of 72 mm to perform best with interpolation of order two and both direct approaches (see Figures A.23 and A.24). This is a remarkable result, since extrapolation over a distance of more than 7 mm is executed for the most eccentric sources. For interpolation of order three, the result can even be improved by further cropping, best results (surely only for spherical models) are reached with a cropping radius of 70 mm.

We finally compare the best results of the different interpolation orders. For the Venant approach we find order two with cropping at 72 mm and order three with cropping at 70 mm performing almost equally well, the resulting diagrams are shown in Figure 4.7. Only a small improvement of both RDM and MAG for deep sources as result of adjustedly choosing the interpolation nodes is visible. This effect will be pointed out more explicitly later on. However, the errors for shallow sources could be reduced drastically by avoiding loaded nodes being close to or placed in the CSF compartment. We gain a RDM below 0.02 for radial and below 0.03 for tangential sources. The MAG was strongly improved, either.

The results regarding RDM and MAG for the partial integration approach are nearly similar to those achieved in the Venant case (see Figure 4.8). Since the original data had a worse accuracy compared to the Venant case, the absolute improvement is even larger. Especially for the most eccentric set of sources, we observe a considerable gain of accuracy. Due to the higher amplitude of the oscillation, we observe a notable profit for deep sources, too. The results for the different orders differ more in this case with order two performing clearly best for radial sources and order three with a small advance for tangential ones.

To illustrate the use of leadfield interpolation for the Venant and the partial integration approach with cubic meshes, we generated maps similar to those shown in the previous chapter (see Figures A.25 and A.26). We used interpolation order two with a 4mm grid cropped at 72 mm in both cases, since this combination effected the biggest gain of accuracy previously. The upper row illustrates mean RE, RDM and MAG without leadfield interpolation, the lower one the result after the interpolation. For both approaches the errors are clearly reduced by applying leadfield interpolation; for the partial integration approach we achieve a nearly optimal result. The oscillations are erased for each of the three error measures while the absolute errors are reduced nearly to the minimum. As expected, the effect for the Venant approach is less impressive. While the oscillations are equally well mollified, the error is located in the mid-range of the spectrum, approving our assumption from the previous chapter.

Concentrating on the behavior for highly eccentric sources, we created Figures A.27 and A.28 where we exemplarily depict the result of leadfield extrapolation. In each of the three introduced

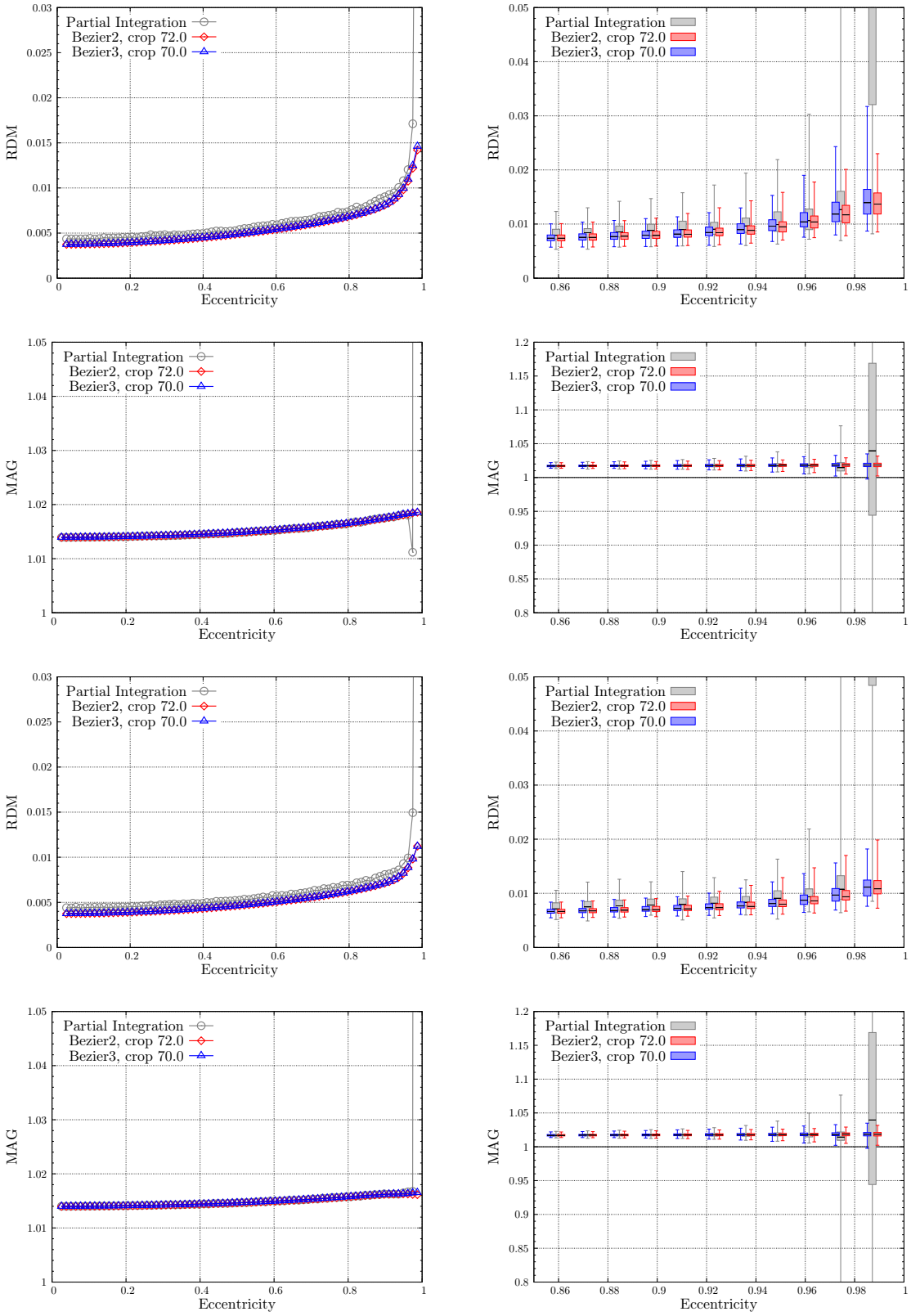

Figure 4.8: RDM and MAG versus eccentricity for leadfield interpolation with Beziér interpolation using a leadfield computed with the partial integration approach. The upper graphs show the results for radial dipoles, the lower those for tangential dipoles. Note that the axes are scaled individually. The boxes are slightly shifted from their original x-position for a better readability. The maximal source eccentricity is 98.72%.

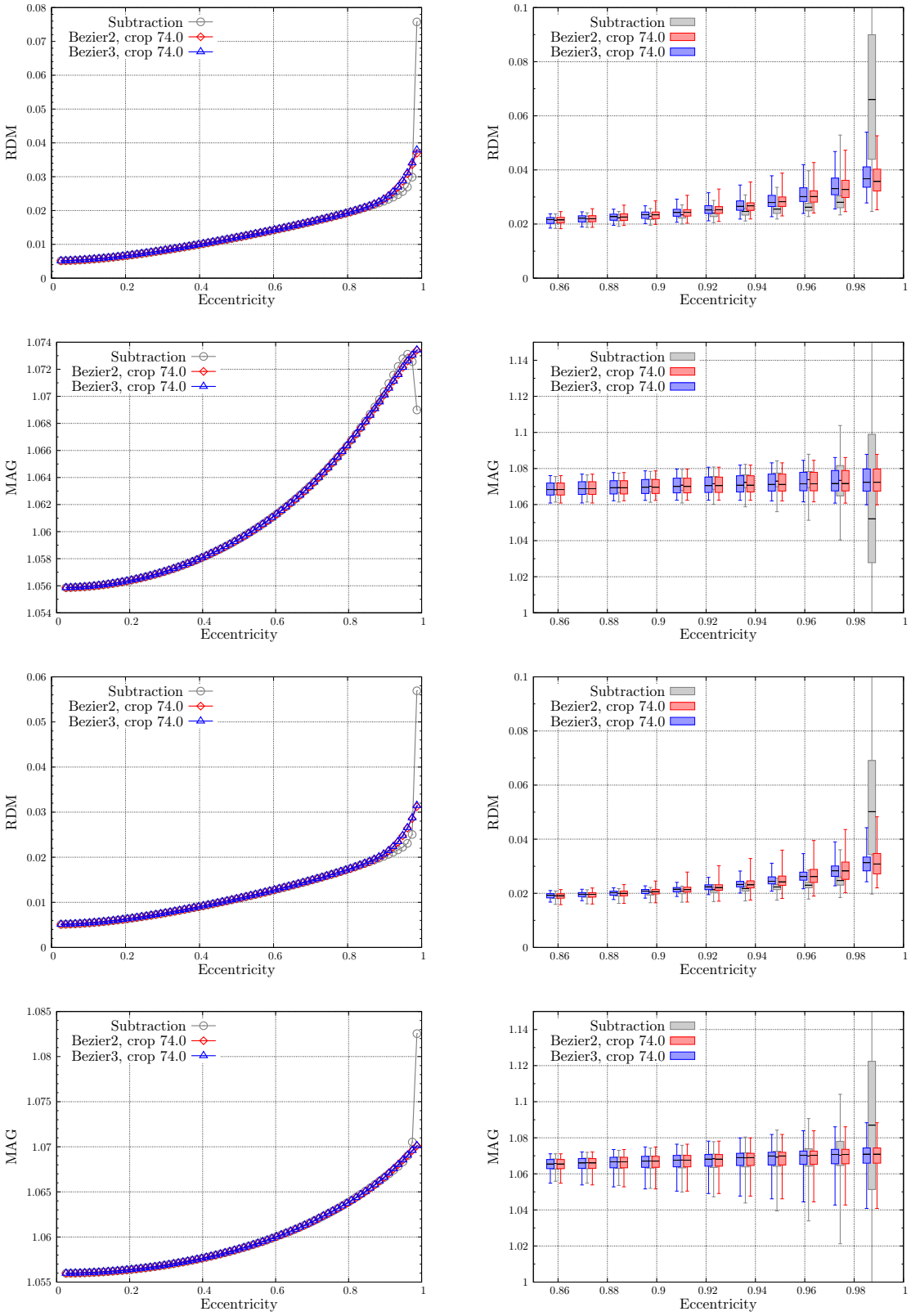

Figure 4.9: RDM and MAG versus eccentricity for leadfield interpolation with Beziér interpolation using a leadfield computed with the subtraction approach. The upper graphs show the results for radial dipoles, the lower those for tangential dipoles. Note that the axes are scaled individually. The boxes are slightly shifted from their original x-position for a better readability. The maximal source eccentricity is 98.72%.

error measures we find a significantly improved accuracy, gaining a RE below 0.03 directly beneath the surface.

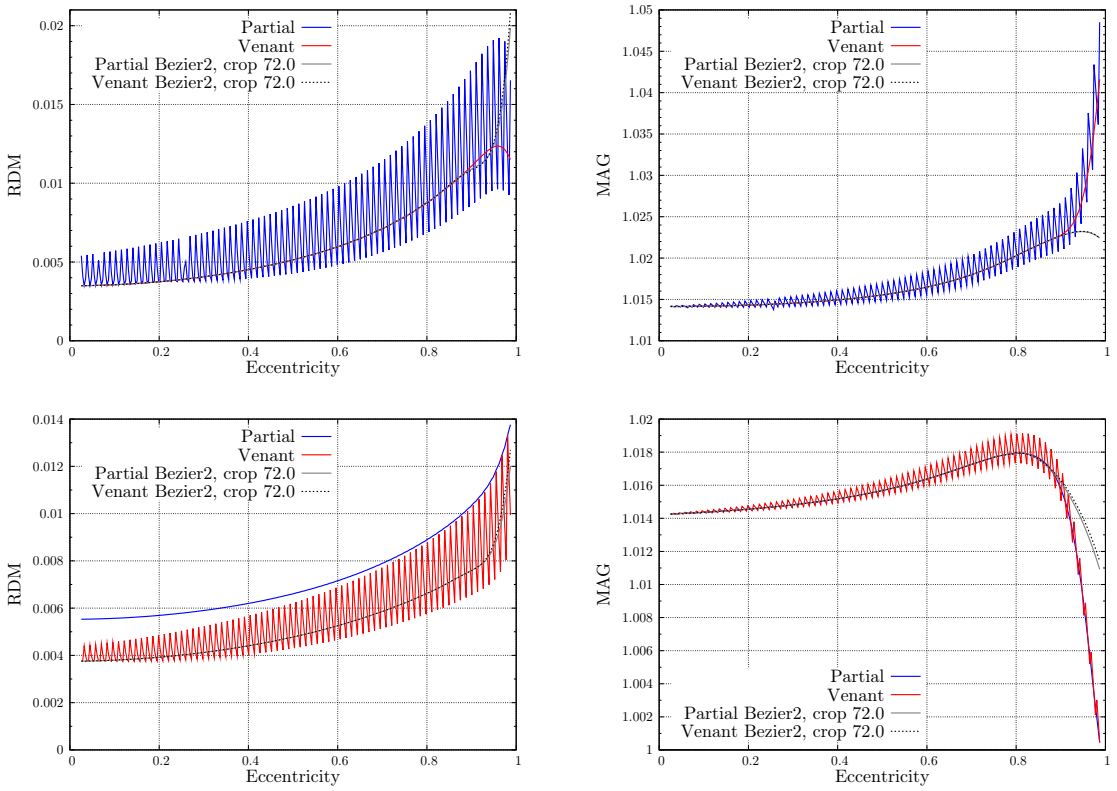

Figure 4.10: RDM and MAG versus eccentricity with and without leadfield interpolation. The upper graphs show the results for radial dipoles, the lower those for tangential dipoles. Note that the axes are scaled individually. The dipoles were placed at $(127, y, 127)^T$. The maximal source eccentricity is 98.72%.

For the sake of comparability we also computed results in a single ray scenario similar to that examined in [84] (cf. Figure 4.10). We placed sources parallel to the y-axis in 0.25 mm steps. We can, again, nicely observe how the oscillations are smoothed, gaining a nearly optimal result for sources close to the origin. With higher eccentricity the position of the minimal error inside a cube apparently moves apart from our previous estimation leading to a minimal higher error. We can once again observe the higher oscillation amplitude of the partial integration approach. We note that the partial integration approach without interpolation was discriminated in this scenario since its minimal error is reached in the cube barycenters, but this does not affect our intended conclusion.

As final examination with cubic models, we evaluated leadfield interpolation in combination with the subtraction approach, using a grid cropped at 74 mm as basis, results are shown in Figure 4.9. Contrary to the direct approaches, the accuracy could be improved only for the most eccentric sources. Indeed, it is already remarkable that we find only slightly higher overall errors when reminding that we used a coarse 10 mm grid. Thus, we achieved an extreme speed-up - only about 5100 sources instead of 19,000 sources had to be calculated - accompanied by a negligible loss of accuracy and an improved result for very eccentric sources (see Figure 4.11(a)). Of course, the speed-up increases when the number of forward calculations that have to be executed rises.

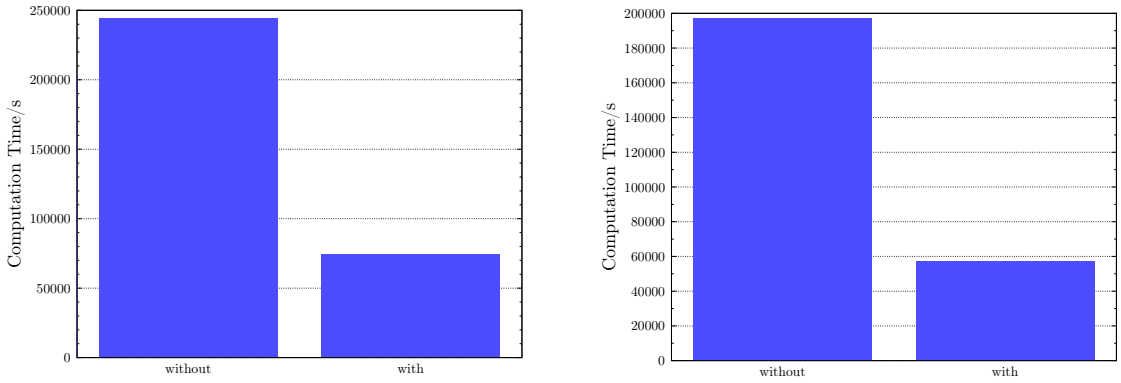

(a) Hexahedra model **(b)** Tetrahedra model

Figure 4.11: Speed-up of the subtraction approach by the use of leadfield interpolation

Tetrahedra Meshes

When applying leadfield interpolation with tetrahedral meshes, we decided to neglect grid cropping. Our main interest concerns the reduction of oscillations, while the numerical accuracy was only problematic for very high eccentricities using the tetrahedral meshes. Thus, we choose a cropping radius of 77.0 mm, the grid sizes remained unchanged.
Compared to the positive results for hexahedral meshes, the effect of leadfield interpolation for tetrahedral meshes and the direct approaches has only poor relevance (see Figures 4.12 and 4.13). The intended mollifying of the unsteady behavior of the direct approaches has not occurred, in contrast we even have to accept a loss of accuracy for some sources. Leadfield extrapolation could neither improve the result for high eccentricities nor for radial dipole moments, leading to a more than twice as high RDM for the Venant and the partial integration approach. Only the accuracy of the Venant approach with tangential sources was reduced by preventing outliers.
Using the subtraction approach we achieved a major speed-up by a factor of three at the cost of only a moderate loss of accuracy, again (see Figure 4.11(b) and 4.14). Nevertheless, the accuracy could not be further improved resulting in increased errors for eccentric sources.

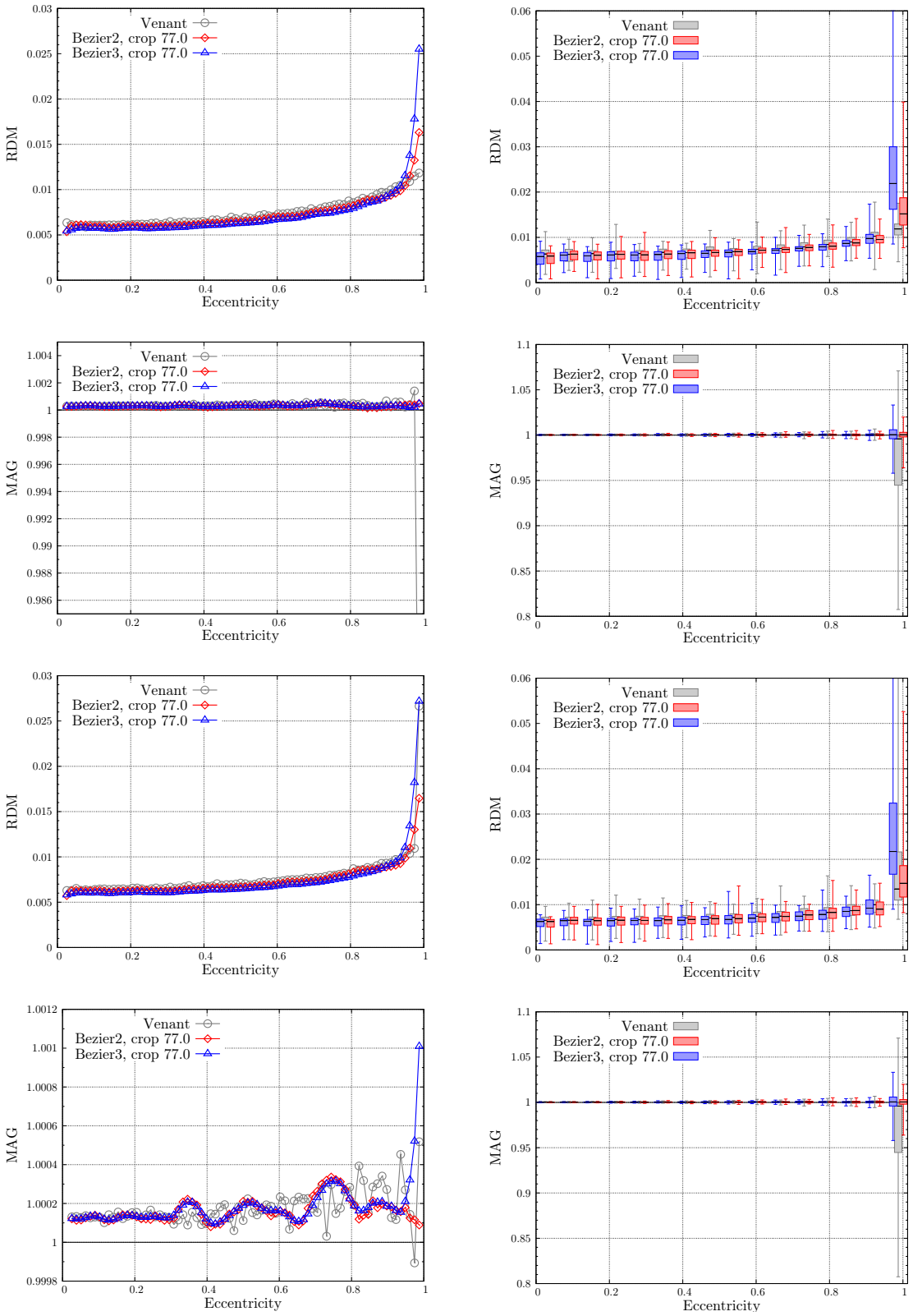

Figure 4.12: RDM and MAG versus eccentricity for leadfield interpolation with Beziér interpolation using a leadfield computed with the Venant approach and a tetrahedra model. The upper graphs show the results for radial dipoles, the lower those for tangential dipoles. Note that the axes are scaled individually. The boxes are slightly shifted from their original x-position for a better readability. The maximal source eccentricity is 98.72%.

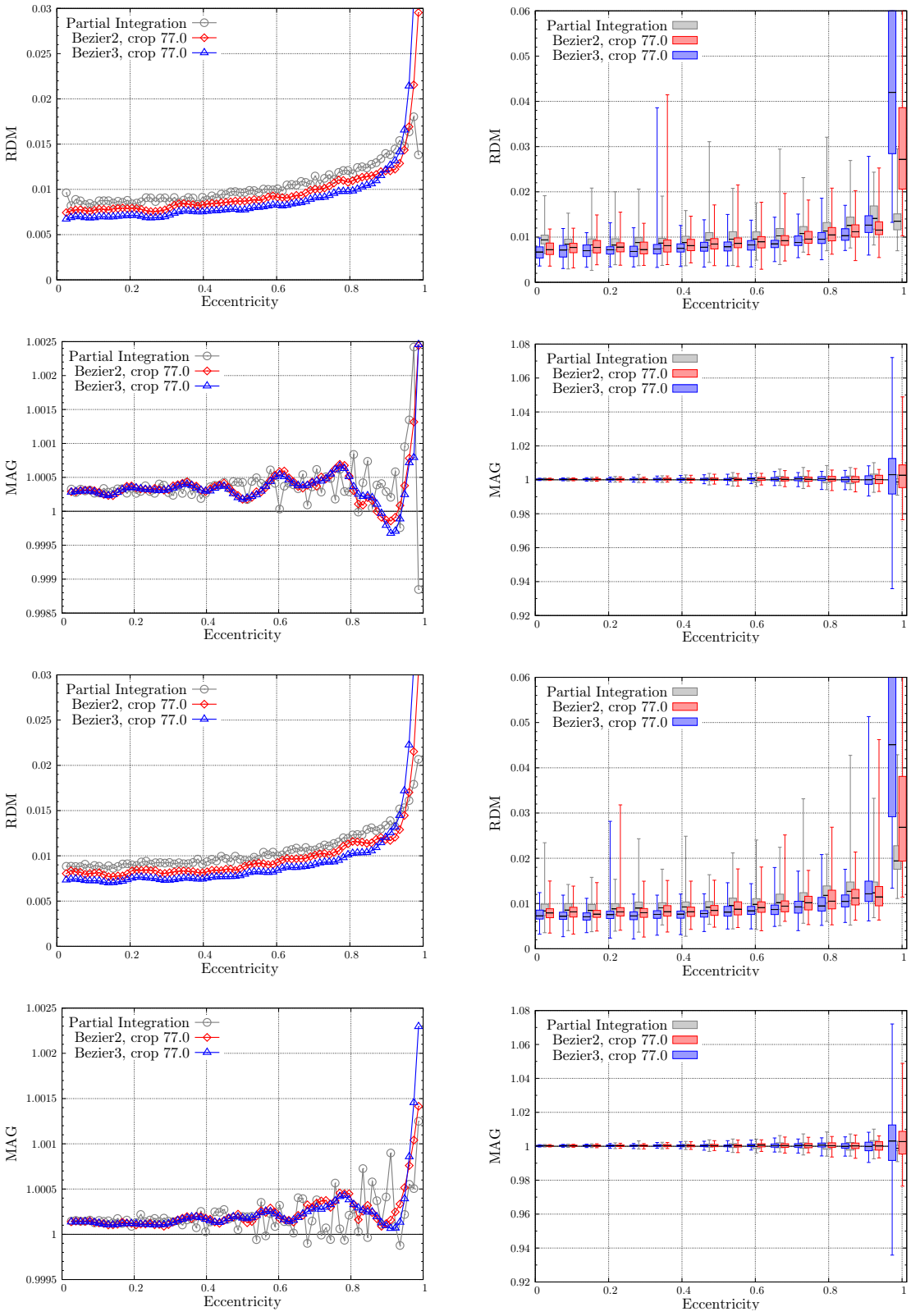

Figure 4.13: RDM and MAG versus eccentricity for leadfield interpolation with Beziér interpolation using a leadfield computed with the partial integration approach and a tetrahedra model. The upper graphs show the results for radial dipoles, the lower those for tangential dipoles. Note that the axes are scaled individually. The boxes are slightly shifted from their original x-position for a better readability. The maximal source eccentricity is 98.72%.

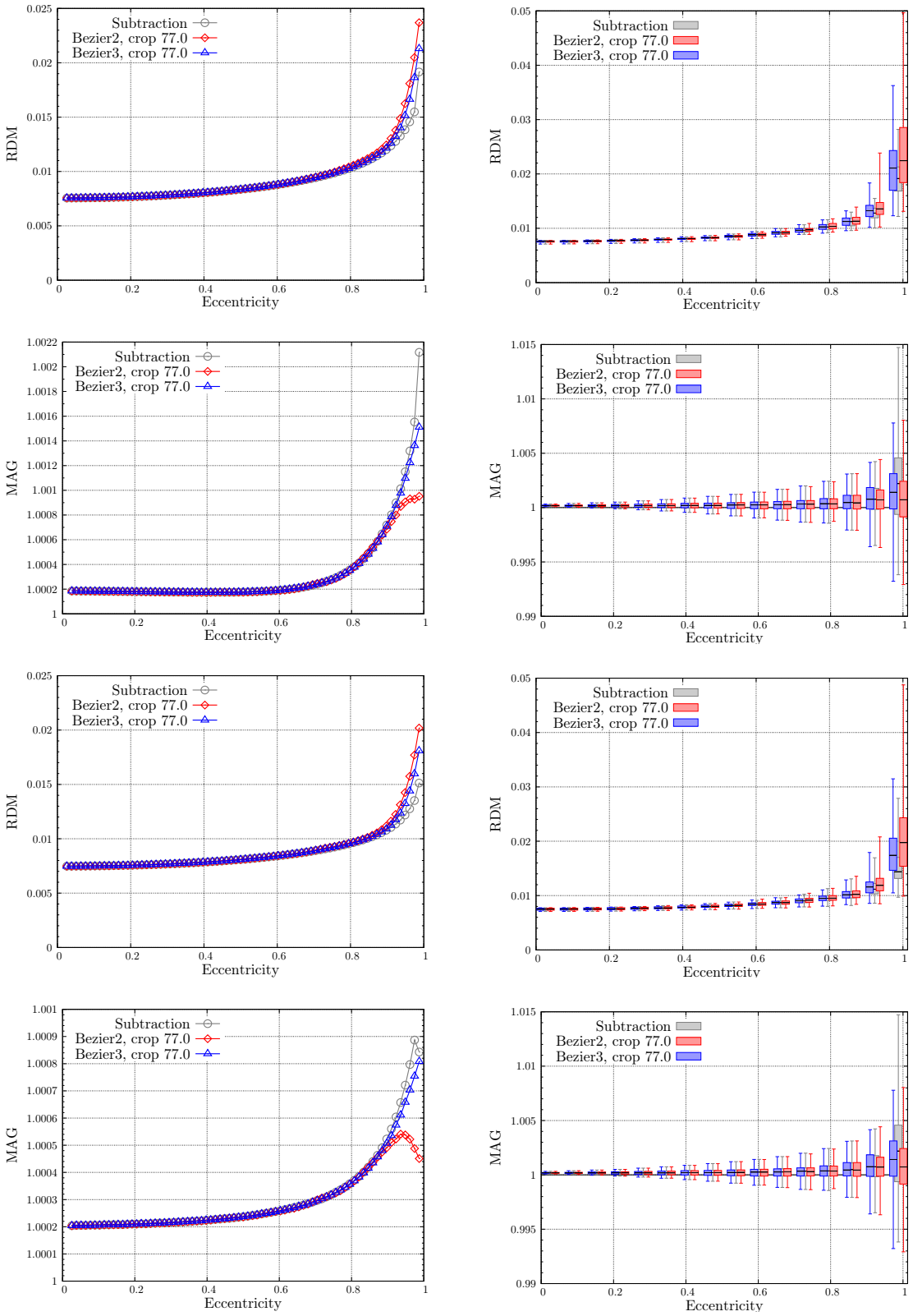

Figure 4.14: RDM and MAG versus eccentricity for leadfield interpolation with Beziér interpolation using a leadfield computed with the subtraction approach and a tetrahedra model. The upper graphs show the results for radial dipoles, the lower those for tangential dipoles. Note that the axes are scaled individually. The boxes are slightly shifted from their original x-position for a better readability. The maximal source eccentricity is 98.72%.

5 Conclusion

The three major goals of this thesis were:

- Compare the accuracy of different numerical solution approaches in a three-layer sphere model,
- analyze the oscillations and improve the accuracy of the direct FE approaches with hexahedral models,
- reduce the computation time and improve the accuracy of the subtraction FE approach.

In Chapters 2 and 3 we showed that the symmetric BEM outperforms the common double-layer BE as well as the FE approaches regarding accuracy in a three-layer sphere model, being the most accurate solution approach in this scenario. The setup time was taken as reference to provide a valid basis for the comparison. However, we demonstrated that the error induced by neglecting the CSF compartment clearly exceeds the numerical errors of the FE methods and found the Venant approach to provide the best compromise of accuracy and time consumption for both tetrahedral and hexahedral four-layer sphere meshes. Furthermore, we were able to confirm our previous estimation concerning the distribution of numerical errors and the optimal placement of a dipole inside a single cubic element in Chapter 3. We provided an explanation for the origin of the oscillations for the partial integration approach.
Applying our previous results, we were able to show that the oscillations of the direct FE approaches with hexahedral meshes can be erased using leadfield interpolation in Chapter 4. We increased the numerical accuracy for eccentric sources and, additionally, gained a slight improvement for deep sources. We pointed out that leadfield interpolation can clearly reduce the computation time when applied with the subtraction approach charging only a marginal loss of accuracy for both tetrahedral and hexahedral meshes. In the case of a hexahedral mesh the accuracy for highly eccentric sources can be improved, too. We found a nearly equal accuracy and time consumption for Venant and partial integration approach in combination with leadfield interpolation, clearly outperforming the subtraction approach.
We did not achieve the hoped for side effect of mollifying the irregular oscillations of the direct approaches with tetrahedral meshes and were, furthermore, not able to achieve an increase of accuracy for eccentric sources. We noted that the accuracy of the subtraction approach is clearly affected by the missing implementation of node-shifted meshes, discriminating it against the direct approaches.

6 Outlook

The promising results concerning the use of leadfield interpolation achieved in this thesis have a limited significance with regard to realistic head models. Therefore, further scenarios have to be evaluated:

- Application of leadfield interpolation in a realistically shaped, isotropic four compartment (i.e. skin, skull spongiosa, skull compacta, brain) head model,
- application of leadfield interpolation in a multi-layer sphere model with anisotropic white matter, i.e., at least five layered,
- leadfield interpolation in a realistically shaped six compartment (skin, skull compacta, skull spongiosa, CSF, grey matter, white matter) head model with realistic white matter anisotropy.

In each scenario, the results will compete with the common BE and FE approaches. However, the lack of an analytical solution constrains the possibilities to find "the optimal solution" in a realistic head model.
Besides the combination of leadfield interpolation with Venant and partial integration approach, the *H-matrix implementation* of the subtraction approach is expected to effect a further speed-up and should be examined, also in combination with leadfield interpolation. The yet not achieved mollifying effect for the direct approaches in combination with tetrahedral meshes might be achieved by the implementation of further interpolation techniques that are not restricted to a rectangular distribution of the interpolation nodes, e.g., 3D-splines or linear interpolation on the basis of tetrahedral grids.
Aside leadfield interpolation, some ideas exist to further improve the direct approaches. Especially the accuracy of the partial integration approach might be increased by the use of higher order ansatz functions, aiming to fill the lack of spatial information (particularly in the direction of the dipole moment) in a particular source element and to suppress the oscillations at their origin, but also the Venant and the subtraction approach are expected to benefit from higher order ansatz functions. Furthermore, the Venant approach might profit from an implementation preventing the placement of monopoles in adjacent layers.
Perspectively, alternative dipole models have to be considered, since a better approximation of an activated brain region may be achieved and the singularity at the source position may be erased. One possibility to realize this goal are the already mentioned Whitney forms, further ideas, e.g., the description of the source term using B-splines, might be implemented with the partial integration approach.

A Appendix

A.1 Tables

Table A.1: Parametrization of the isotropic three layer sphere model

Medium	Brain	Skull	Scalp
Outer shell radius	80 mm	86 mm	92 mm
Conductivity	0.33 S/m	0.0042 S/m	0.33 S/m

Table A.2: Parametrization of the isotropic four layer sphere model

Medium	Brain	CSF	Skull	Scalp
Outer shell radius	78 mm	80 mm	86 mm	92 mm
Conductivity	1.79 S/m	0.33 S/m	0.0042 S/m	0.33 S/m

Table A.3: Computation times of the different BE forward solutions. Setup measures the time for computing and inverting the BE head matrix. One forward computation consists of the setup of the right hand side vector and the resulting matrix multiplication. Leadfield indicates the overall time for 19,000 forward computations.

Forward Model	Model	Solver	Setup	Forward	Leadfield
Double-Layer	2056-2056-2056	SimBio	198 min 58 s	100.9 ms	230 min 56 s
Symmetric	2056-2056-2056	OpenMEEG	115 min 39 s	296.9 ms	209 min 41 s
Symmetric	2056-2056-2056	OMEEG NoAd	115 min 39 s	69.4 ms	137 min 37 s

Table A.4: Tetgen parameters of the tetrahedral FE models

Model	nodes	elements	quality constraint	volume constraint / mm^3
802k-4layer-dense	801633	4985234	1.1	1.12
818k-3layer-dense	818048	5097930	1.1	1.12
519k-4layer-sparse	518730	3159575	1.1	0.63 / -1
497k-3layer-sparse	497108	3027991	1.1	0.63 / -1

Table A.5: Tetgen parameters of the cubic FE models

Model	nodes	elements	edge length / mm	node shift
1mm-3layer	3342701	3262312	1	no
1mm-3layer-ns	3342701	3262312	1	yes
1mm-4layer	3342701	3262312	1	no
1mm-4layer-ns	3342701	3262312	1	yes

Table A.6: Computation times of the different FE forward solutions. Setup measures the time for computing the FE transfer matrix. One forward computation consists of the setup of the right hand side vector and the resulting matrix multiplication. Leadfield indicates the overall time for 19,000 forward computations.

Forward Model	Model	Setup	Forward	Leadfield
Venant	802k-4layer-dense	99 min 26 s	23.4 ms	106 min 51 s
Partial integration	802k-4layer-dense	98 min 58 s	65.1 ms	119 min 34 s
Subtraction	519k-4layer-sparse	76 min 30 s	10.5 s	3394 min 38 s
Venant	818k-3layer-dense	106 min 8 s	23.0 ms	113 min 25 s
Partial integration	818k-3layer-dense	107 min 23 s	65.8 ms	128 min 14 s
Subtraction	497k-3layer-sparse	73 min 14 s	7.9 s	2579 min 18 s
Venant	1mm-4layer-ns	192 min 57 s	166.2 ms	245 min 34 s
Partial integration	1mm-4layer-ns	183 min 43 s	224.8 ms	254 min 55 s
Subtraction	1mm-4layer	187 min 55 s	12.3 s	4075 min 3 s

Table A.7: Number of nodes for the different interpolation grids.

Forward approach	Grid size	Cropping radius	Number of nodes
Venant	4 mm	70.0 mm	22,551
Venant	4 mm	72.0 mm	24,303
Venant/Sphere	4 mm	74.0 mm	26,745
Venant/Sphere	4 mm	75.5 mm	28,233
Venant/Sphere	4 mm	77.0 mm	29,807
Sphere	7 mm	74.0 mm	4,911
Sphere	10 mm	74.0 mm	1,743
Partial	4 mm	70.0 mm	22,475
Partial	4 mm	72.0 mm	24,429
Partial	4 mm	74.0 mm	26,538
Partial	4 mm	75.5 mm	28,150
Partial	4 mm	77.0 mm	28,896
Subtraction	10 mm	74.0 mm	1,716
Subtraction	10 mm	77.0 mm	1,887

Table A.8: Computation times of the different interpolation approaches. Forward indicates the time for the interpolation of one forward solution, leadfield indicates the overall time for 19.000 forward computations. An analytic leadfield with 26745 positions is used as basis.

Interpolation	Order	Forward	Leadfield
Trilinear	1	0.9 ms	17 s
Bezier	2	11.9 ms	3 min 46 s
Bezier	3	59.7 ms	18 min 54 s
Bezier	4	267.2 ms	87 min 27 s

A.2 Additional Figures

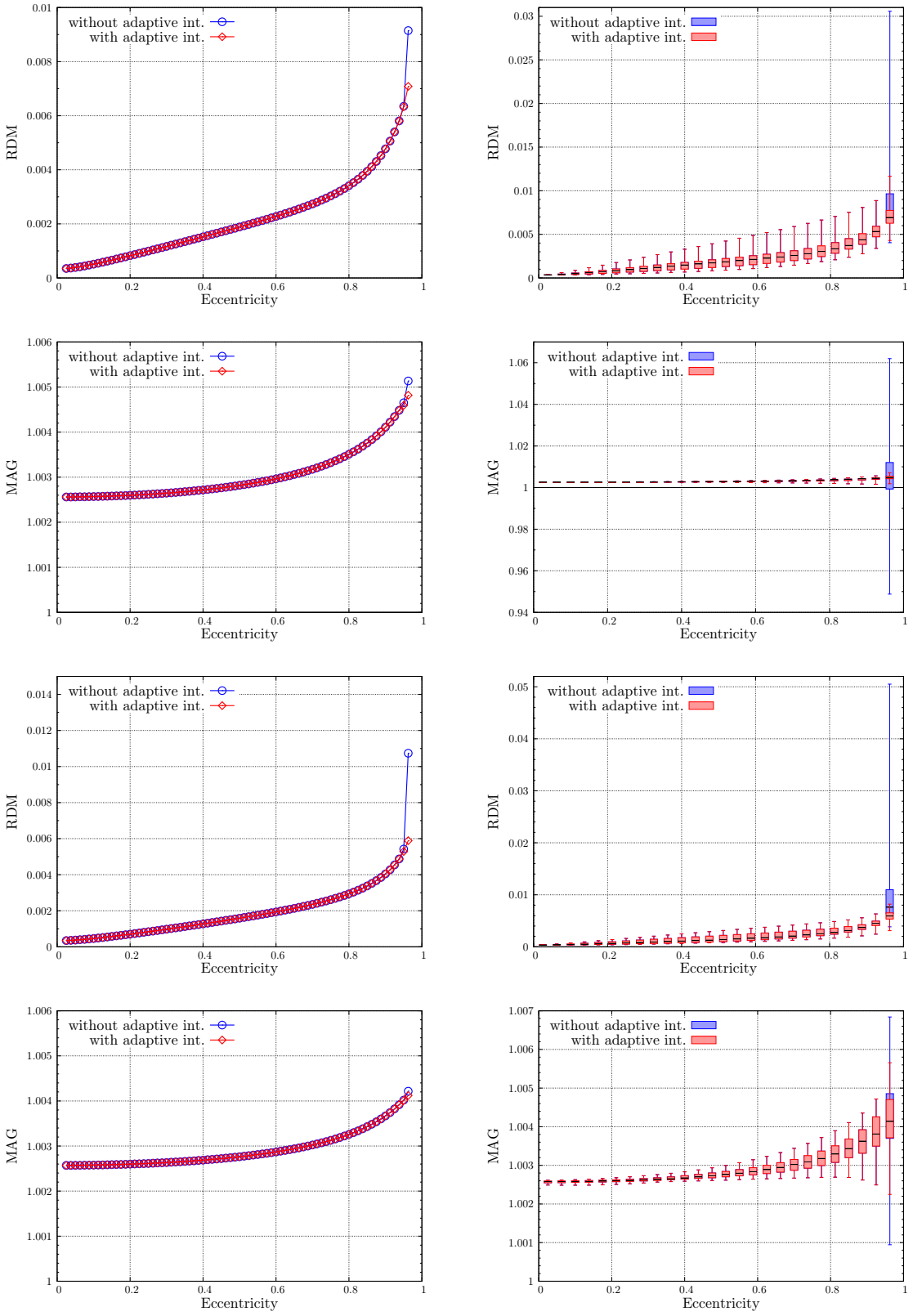

Figure A.1: RDM and MAG versus eccentricity for the symmetric BEM with and without adaptive integration. The upper graphs show the results for radial dipoles, the lower graphs those for tangential dipoles. Note that the y-axes are scaled individually. The maximal source eccentricity is 96.25%.

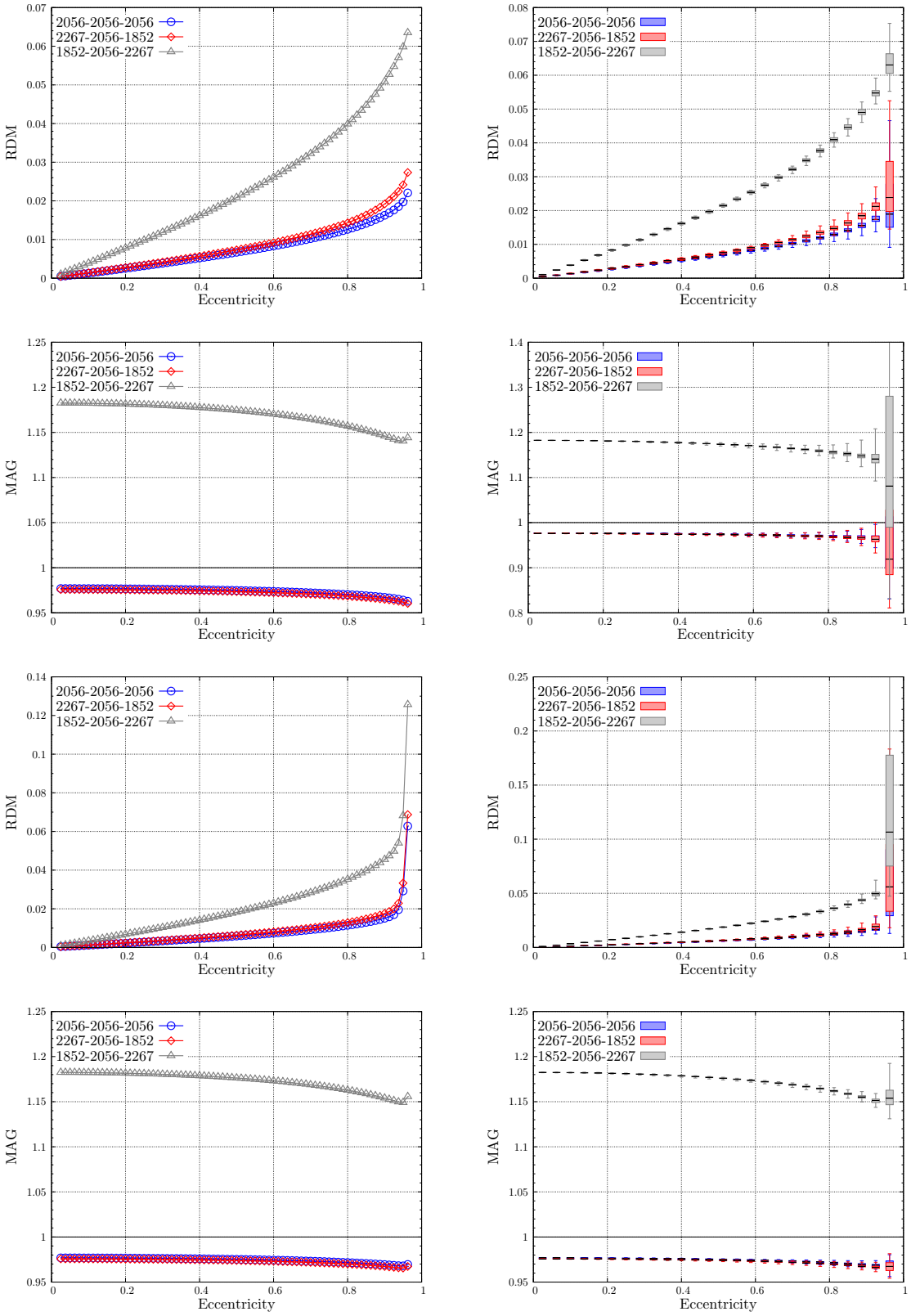

Figure A.2: RDM and MAG versus eccentricity for the double layer BEM with different nodes per sphere configurations. First value gives the nodes on the inner, second on the mid, third on the outer sphere. The upper graphs show the results for radial dipoles, the lower graphs those for tangential dipoles. Note that the y-axes are scaled individually. The maximal source eccentricity is 96.25%.

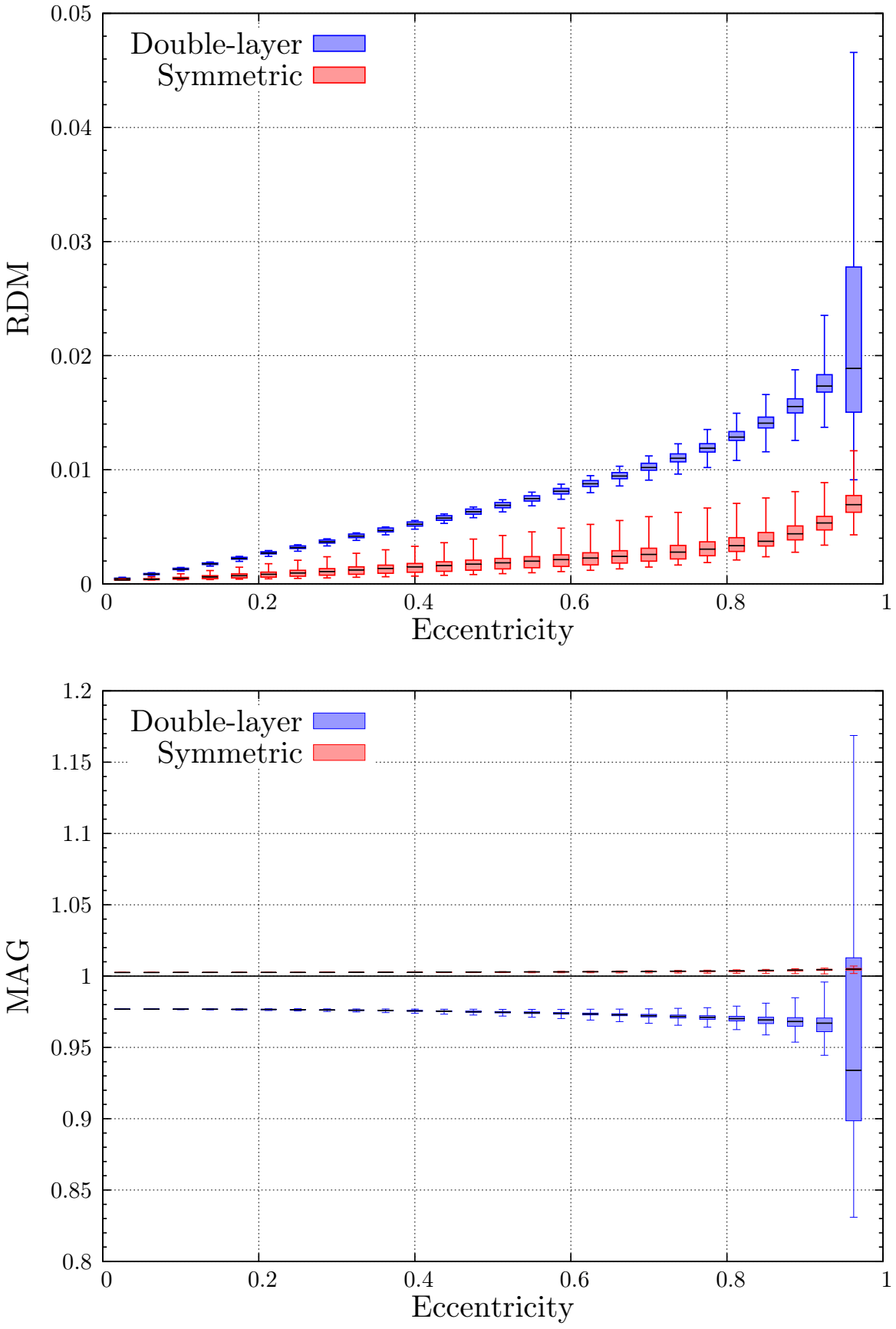

Figure A.3: Large versions of the boxplots shown in Figure 2.5 for radial dipoles.

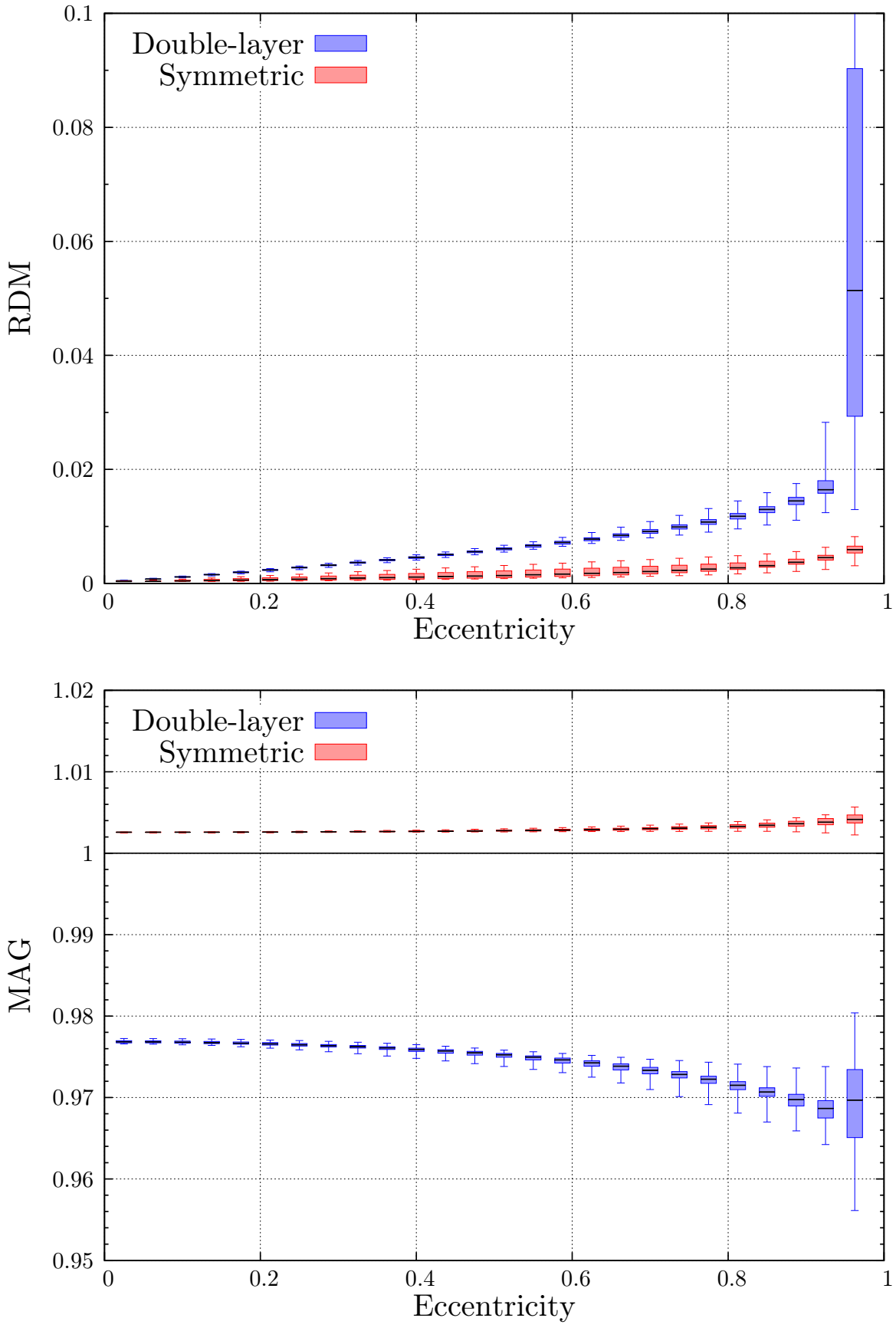

Figure A.4: Large versions of the boxplots shown in Figure 2.5 for tangential dipoles.

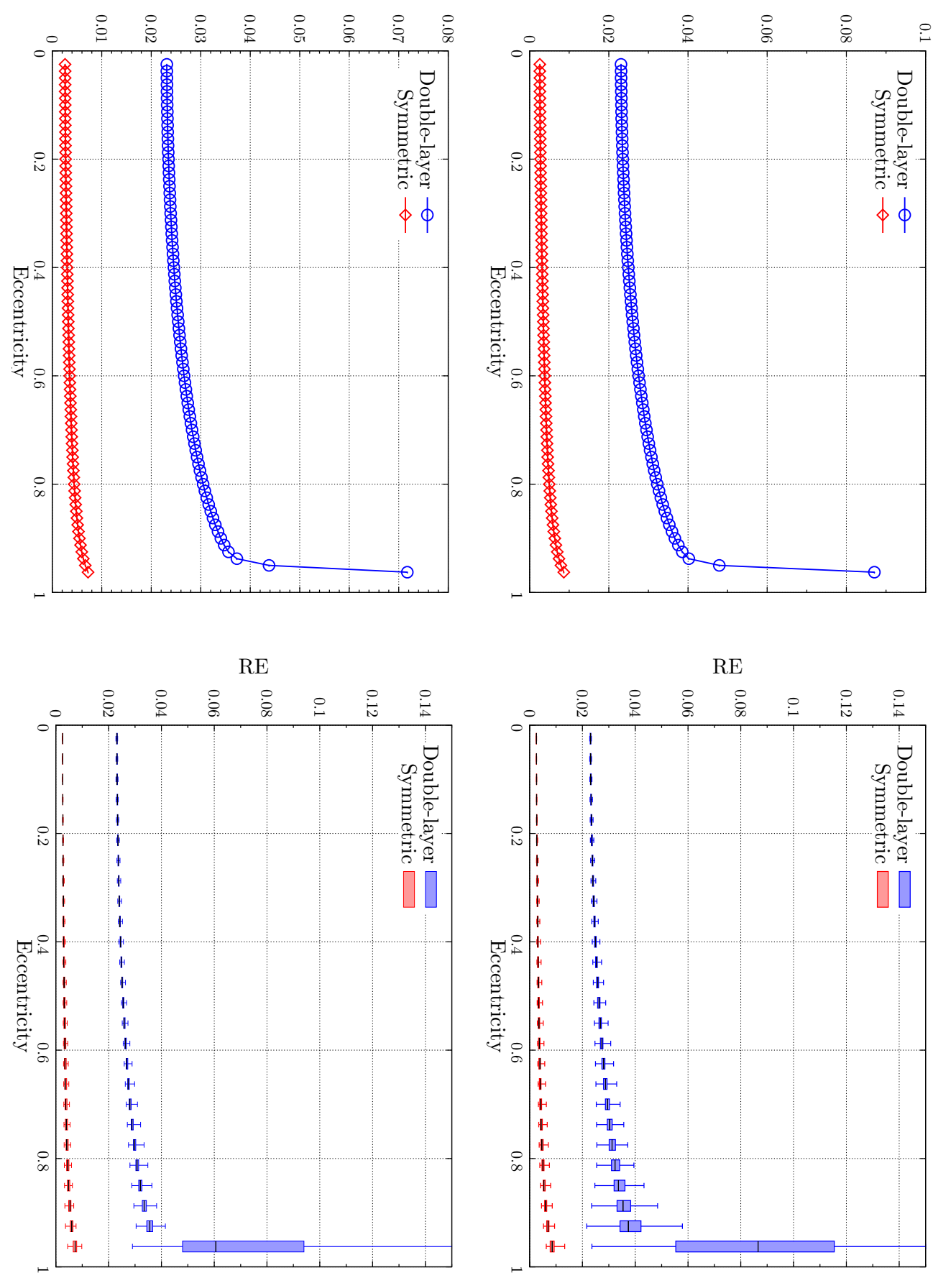

Figure A.5: RE versus eccentricity. The upper graphs show the results for radial dipoles, the lower graphs those for tangential dipoles. Note that the y-axes are scaled individually. The maximal source eccentricity is 96.25%.

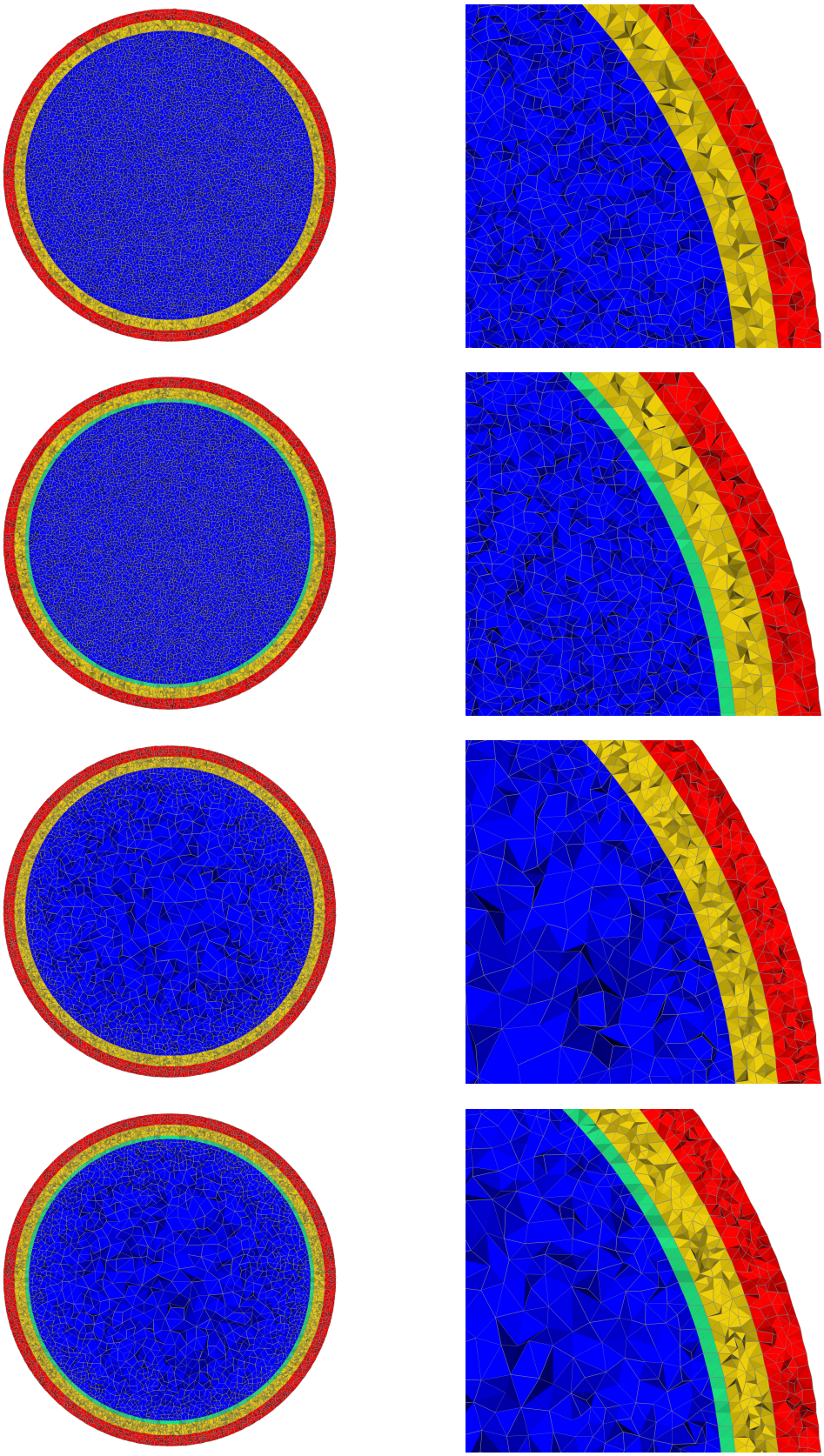

Figure A.6: The four tetrahedral FE models. The upper four images show the models that are designated for Venant and partial integration approach, the lower four those for the subtraction approach. The cut is made through the $x = 127$ plane.

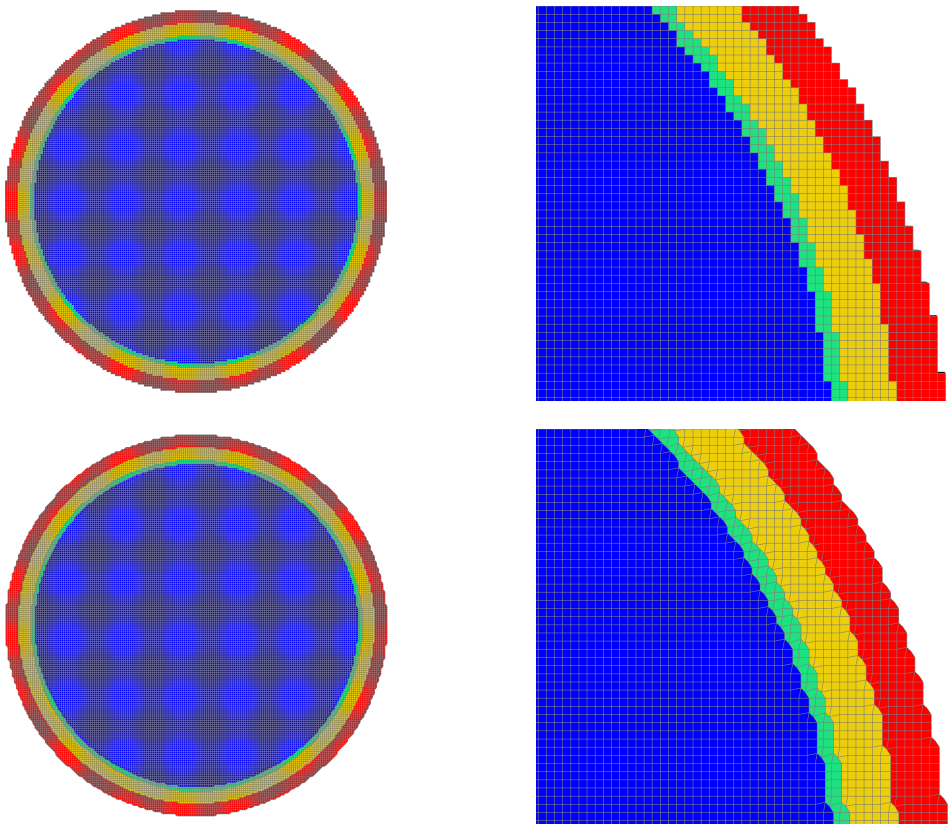

Figure A.7: The two cubic FE models. The upper two images show the model without node shift, the lower two the model with node shift. The cut is made through the $x = 127$ plane.

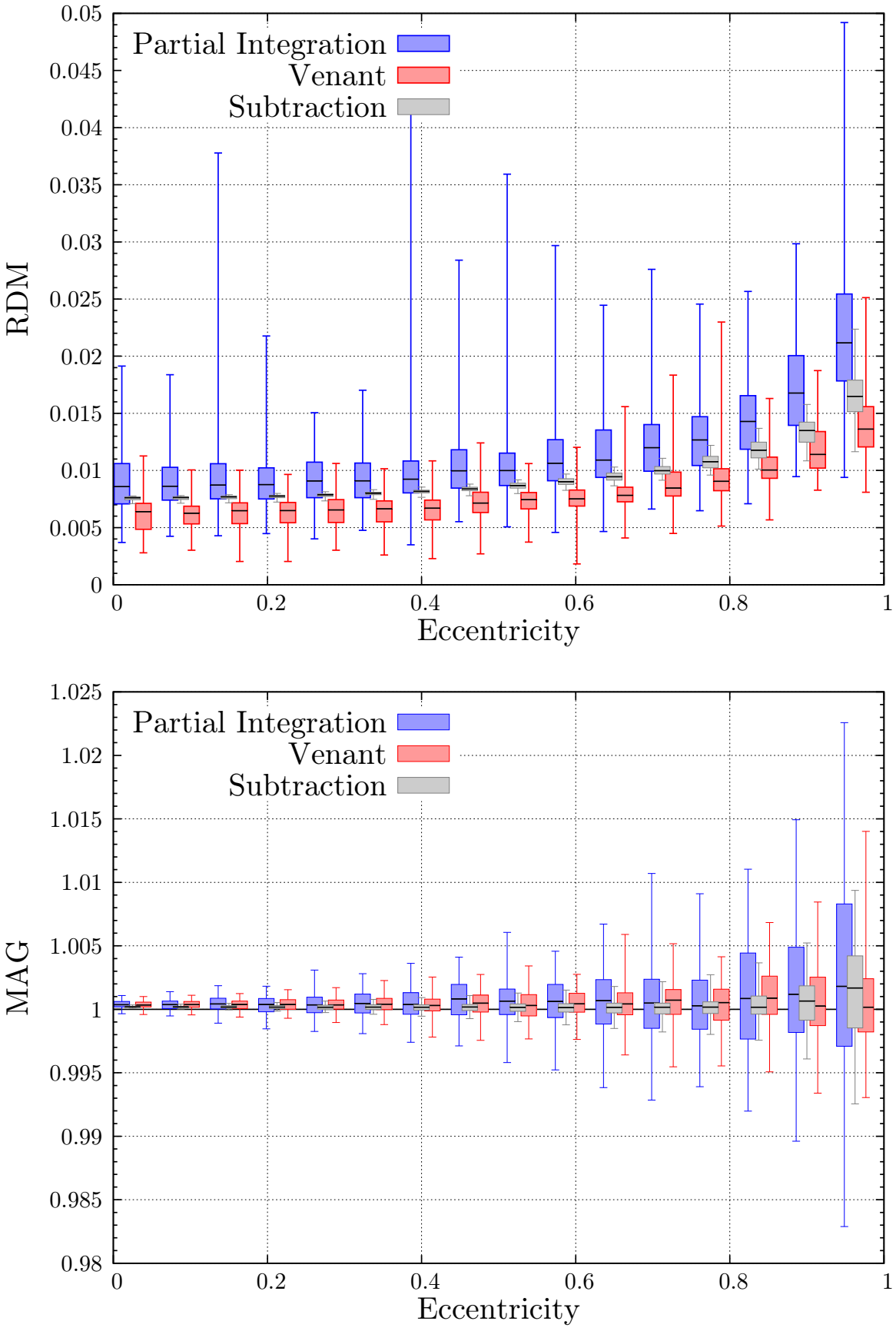

Figure A.8: Large versions of the boxplots shown in Figure 3.5 for radial dipoles.

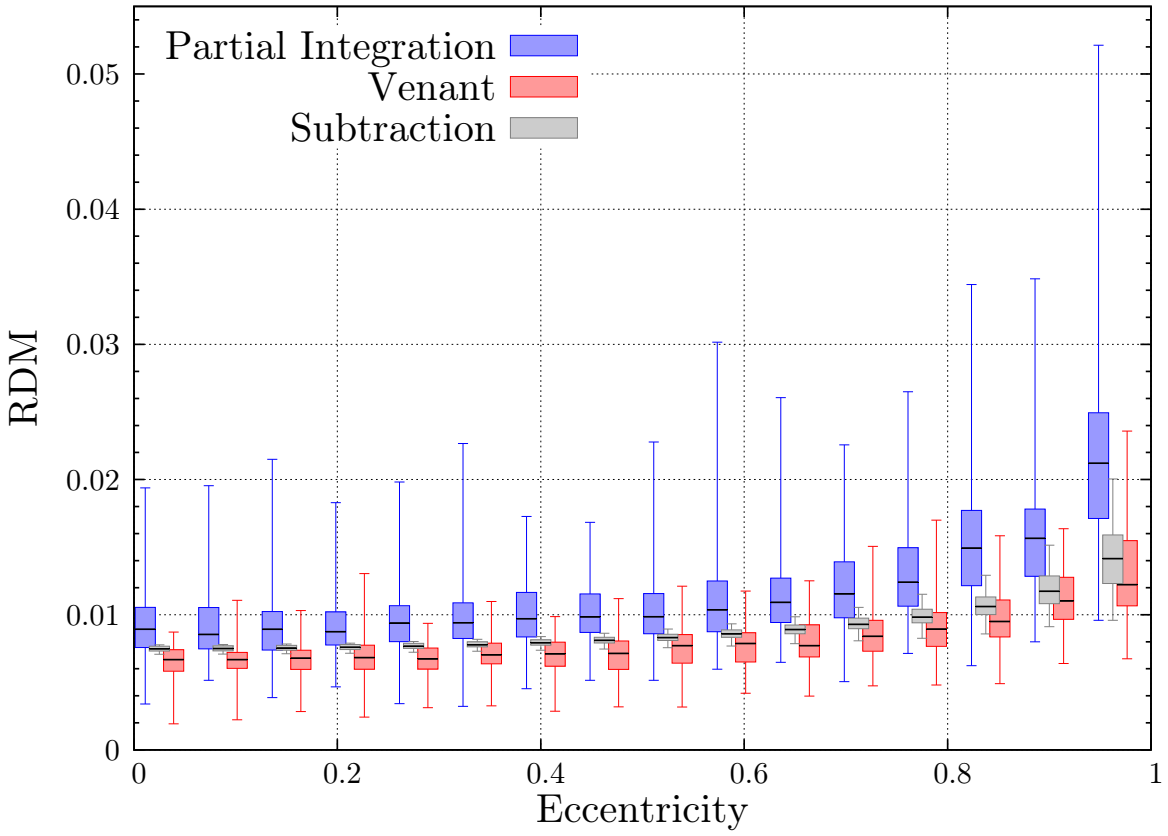

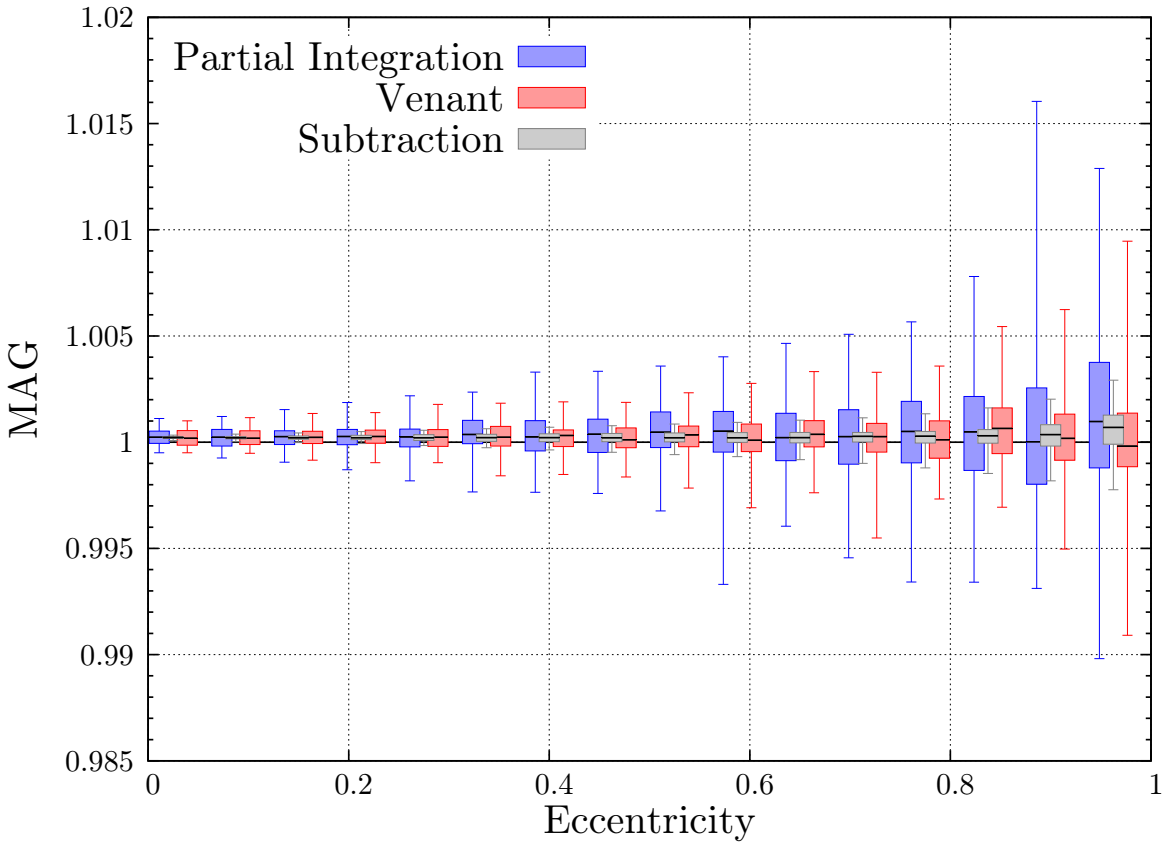

Figure A.9: Large versions of the boxplots shown in Figure 3.5 for tangential dipoles.

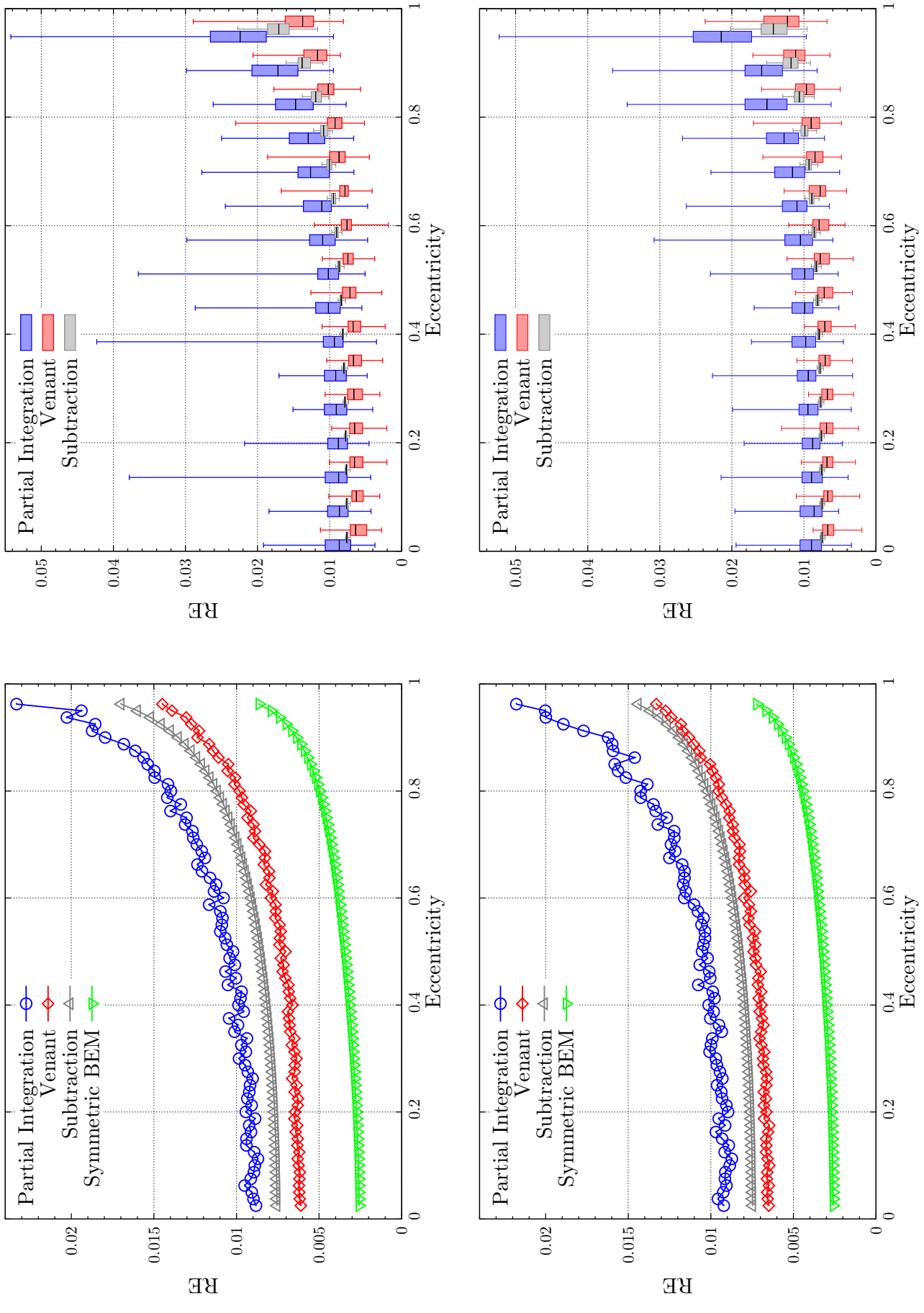

Figure A.10: RE versus eccentricity for tetrahedral three layer model. The upper graphs show the results for radial dipoles, the lower graphs those for tangential dipoles. Note that the y-axes are scaled individually. The maximal source eccentricity is 98.72%.

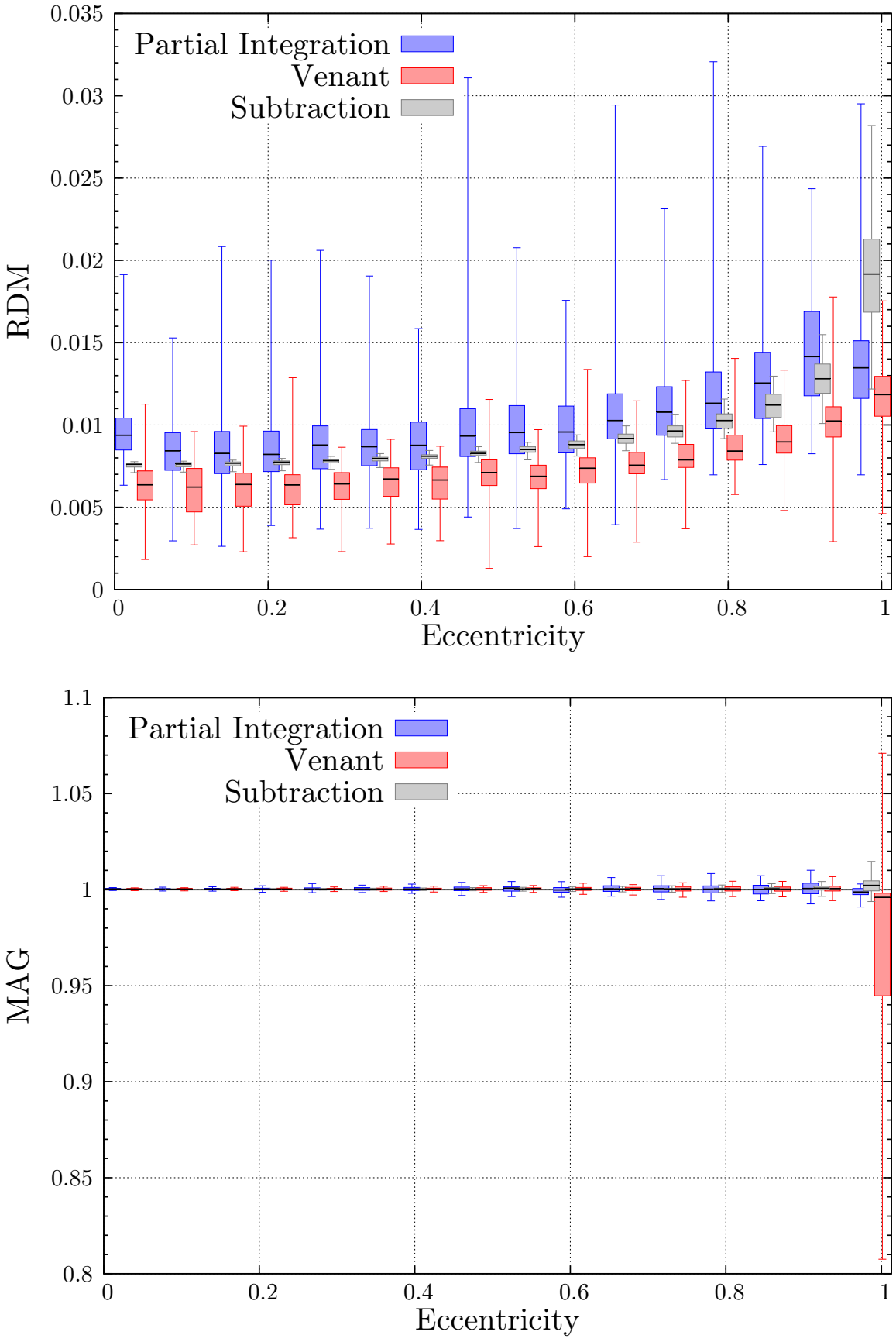

Figure A.11: Large versions of the boxplots shown in Figure 3.6 for radial dipoles.

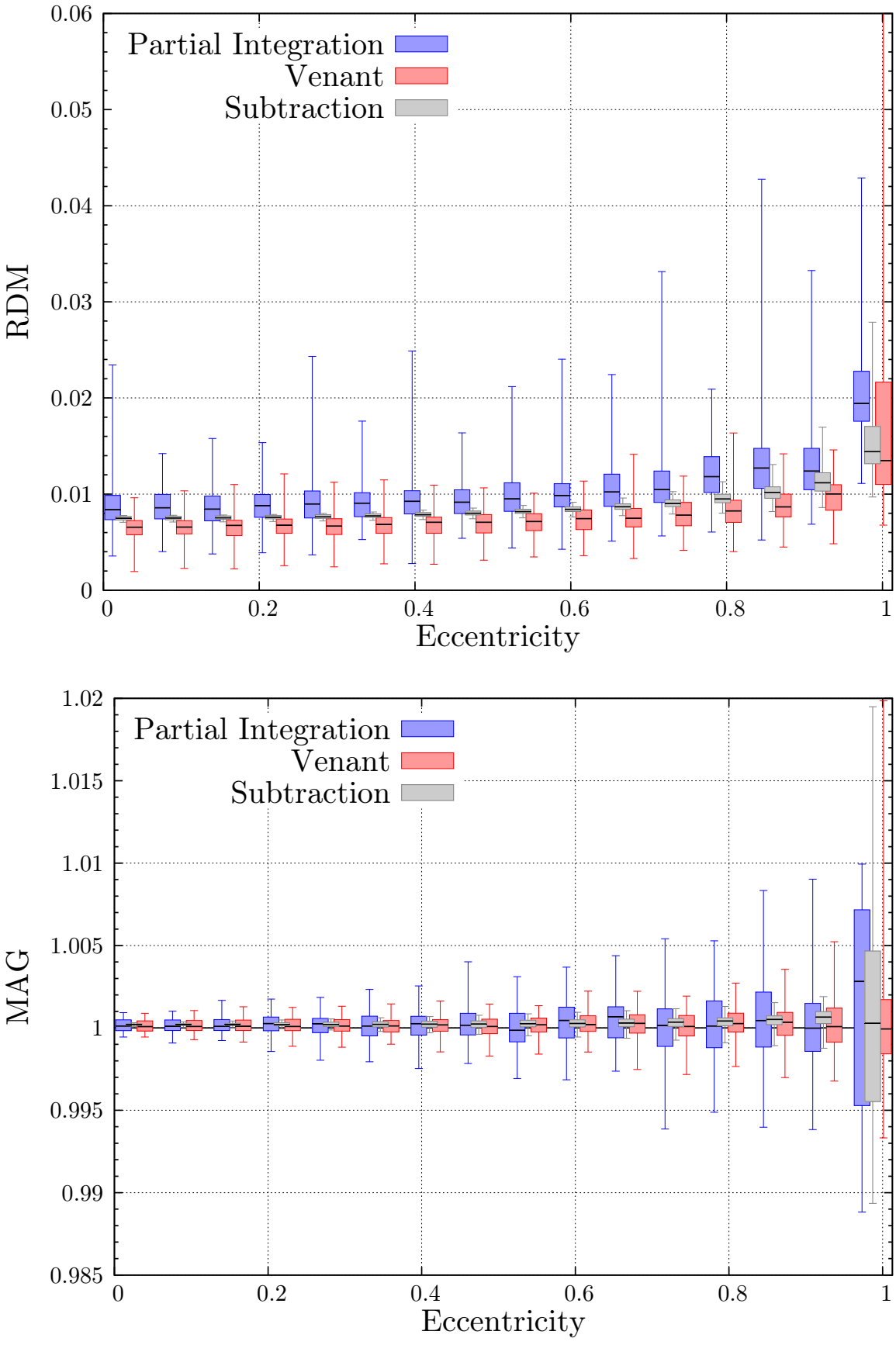

Figure A.12: Large versions of the boxplots shown in Figure 3.6 for tangential dipoles.

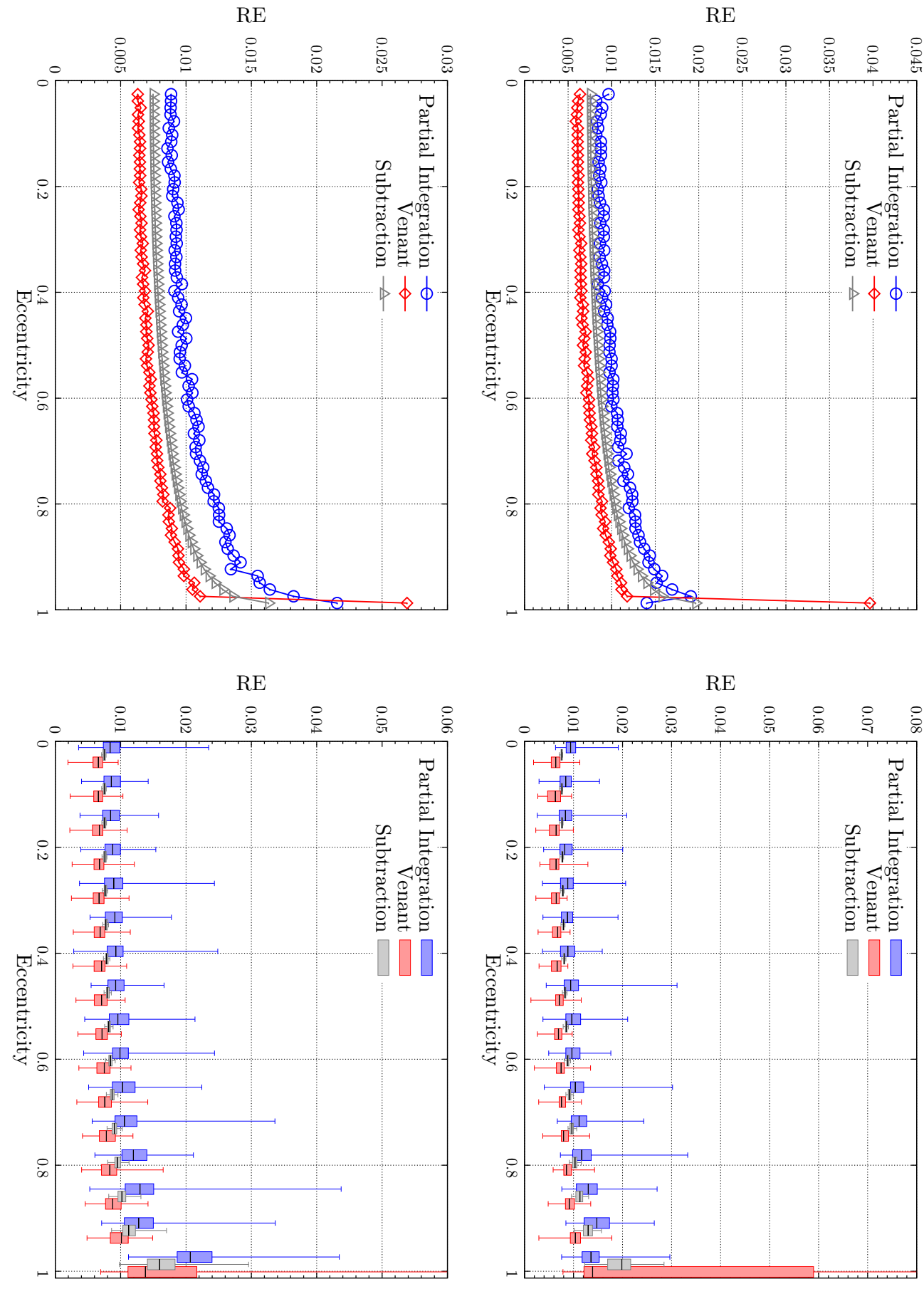

Figure A.13: RE versus eccentricity for tetrahedral four layer model. The upper graphs show the results for radial dipoles, the lower graphs those for tangential dipoles. Note that the y-axes are scaled individually. The maximal source eccentricity is 98.72%.

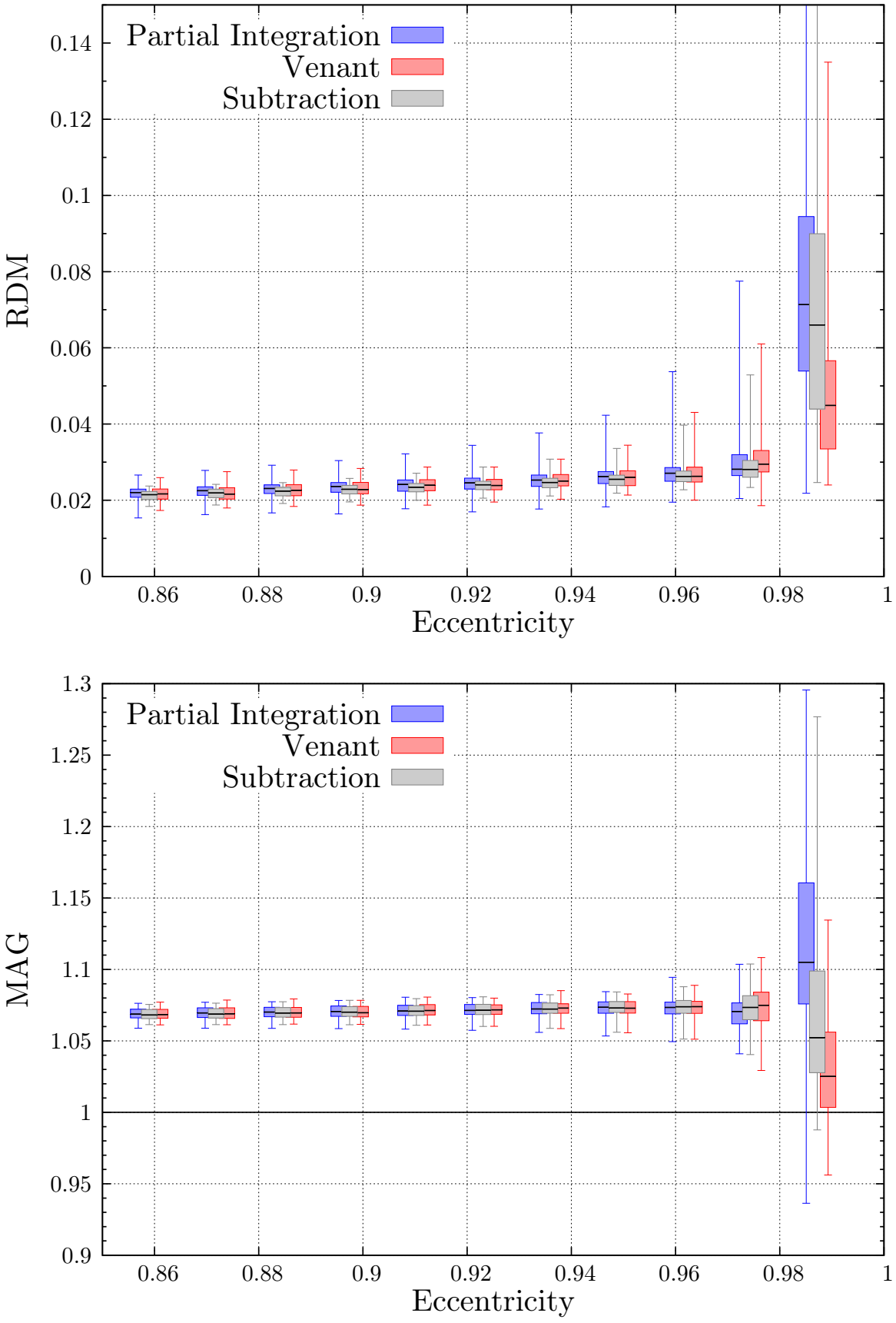

Figure A.14: Large versions of the boxplots shown in Figure 3.7 for radial dipoles.

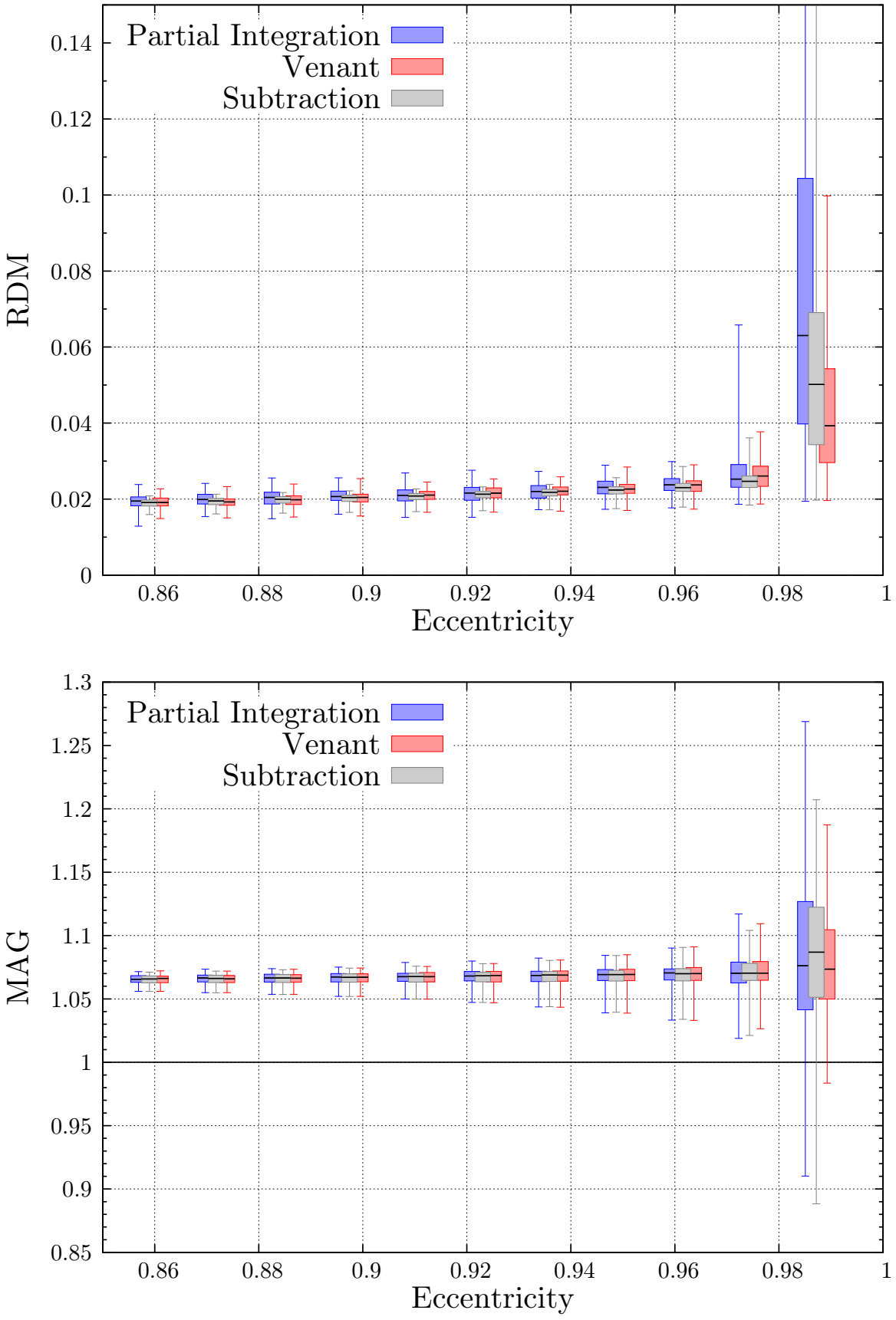

Figure A.15: Large versions of the boxplots shown in Figure 3.7 for tangential dipoles.

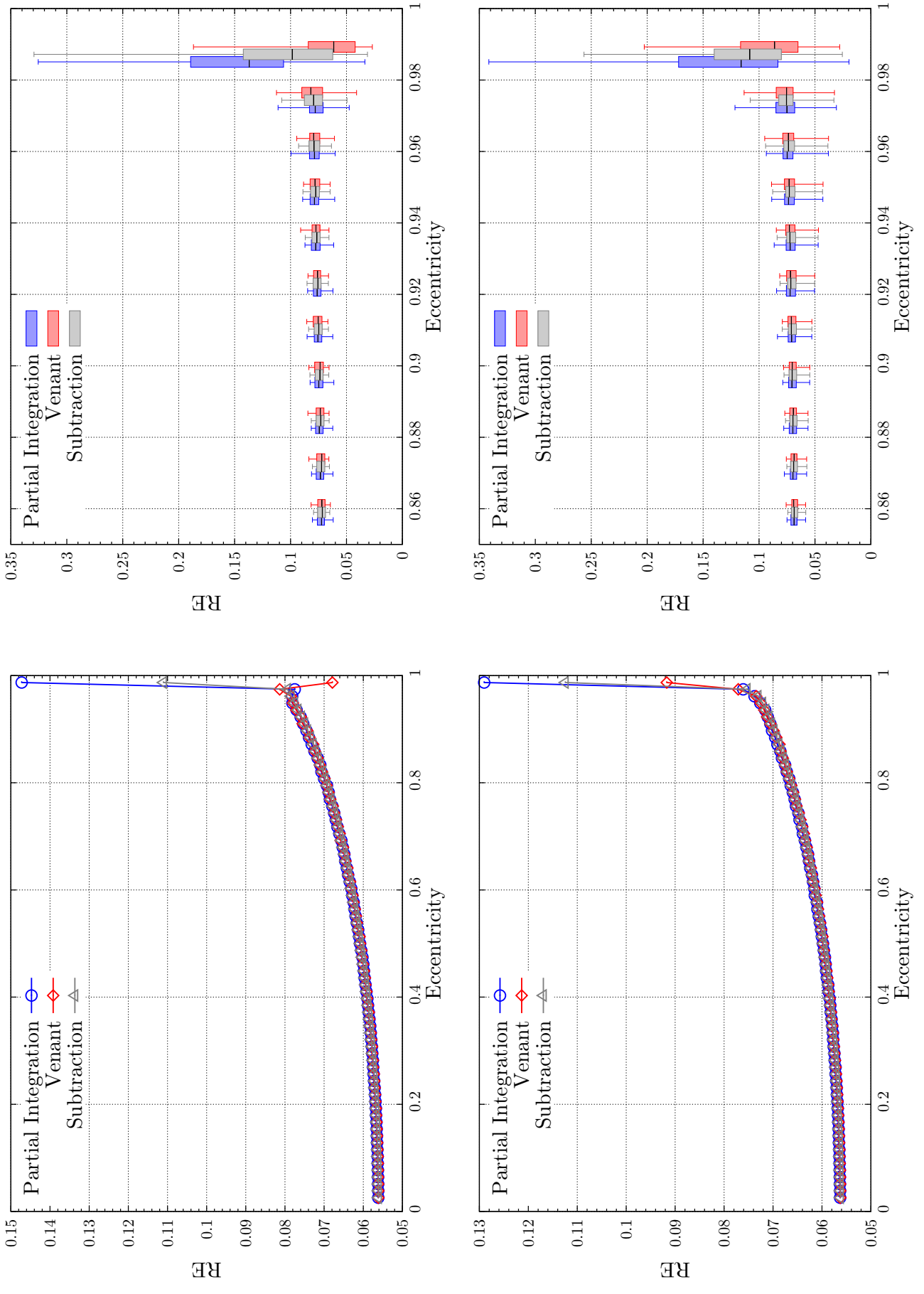

Figure A.16: RE versus eccentricity for cubic four layer model without node shift. The upper graphs show the results for radial dipoles, the lower graphs those for tangential dipoles. Note that the axes are scaled individually. The maximal source eccentricity is 98.72%.

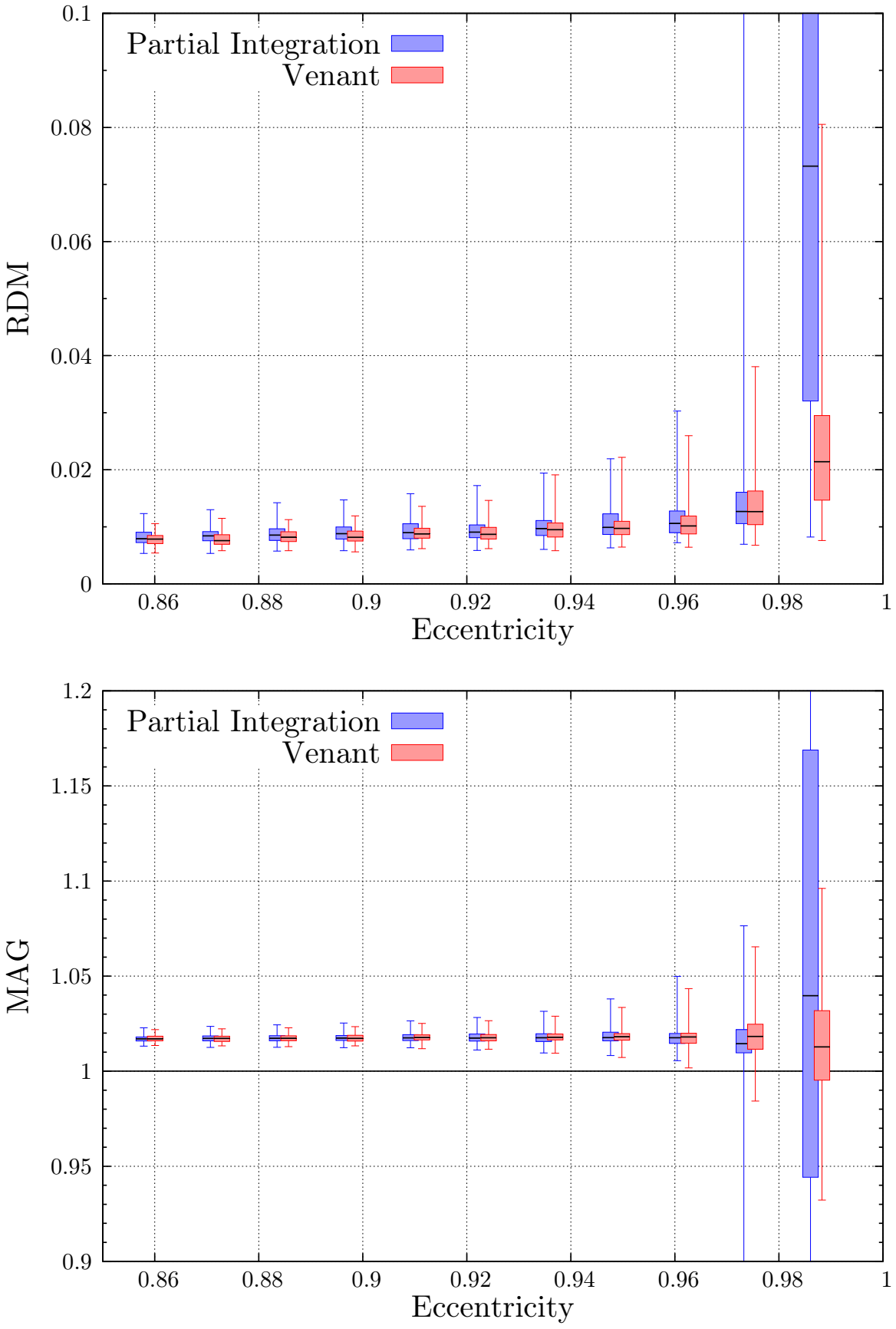

Figure A.17: Large versions of the boxplots shown in Figure 3.8 for radial dipoles.

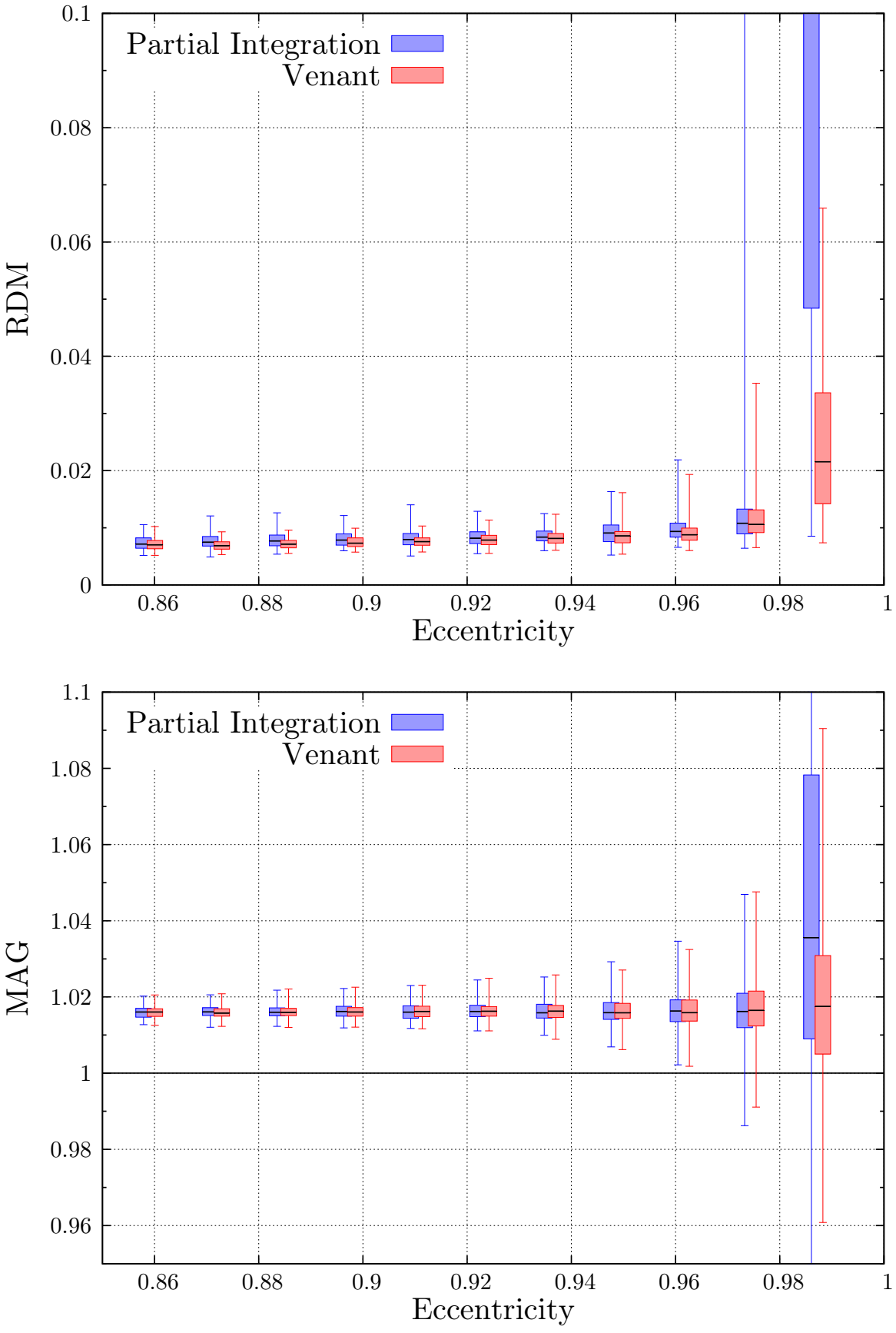

Figure A.18: Large versions of the boxplots shown in Figure 3.8 for tangential dipoles.

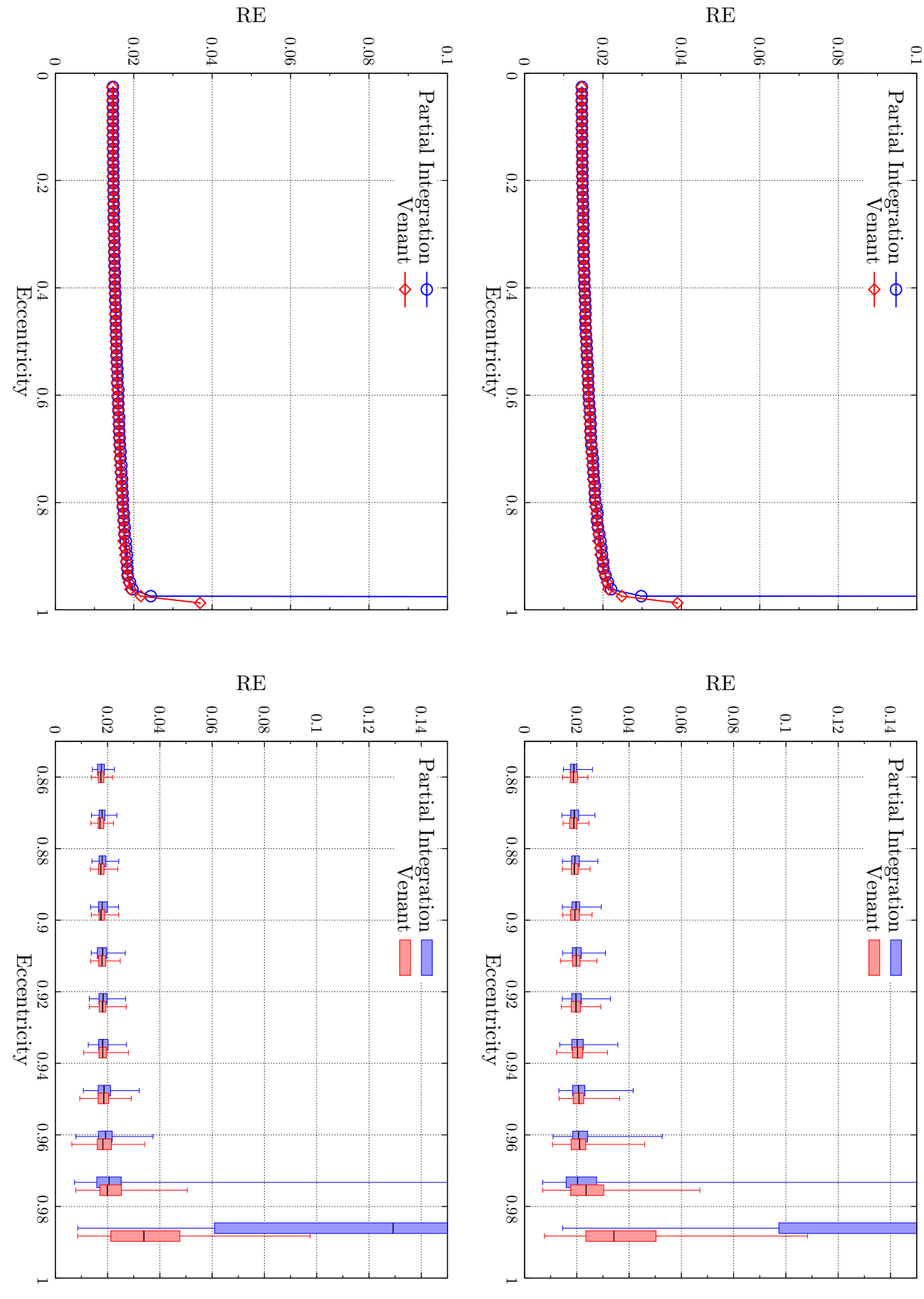

Figure A.19: RE versus eccentricity for cubic four layer model with node shift. The upper graphs show the results for radial dipoles, the lower graphs those for tangential dipoles. Note that the axes are scaled individually. The maximal source eccentricity is 98.72%.

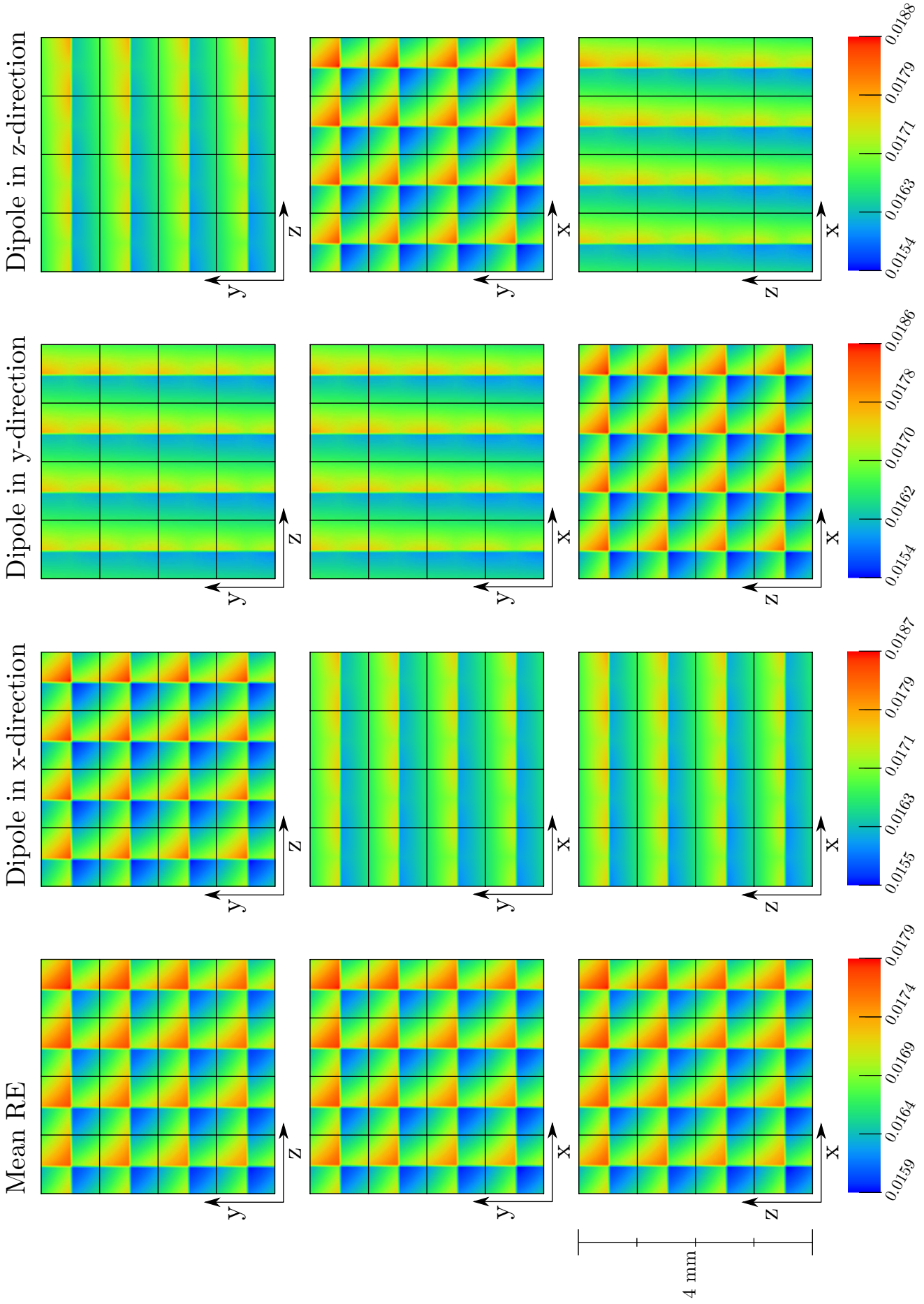

Figure A.20: Distribution of RE for the Venant approach. The bottom left corner has coordinates $(155, 155, 155)^T$.

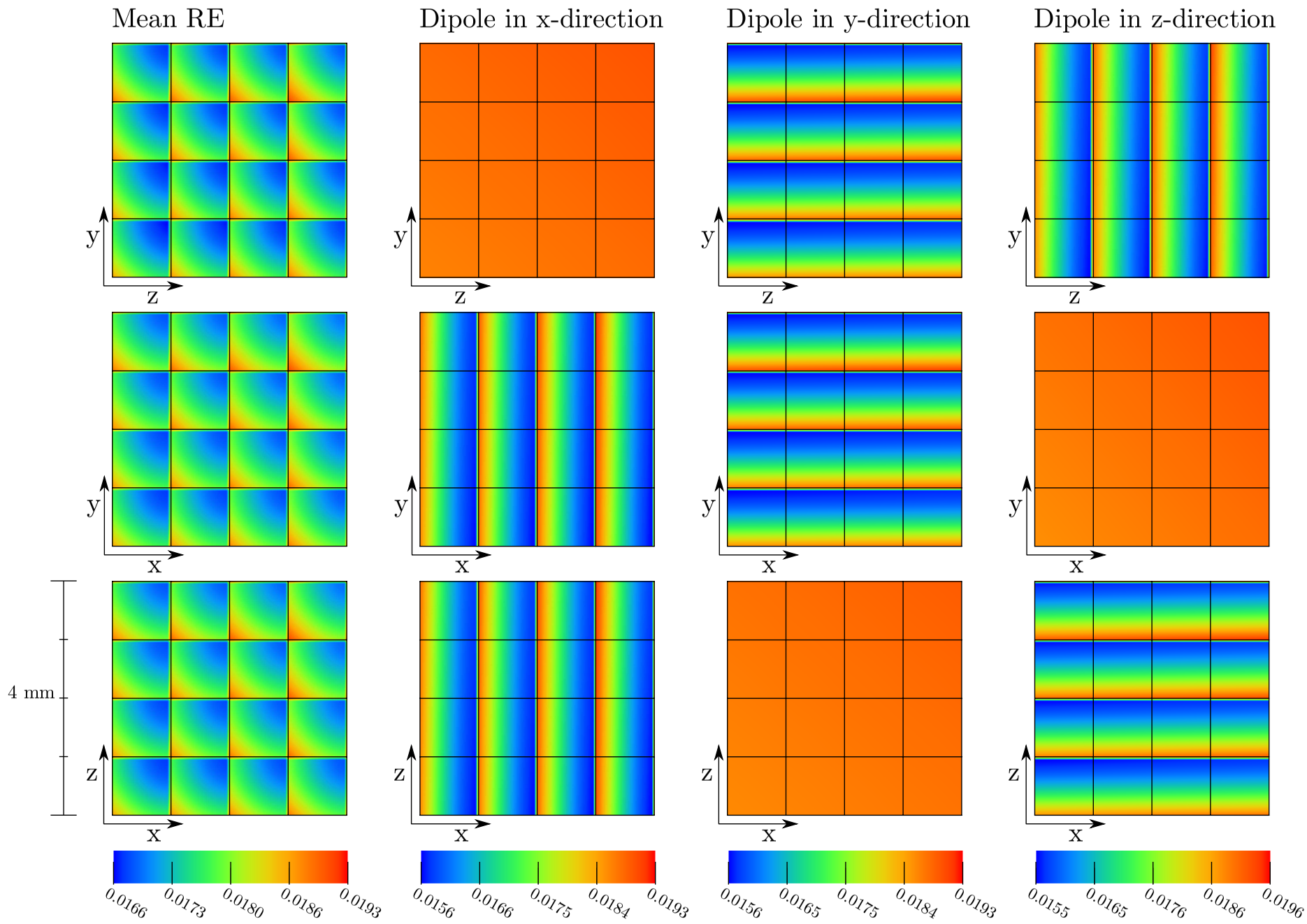

Figure A.21: Distribution of RE for the partial integration approach. The bottom left corner has coordinates $(155, 155, 155)^T$.

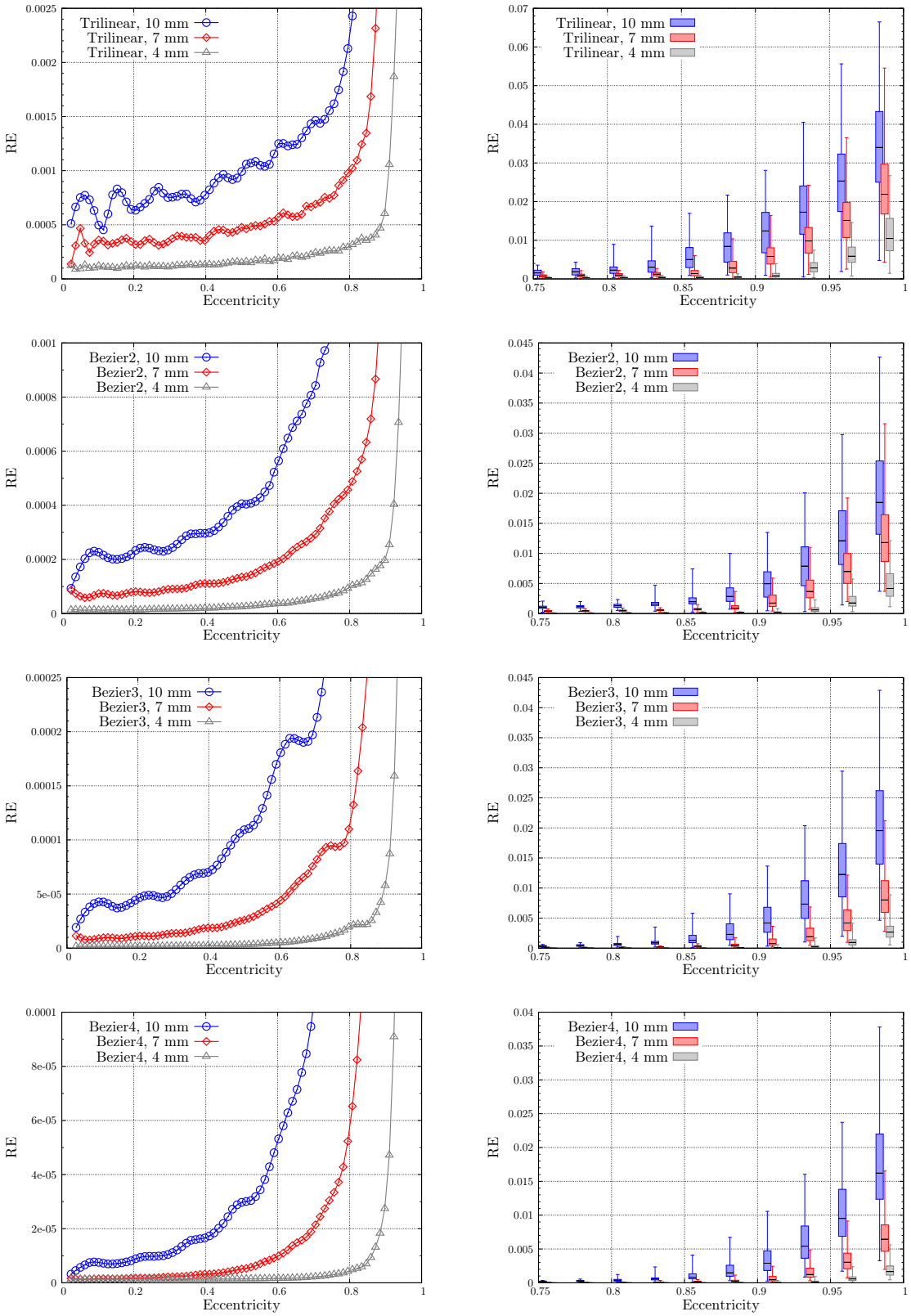

Figure A.22: RE versus eccentricity for different interpolation grid sizes cropped at a radius of 74.0 mm. Note that the axes are scaled individually. The boxes are slightly shifted from their original x-position for a better readability. The maximal source eccentricity is 98.72%.

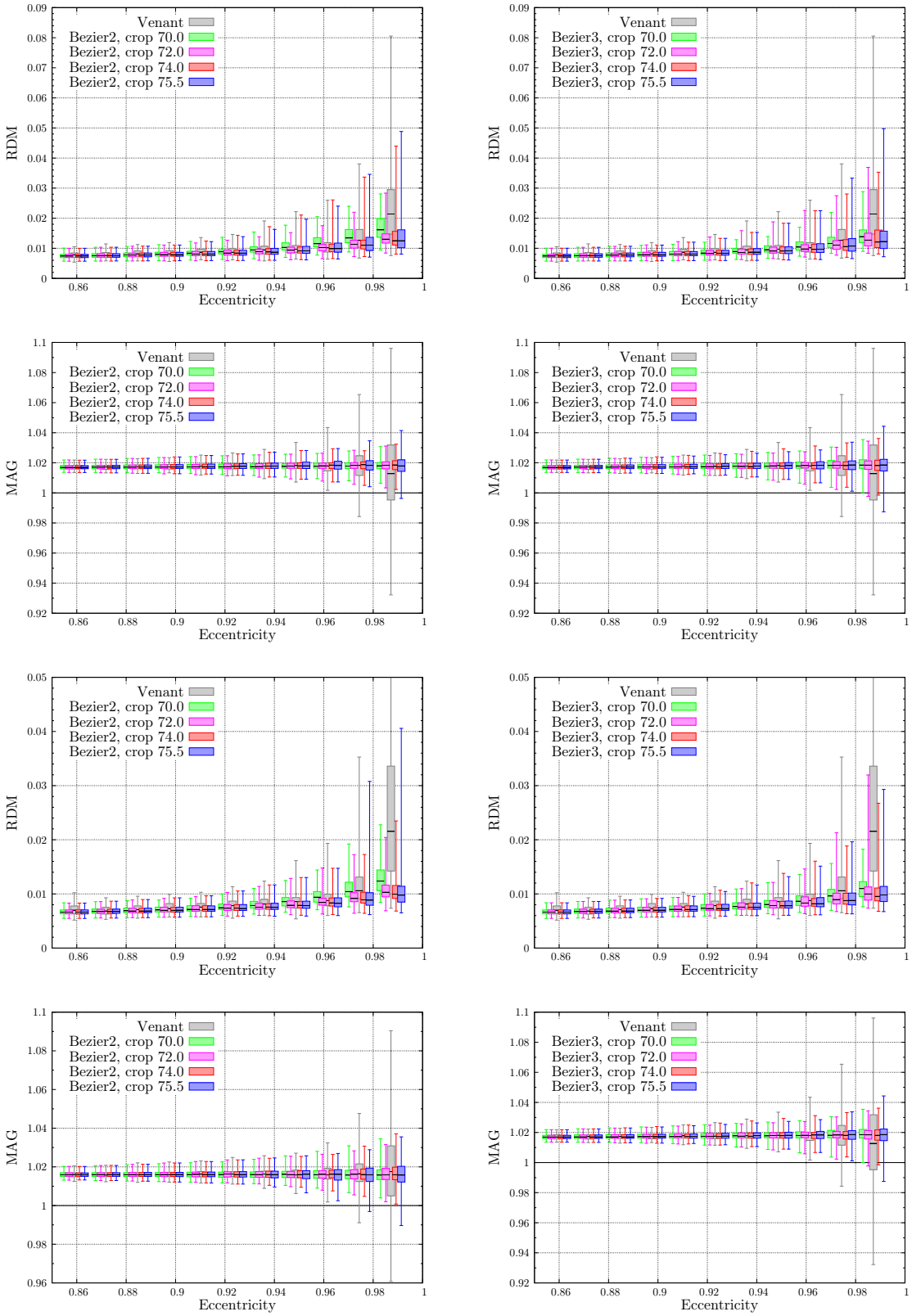

Figure A.23: RDM and MAG versus eccentricity for leadfield interpolation with Beziér interpolation of order two (left column) and three (right column) using a leadfield computed with the Venant approach. The upper graphs show the results for radial dipoles, the lower those for tangential dipoles. Note that the axes are scaled individually. The boxes are slightly shifted from their original x-position for a better readability. The maximal source eccentricity is 98.72%.

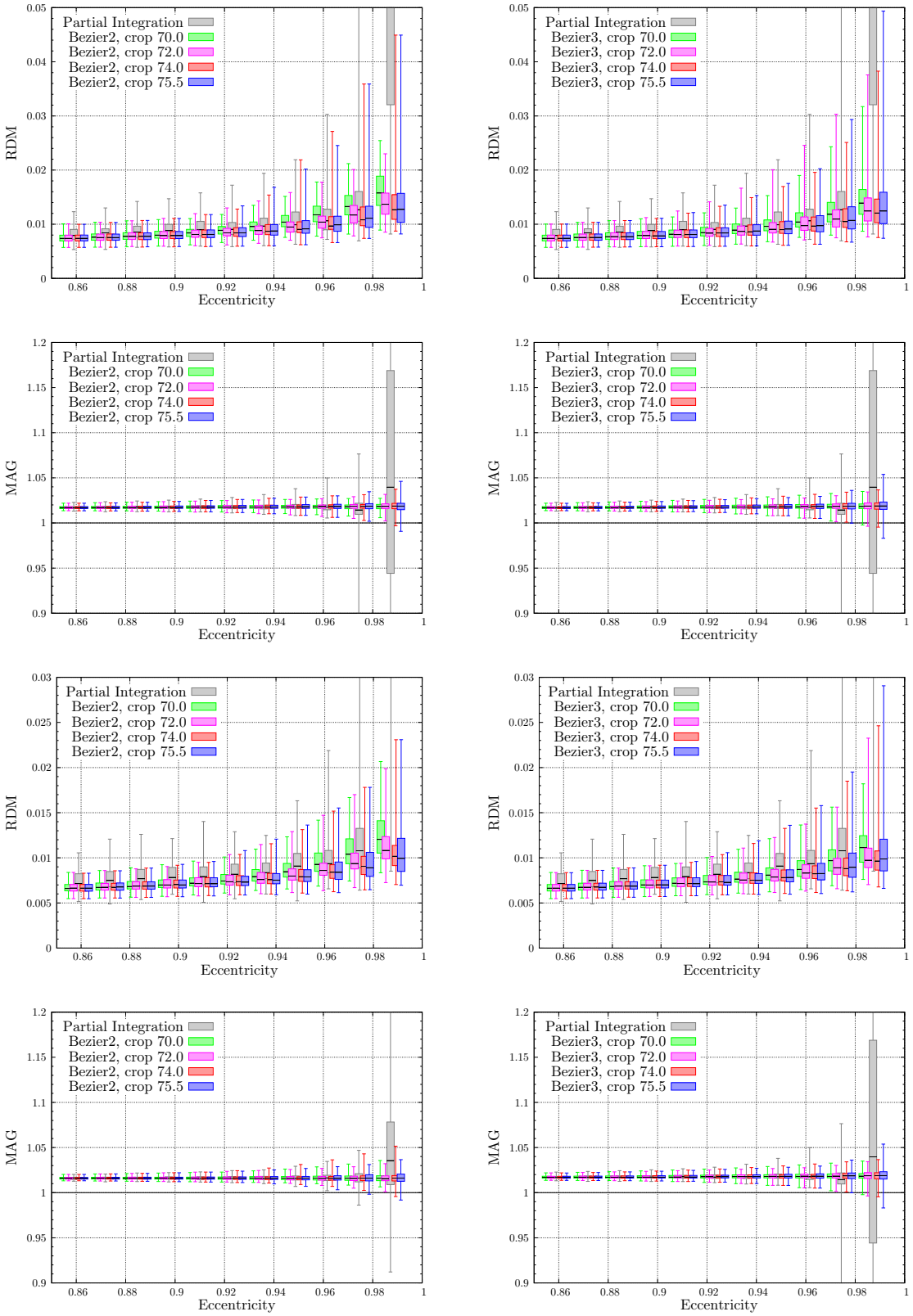

Figure A.24: RDM and MAG versus eccentricity for leadfield interpolation with Beziér interpolation of order two (left column) and three (right column) using a leadfield computed with the partial integration approach. The upper graphs show the results for radial dipoles, the lower those for tangential dipoles. Note that the axes are scaled individually. The boxes are slightly shifted from their original x-position for a better readability. The maximal source eccentricity is 98.72%.

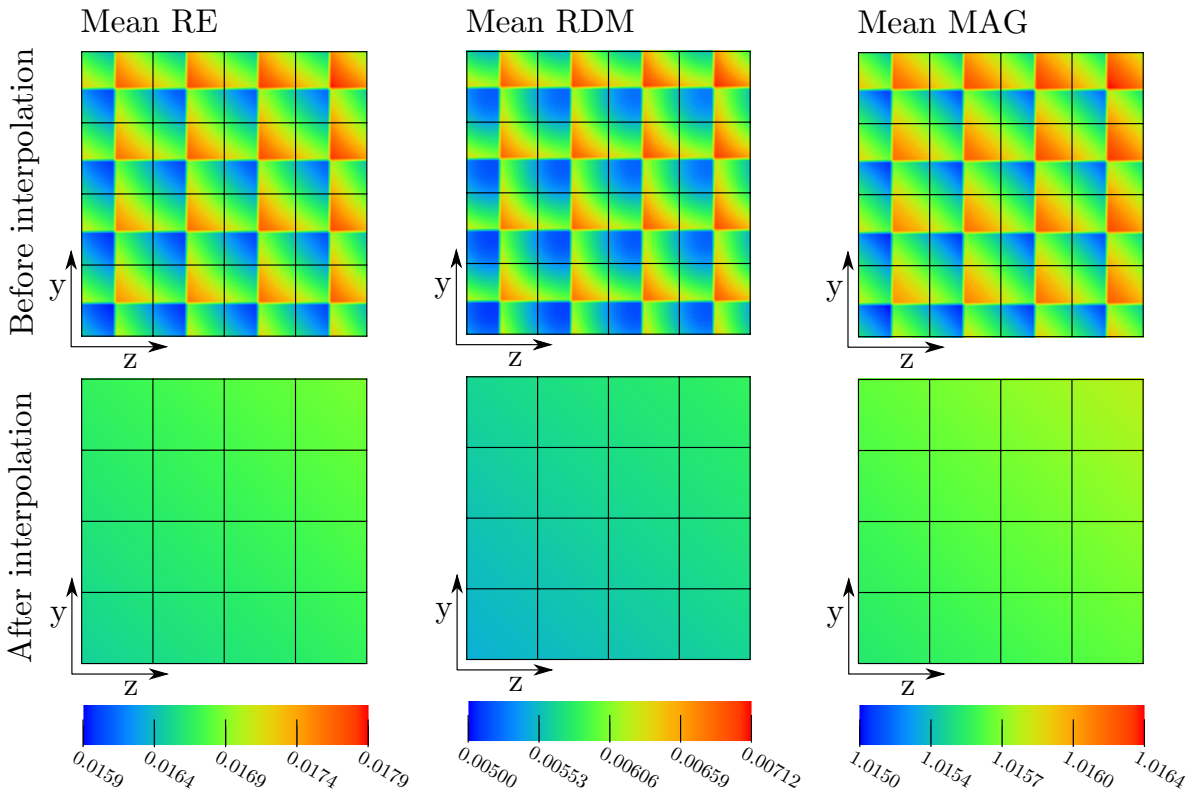

Figure A.25: Improvement of accuracy through leadfield interpolation for the Venant approach. The bottom left corner has coordinates $(155, 155, 155)^T$.

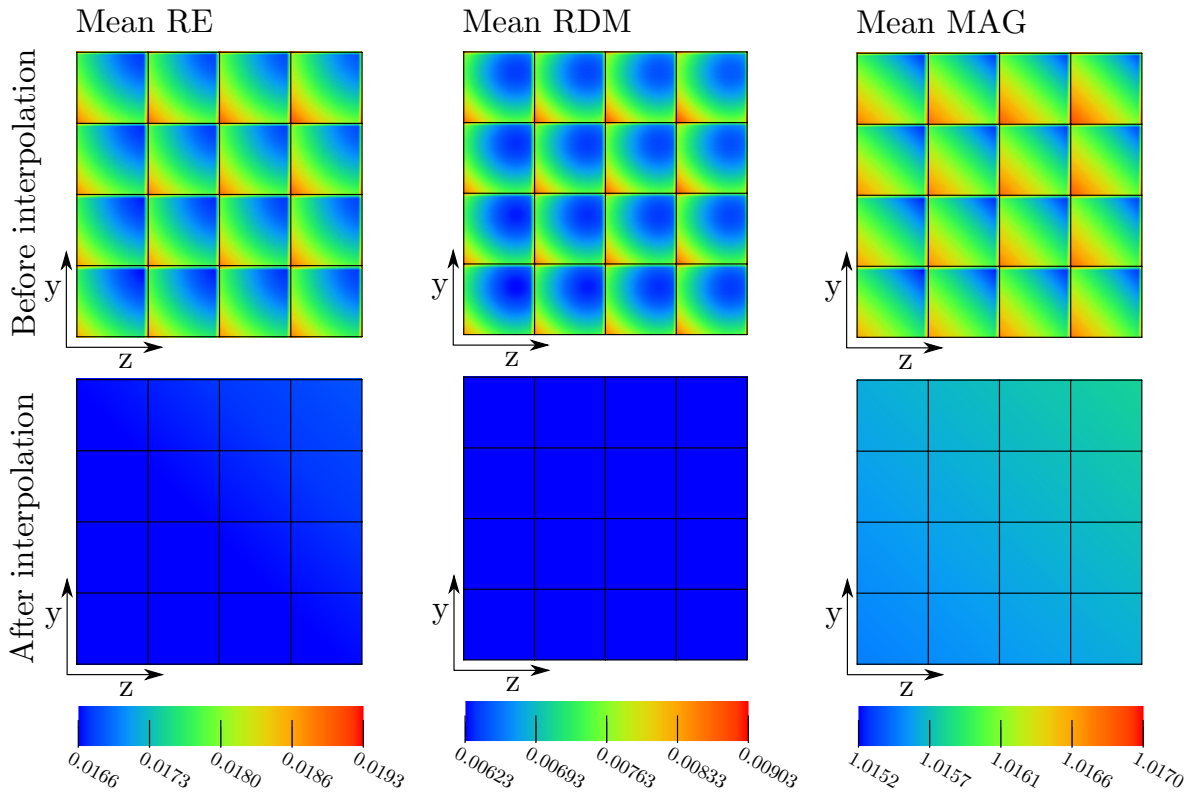

Figure A.26: Improvement of accuracy through leadfield interpolation for the partial integration approach. The bottom left corner has coordinates $(155, 155, 155)^T$.

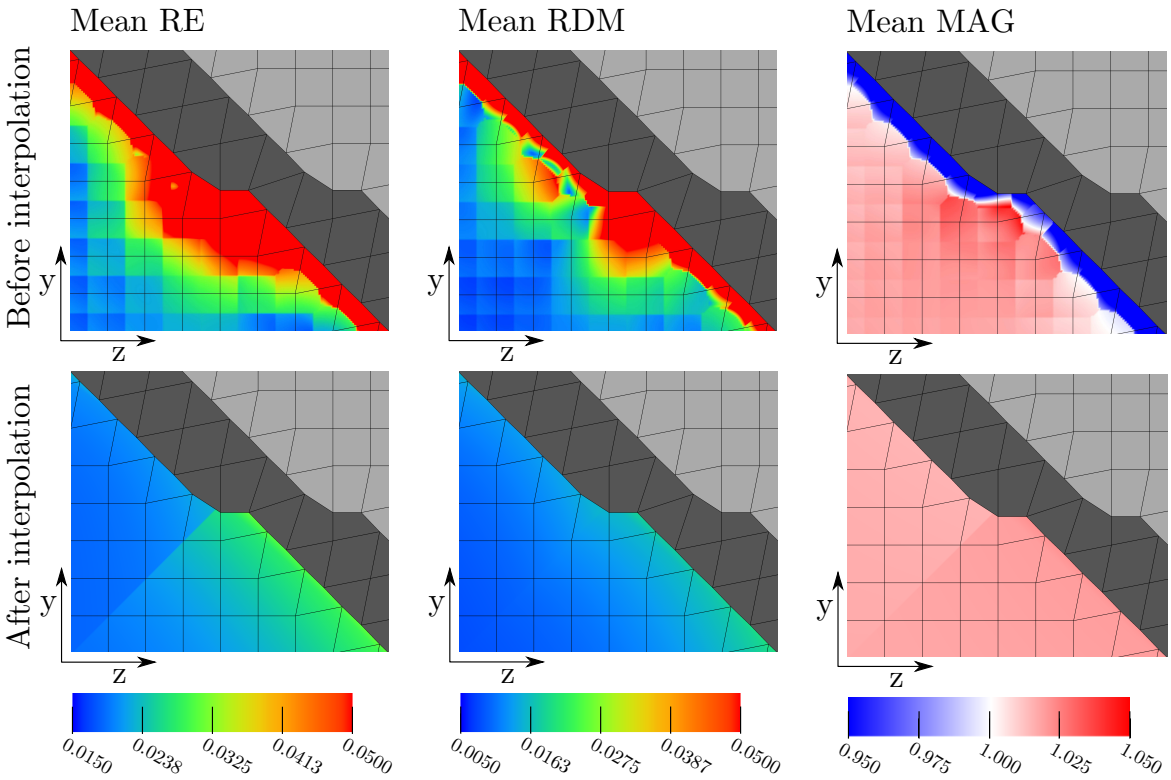

Figure A.27: Improvement of accuracy through leadfield interpolation for eccentric sources for the Venant approach. The bottom left corner has coordinates $(127, 174, 182)^T$. Dark grey corresponds to the CSF, light gray to the skull compartment.

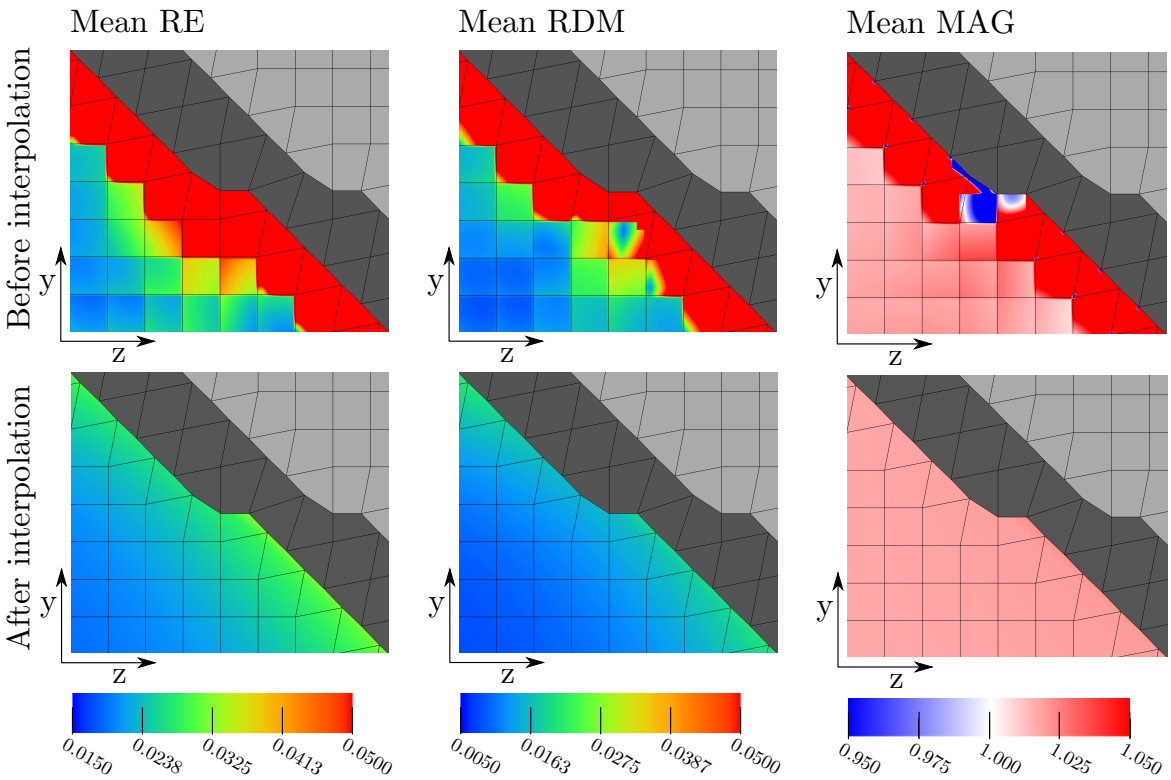

Figure A.28: Improvement of accuracy through leadfield interpolation for eccentric sources for the partial integration approach. The bottom left corner has coordinates $(127, 174, 182)^T$. Dark grey corresponds to the CSF, light gray to the skull compartment.

A.3 Miscellaneous

A.3.1 St. Venant's principle for electrostatics

The law of St. Venant was originally stated in elasticity theory, saying that a system of forces generating a particular stress distribution can be replaced by an equivalent system of forces with a negligible influence in a relatively far distance as long as the extension of the forces is matchable small or more specific

> "... the strains that can be produced in a body by the application, to a small part of its surface, of a system of forces statically equivalent to zero force and zero couple, are of negligible magnitude at distances which are large compared with the linear dimensions of the part."[40]

We find reason to transfer this law to our specific application, i.e., the calculation of the electric field induced by a point dipole, in the multipole expansion [35]. If we make sure to keep the first and second moment of our source distribution, i.e., the sum of charges and the dipole moment, respectively, constant, the influence of our redistribution decays with $\sim 1/r^3$ which is one order faster then the decay of the dipole field. By taking higher orders into account (even though they do not directly correspond to those of the multipole expansion in our case) the influence can be further reduced.

A.3.2 Estimation of Scaling Parameter

We reflect the ideas of [57]. The choice of the scaling parameter is important for the correct weighting of the different moments. While a large choice lets the zeroth and first moment dominate, a small reference length favors the influence of higher moments. Under the assumption of a cortex thickness of $d_1 = 3$ mm [61] and a distance between cortex surface and scalp electrodes of at least $d_2 = 15$ mm, a^{ref} should lead to a reasonable approximation in a sphere with a radius of 64 mm. Additionally, the reference length should be twice larger than the edge lengths of the tetrahedra, which is uncritical for fine models like ours. Since we take a sphere with a radius of 92 mm as reference, we choose to scale the reference length, $a^{ref} = 20$ mm.

Bibliography

[1] G. Adde, M. Clerc, O. Faugeras, R. Keriven, J. Kybic, and T. Papadopoulo. Symmetric BEM formulation for the M/EEG forward problem. In *Information Processing in Medical Imaging*, pages 524–535. Springer, 2003.

[2] E. Anderson and J. Dongarra. Evaluating block algorithm variants in LAPACK. In *Proceedings of the Fourth SIAM Conference on Parallel Processing for Scientific Computing*, pages 3–8. Society for Industrial and Applied Mathematics, 1990.

[3] A. Barnard, I. Duck, M. Lynn, and W. Timlake. The application of electromagnetic theory to electrocardiology: II. Numerical solution of the integral equations. *Biophysical journal*, 7(5):463–491, 1967.

[4] S. Baumann, D. Wozny, S. Kelly, and F. Meno. The electrical conductivity of human cerebrospinal fluid at body temperature. *IEEE Transactions on Biomedical Engineering*, 44(3):220–223, 1997.

[5] G. Berti. Image-based unstructured 3D mesh generation for medical applications. In *European Congress on Computational Methods in Applied Sciences and Engineering ECCOMAS*, pages 24–28, 2004.

[6] O. Bertrand, M. Thévenet, and F. Perrin. 3D finite element method in brain electrical activity studies. In J. Nenonen, H. Rajala, and T. Katila, editors, *Biomagnetic Localization and 3D Modelling*, pages 154–171. Report of the Department of Technical Physics, Helsinki University of Technology, 1991.

[7] H. Buchner, G. Knoll, M. Fuchs, A. Rienäcker, R. Beckmann, M. Wagner, J. Silny, and J. Pesch. Inverse localization of electric dipole current sources in finite element models of the human head. *Electroencephalography and Clinical Neurophysiology*, 102(4):267–278, 1997.

[8] D. Camacho, R. Hopper, G. Lin, and B. Myers. An improved method for finite element mesh generation of geometrically complex structures with application to the skullbase. *Journal of Biomechanics*, 30(10):1067–1070, 1997.

[9] T. Chan. Deflated decomposition of solutions of nearly singular systems. *SIAM Journal on Numerical Analysis*, 21(4):738–754, 1984.

[10] M. Cook and Z. Koles. A high-resolution anisotropic finite-volume head model for EEG source analysis. In *Proceedings of the 28th Annual International Conference of the IEEE Engineering in Medicine and Biology Society*, pages 4536–4539, 2006.

[11] M. Dannhauer, T. Knösche, B. Lanfer, and C. Wolters. Skull tissue conductivity modeling affects forward and inverse solution: an EEG simulation study across subjects. *NeuroImage*, 47:S74, 2009.

[12] M. Dannhauer, B. Lanfer, C. Wolters, and T. Knösche. Modeling of the human skull in EEG source analysis. *Human Brain Mapping*, 2010.

[13] J. de Munck. The potential distribution in a layered anisotropic spheroidal volume conductor. *Journal of Applied Physics*, 64:465–469, 1988.

[14] J. de Munck. A linear discretization of the volume conductor boundary integralequation using analytically integrated elements electrophysiologyapplication. *IEEE Transactions on Biomedical Engineering*, 39(9):986–990, 1992.

[15] J. de Munck, B. van Dijk, and H. Spekreijse. Mathematical dipoles are adequate to describe realistic generators of human brain activity. *IEEE Transactions on Biomedical Engineering*, 35(11):960–966, 1988.

[16] D. Drachman. Do we have brain to spare? *Neurology*, 64(12):2004, 2005.

[17] F. Drechsler, C. Wolters, T. Dierkes, H. Si, and L. Grasedyck. A full subtraction approach for finite element method based source analysis using constrained Delaunay tetrahedralisation. *NeuroImage*, 46(4):1055–1065, 2009.

[18] G. Fischer, B. Tilg, R. Modre, F. Hanser, B. Messnarz, and P. Wach. On modeling the Wilson terminal in the boundary and finite element method. *IEEE transactions on bio-medical engineering*, 49(3):217–224, 2002.

[19] O. Forster. *Analysis 3: Integralrechnung im $\mathbb{R}^n$ mit Anwendungen.* Vieweg+Teubner, 2008.

[20] M. Fuchs, R. Drenckhahn, H. Wischmann, and M. Wagner. An improved boundary element method for realistic volume-conductor modeling. *IEEE Transactions on Biomedical Engineering*, 45(8):980–997, 1998.

[21] N. Gençer and C. Acar. Sensitivity of EEG and MEG measurements to tissue conductivity. *Physics in Medicine and Biology*, 49:701, 2004.

[22] D. Geselowitz. On bioelectric potentials in an inhomogeneous volume conductor. *Biophysical journal*, 7(1):1–11, 1967.

[23] A. Gramfort, T. Papadopoulo, E. Olivi, and M. Clerc. Openmeeg: opensource software for quasistatic bioelectromagnetics. *BioMedical Engineering OnLine*, 9(1):45, 2010.

[24] A. Gramfort, T. Papadopoulo, E. Olivi, and M. Clerc. Forward field computation with OpenMEEG. *Computational Intelligence and Neuroscience*, 2011:1–13, 2011. doi:10.1155/2011/923703.

[25] D. Güllmar, J. Haueisen, and J. Reichenbach. Influence of anisotropic electrical conductivity in white matter tissue on the EEG/MEG forward and inverse solution. A high-resolution whole head simulation study. *Neuroimage*, 51(1):145–163, 2010.

[26] W. Hackbusch. *Integralgleichungen: Theorie und Numerik.* Teubner Studienbücher, 1989.

[27] W. Hackbusch. *Hierarchische Matrizen: Algorithmen und Analysis.* Springer, 2009.

[28] H. Hallez, B. Vanrumste, P. Van Hese, Y. D'Asseler, I. Lemahieu, and R. Van de Walle. A finite difference method with reciprocity used to incorporate anisotropy in electroencephalogram dipole source localization. *Physics in Medicine and Biology*, 50:3787–3806, 2005.

[29] H. Hallez, B. Vanrumste, P. Van Hese, S. Delputte, and I. Lemahieu. Dipole estimation errors due to differences in modeling anisotropic conductivities in realistic head models for EEG source analysis. *Physics in Medicine and Biology*, 53:1877–1894, 2008.

[30] M. Hämäläinen, R. Hari, R. Ilmoniemi, J. Knuutila, and O. Lounasmaa. Magnetoencephalography – theory, instrumentation, and applications to noninvasive studies of the working human brain. *Reviews of Modern Physics*, 65(2):413–497, 1993.

[31] M. Hämäläinen and J. Sarvas. Realistic conductivity geometry model of the human head for interpretation of neuromagnetic data. *IEEE Transactions on Biomedical Engineering*, 36(2):165–171, 1989.

[32] U. Hartmann and G. Berti. The SimBio-Vgrid mesh generator. http://www.rheinahrcampus.de/∼medsim/vgrid/.

[33] J. Haueisen, D. Tuch, C. Ramon, P. Schimpf, V. Wedeen, J. George, and J. Belliveau. The influence of brain tissue anisotropy on human EEG and MEG. *NeuroImage*, 15(1):159–166, 2002.

[34] R. Hosek, A. Sances Jr, R. Jodat, and S. Larson. The contributions of intracerebral currents to the EEG and evoked potentials. *IEEE Transactions on Biomedical Engineering*, 25(5):405–413, 1978.

[35] J. Jackson, C. Witte, and K. Müller. *Klassische Elektrodynamik*. de Gruyter, 2006.

[36] J. Kybic, M. Clerc, T. Abboud, O. Faugeras, R. Keriven, and T. Papadopoulo. A common formalism for the integral formulations of the forward EEG problem. *IEEE Transactions on Medical Imaging*, 24(1):12–18, 2005.

[37] B. Lanfer. Validation and comparison of realistic head modeling techniques and application to somatosensory E/MEG data. Master thesis in physics, Institut für Biomagnetismus und Biosignalanalyse, Universitätsklinikum Münster, 2007.

[38] B. Lanfer, C. Wolters, S. Demokritov, and C. Pantev. Validating finite element method based EEG and MEG forward computations. In *Proceedings of 41.Jahrestagung der DGBMT, Deutsche Gesellschaft für Biomedizinische Technik, Aachen, Germany*, pages 140–141. ISSN: 0939-4990, 2007. http://www.bmt2007.de.

[39] S. Lew, C. Wolters, T. Dierkes, C. Röer, and R. MacLeod. Accuracy and run-time comparison for different potential approaches and iterative solvers in finite element method based EEG source analysis. *Applied Numerical Mathematics*, 59(8):1970–1988, 2009.

[40] A. Love. *A treatise on the mathematical theory of elasticity*. Dover Publications, New York, 1927.

[41] J. Meijs, O. Weier, M. Peters, and A. Van Oosterom. On the numerical accuracy of the boundary element method. *IEEE Transactions on Biomedical Engineering*, 36(10):1038–1049, 1989.

[42] M.E.Taylor. *Partial Differential Equations, Basic Theory*. Springer-Verlag, New York, 1996.

[43] M. Mohr and B. Vanrumste. Comparing iterative solvers for linear systems associated with the finite difference discretisation of the forward problem in electro-encephalographic source analysis. *Medical and Biological Engineering and Computing*, 41(1):75–84, 2003.

[44] J. Mosher, R. Leahy, and P. Lewis. EEG and MEG: forward solutions for inverse methods. *IEEE Transactions on Biomedical Engineering*, 46(3):245–259, 1999.

[45] J. Munck and M. Peters. A fast method to compute the potential in the multisphere model. *IEEE Transactions on Biomedical Engineering*, 40(11):1166–1174, 1993.

[46] S. Murakami and Y. Okada. Contributions of principal neocortical neurons to magnetoencephalography and electroencephalography signals. *The Journal of Physiology*, 575(3):925–936, 2006.

[47] J. Nédélec. *Acoustic and electromagnetic equations: integral representations for harmonic problems*. Springer, 2001.

[48] Y. Okada. Empirical bases for constraints in current-imaging algorithms. *Brain Topography*, 5(4):373–377, 1993.

[49] J. Ollikainen, M. Vauhkonen, P. Karjalainen, and J. Kaipio. Effects of local skull inhomogeneities on EEG source estimation. *Medical Engineering & Physics*, 21(3):143–154, 1999.

[50] T. Oostendorp and A. Van Oosterom. Source parameter estimation in inhomogeneous volume conductors of arbitrary shape. *IEEE Transactions on Biomedical Engineering*, 36(3):382–391, 1989.

[51] C. Phillips. *Source estimation in EEG*. PhD thesis, University de Liege, Belgium, 2000.

[52] R. Plonsey. Action potential sources and their volume conductor fields. *Proceedings of the IEEE*, 65(5):601–611, 2005.

[53] S. Pursiainen. *Computational methods in electromagnetic biomedical inverse problems*. PhD thesis, Helsinki University of Technology, Faculty of Information and Natural Sciences, Institute of Mathematics, 2008.

[54] S. Pursiainen, A. Sorrentino, C. Campi, and M. Piana. Forward simulation and inverse dipole localization with the lowest order Raviart-Thomas elements for electroencephalography. *Inverse Problems*, 27(4), 2011.

[55] J. Rahola and S. Tissari. Iterative solution of dense linear systems arising from the electrostatic integral equation in MEG. *Physics in Medicine and Biology*, 47:961, 2003.

[56] C. Ramon, P. Schimpf, J. Haueisen, M. Holmes, and A. Ishimaru. Role of soft bone, CSF and gray matter in EEG simulations. *Brain Topography*, 16(4):245–248, 2004.

[57] A. Rienäcker, R. Beckmann, J. Pesch, G. Knoll, H. Buchner, and J. Silny. Dipolabbildung im FEM-Netz (III): Berücksichtigung höherer Dipolmomente. Arbeitspapier zum projekt anatomische abbildung elektrischer aktivität des zentralnervensystems, RWTH Aachen, November 1994.

[58] C. Röer. Source analysis of simultaneous sEEG and iEEG measurements in presurgical epilepsy diagnosis. Master thesis in physics, Institut für Biomagnetismus und Biosignalanalyse, Universitätsklinikum Münster, 2008.

[59] R. Sadleir and A. Argibay. Modeling skull electrical properties. *Annals of Biomedical Engineering*, 35(10):1699–1712, 2007.

[60] J. Sarvas. Basic mathematical and electromagnetic concepts of the biomagnetic inverse problem. *Physics in Medicine and Biology*, 32:11–22, 1987.

[61] M. Scherg. *Akustisch evozierte Potentiale: Grundlagen, Entstehungsmechanismen, Quellenmodell*. W. Kohlhammer, 1991.

[62] R. Schönen, A. Rienäcker, R. Beckmann, and G. Knoll. Dipolabbildung im FEM-Netz, Teil 1: Vorwärtslösung. Arbeitspapier zum projekt anatomische abbildung elektrischer aktivität des zentralnervensystems, RWTH Aachen, Juli 1994.

[63] H. Si. TetGen: A quality tetrahedral mesh generator and three-dimensional delaunay triangulator, V1.3, user's manual. Technical Report 9, Weierstrass Institute for Applied Analysis and Stochastics, 2004. http://tetgen.berlios.de.

[64] SimBio Development Group. SimBio: A generic environment for bio-numerical simulations. online, https://www.mrt.uni-jena.de/simbio, 2011.

[65] E. Somersalo, M. Cheney, and D. Isaacson. Existence and uniqueness for electrode models for electric current computed tomography. *SIAM Journal on Applied Mathematics*, 52(4):1023–1040, 1992.

[66] M. Stenroos, V. Mäntynen, and J. Nenonen. A Matlab library for solving quasi-static volume conduction problems using the boundary element method. *Computer Methods and Programs in Biomedicine*, 88(3):256–263, 2007.

[67] G. Strang and G. Fix. A Fourier analysis of the finite element variational method. *Constructive aspects of functional analysis*, pages 796–830, 1971.

[68] I. Tanzer, S. Järvenpää, J. Nenonen, and E. Somersalo. Representation of bioelectric current sources using Whitney elements in the finite element method. *Physics in Medicine and Biology*, 50:3023–3039, 2005.

[69] R. Thompson. *Das Gehirn*. Spektrum Akadademischer Verlag, 1992.

[70] S. Tissari and J. Rahola. Error analysis of a new Galerkin method to solve the forward problem in MEG and EEG using the boundary element method. In *MEG and EEG using the boundary element method, CERFACS Technical Report TR/PA/98/39, CERFACS*, 1998.

[71] D. Tuch, V. Wedeen, A. Dale, J. George, and J. Belliveau. Conductivity tensor mapping of the human brain using diffusion tensor MRI. *Proceedings of the National Academy of Sciences of the United States of America*, 98(20):11697–11701, 2001.

[72] B. Vanrumste, G. Van Hoey, P. Boon, M. D'Havé, and I. Lemahieu. Inverse calculations in EEG source analysis applying the finite difference method, reciprocity and lead fields. In *Proceedings of the 20th Annual International Conference of the IEEE Engineering in Medicine and Biology Society*, volume 20, part 4/6, 1998.

[73] D. Van't Ent, J. de Munck, and A. Kaas. An automated procedure for deriving realistic volume conductor models for MEG/EEG source localization. *IEEE Transactions on Biomedical Engineering*, 48:1434–1443, 2001.

[74] J. Weinreb, L. Brateman, E. Babcock, K. Maravilla, J. Cohen, and S. Horner. Chemical shift artifact in clinical magnetic resonance images at 0.35 T. *American Journal of Roentgenology*, 145(1):183–185, 1985.

[75] D. Weinstein, L. Zhukov, and C. Johnson. Lead-field bases for electroencephalography source imaging. *Annals of Biomedical Engineering*, 28(9):1059–1065, 2000.

[76] K. Wendel, N. Narra, M. Hannula, P. Kauppinen, and J. Malmivuo. The influence of CSF on EEG sensitivity distributions of multilayered head models. *IEEE Transactions on Biomedical Engineering*, 55(4):1454–1456, 2008.

[77] D. Wilton, A. Glisson, D. Schaubert, O. Al-Bundak, and C. Butler. Potentials integrals for uniform and linear source distributions on polygonal and polyhedral domains. *IEEE Transactions on Antennas and Propagation*, 32(3):276–281, 1984.

[78] C. Wolters. *Influence of tissue conductivity inhomogeneity and anisotropy on EEG/MEG based source localization in the human brain*. MPI of Cognitive Neuroscience Leipzig.

[79] C. Wolters. Mathematical methods in bioelectromagnetism and in the analysis of biosignals. online, http://www.sci.utah.edu/∼wolters/LiteraturZurVorlesung/Vorlesungsskriptum/, 2010.

[80] C. Wolters, A. Anwander, G. Berti, and U. Hartmann. Geometry-adapted hexahedral meshes improve accuracy of finite-element-method-based EEG source analysis. *IEEE Transactions on Biomedical Engineering*, 54(8):1446–1453, 2007.

[81] C. Wolters, A. Anwander, M. Koch, S. Reitzinger, M. Kuhn, and M. Svensén. Influence of head tissue conductivity anisotropy on human EEG and MEG using fast high resolution finite element modeling, based on a parallel algebraic multigrid solver. In T. Plesser and V. Macho, editors, *Contributions to the Heinz-Billing Award*, number 58, pages 111–157. Gesellschaft für wissenschaftliche Datenverarbeitung mbH Göttingen, 2001. ISSN: 0176-2516, http://www.billingpreis.mpg.de.

[82] C. Wolters, A. Anwander, X. Tricoche, D. Weinstein, M. Koch, and R. MacLeod. Influence of tissue conductivity anisotropy on EEG/MEG field and return current computation in a realistic head model: A simulation and visualization study using high-resolution finite element modeling. *NeuroImage*, 30(3):813–826, 2006.

[83] C. Wolters, L. Grasedyck, and W. Hackbusch. Efficient computation of lead field bases and influence matrix for the FEM-based EEG and MEG inverse problem. *Inverse Problems*, 20(4):1099–1116, 2004.

[84] C. Wolters, H. Köstler, C. Möller, J. Härdtlein, and A. Anwander. Numerical approaches for dipole modeling in finite element method based source analysis. In *International Congress Series*, volume 1300, pages 189–192. Elsevier, 2007.

[85] C. Wolters, H. Köstler, C. Möller, J. Härdtlein, L. Grasedyck, and W. Hackbusch. Numerical mathematics of the subtraction method for the modeling of a current dipole in EEG source reconstruction using finite element head models. *SIAM Journal on Scientific Computing*, 30(1):24–45, 2007.

[86] C. Wolters, M. Kuhn, A. Anwander, and S. Reitzinger. A parallel algebraic multigrid solver for finite element method based source localization in the human brain. *Computing and Visualization in Science*, 5(3):165–177, 2002.

[87] Y. Yan, P. Nunez, and R. Hart. Finite-element model of the human head: scalp potentials due to dipole sources. *Medical and Biological Engineering and Computing*, 29(5):475–481, 1991.

[88] B. Yvert, A. Crouzeix-Cheylus, and J. Pernier. Fast realistic modeling in bioelectromagnetism using lead-field interpolation. *Human Brain Mapping*, 14(1):48–63, 2001.

[89] F. Zanow. *Realistically shaped models of the head and their application to EEG and MEG*. University of Twente, The Netherlands, 1997.

[90] F. Zanow and T. Knösche. Asa-advanced source analysis of continuous and event-related EEG/MEG signals. *Brain Topography*, 16(4):287–290, 2004.

[91] Z. Zhang. A fast method to compute surface potentials generated by dipoles within multilayer anisotropic spheres. *Physics in Medicine and Biology*, 40:335–349, 1995.

Erklärung der Eigenständigkeit

Hiermit versichere ich, Johannes Vorwerk, dass ich die vorliegende Arbeit selbstständig verfasst und keine anderen als die angegebenen Hilfsmittel verwendet habe.
Gedanklich, inhaltlich oder wörtlich Übernommenes habe ich durch Angabe von Herkunft und Text oder Anmerkung belegt bzw. kenntlich gemacht. Dies gilt in gleicher Weise für Bilder, Tabellen und Skizzen, die nicht von mir selbst erstellt wurden.
Diese Arbeit wurde in gleicher oder ähnlicher Form noch keiner Prüfungsbehörde vorgelegt.

Münster, 12. April 2011